Design and Control Optimization of Hybrid Electric Vehicles: from Two-Wheel-Drive to All-Wheel-Drive Vehicles

by

Ziheng Pan

A dissertation submitted in partial fulfillment
of the requirements for the degree of
Doctor of Philosophy
(Mechanical Engineering)
in The University of Michigan
2019

Doctoral Committee:

Professor Huei Peng, Chair
Dr. Tulga Ersal
Professor Jessy Grizzle
Professor Chinedum Okwudire
Dr. Nikhil Ravi

Ziheng Pan

zihpan@umich.edu

ORCID iD: 0000-0002-9656-0138

ACKNOWLEDGEMENTS

I would like to express my sincerest gratitude to my advisor, Professor Huei Peng. Hi guidance, assistance, patience, encouragement, and continuous support have been of enormous crucial to my studies, research, and career development. Without his support, I would not be able to reach this most amazing journey thus far in my life. I would also like to thank my other committee members, Dr. Tulga Ersal, Professor Jessy Grizzle, Professor Chinedum Okwudire, and Dr. Nikhil Ravi, for their helpful advice and comments.

I am indebted to the Department of Mechanical Engineering, the Rackham Graduate School, the US-China Clean Energy Research Center, and Robert Bosch LLC for the financial support for my graduate study.

As a proud member of the Vehicle Dynamics Lab, I would like to first express my earnest gratitude to the lab alumni: Chiao-Ting Li, Changsun Ahn, Byung-joo Kim, and Xiaowu zhang, whose patient guidance helped me through my research practice. Great appreciation should go to my colleague in VDL for their help, discussion and all the good times we have had in the office: William Smith, Zhenzhong Jia, Huajie ding, Yalian Yang, Daofei Li, Yugong Luo, Diange Yang, Tianyou Guo, Ding Zhao, Baojin Wang, Steven Karamihas, Yuxiao Chen, Oguz Dagzi, Shaobing Xu, Su-Yang Shieh, Xianan Huang, Geunseob Oh, Nauman Sohani, Songan Zhang, Boqi Li, Xinpeng Wang, Minghan Zhu, and Siyuan Feng.

Moreover, I am proud of being in the big family of University of Michigan. I would like to express my sincerely gratitude to colleagues and friends I met in this family: Chaozhe He, Kaiwu, Jun Hou, Rui Chen, Ziyou Song, Junming Hu, and Jiaxi Li.

I am also highly grateful for the internship and employment opportunity that Robert Bosch LLC provided me. That experience offered me exposure to the industry and helped improve my study with more realistic considerations, constructive suggestions and

comments on my PhD research. Great appreciation should go to my colleague in Bosch for their support and advices: Li Jiang, Stefan Koidl, Jason Schwanke, Shyam Jade, Mohammad Fatouraie, James Doetsch, Michael Lim, Ryan O'Donnell, Utkarsh Pradhan, Iltesham Syed, Vasanthi Karri, Kwangwoo Jeong, Andre Brune, Andi Diko, Axel Hahn, Nandan Vora, Varoun Perumal, Martin Belley, Alessandro Allievi, Alexander Freitag, Matt Thorington Andreas Keuper, Yun Jae Cho, Kivanc Temel, and Viktor Rill.

Last, but not least, my deepest thank to my parents for their love and support. In addition, my sincerely thank to my bosom friend, Koey Yip, for her encouragement, guidance, and support. Without her, I won't be able to overcome the toughest time along this journey and achieve what I have done.

TABLE OF CONTENTS

LIST OF FIGURES

LIST OF TABLES

LIST OF APPENDICES

LIST OF ABBREVIATIONS

AWD	All-Wheel-Drive
AWRB	All-Wheel-Regenerative Braking
BSFC	Brake Specific Fuel Consumption
DOF	Degree-of-freedom
DP	Dynamic Programming
ECMS	Equivalent Consumption Minimization Strategy
ECVT	Electronic-Continuous Variable Transmission
EM	Electric Machine
EPA	Environmental Protection Agency
EV	Electric Vehicle
FWD	Front-Wheel-Drive
HEV	Hybrid Electric Vehicle
ICE	Internal Combustion Engine
MG	Motor/Generator
MPP	Multi-Parametric Programming
OCV	Open Circuit Voltage
PEARS	Power-Weighted Efficiency Analysis for Rapid Sizing
PG	Planetary Gear
PHEV	Plug-in Hybrid Electric
PnG	Pulse-and-Glide
RWD	Rear-Wheel-Drive
SDP	Stochastic Dynamic Programming
SOC	State of Charge
2WD	Two-Wheel-Drive

ABSTRACT

Fuel efficiency standards in the ground transportation sector have been becoming more stringent over the previous decade worldwide. The power-split hybrid powertrain technology is one of the most promising solutions to meet those exigent standards. This technology has been successfully implemented in the passenger vehicle market, such as Toyota Prius, and demonstrated a fuel economy improvement of over 60%. In contrast, however, few hybrid electric light trucks are available, which is problematic given the fact that trucks are now more than 65% of light-duty vehicle sales in the United States. Additional performance requirements such as all-wheel-drive (AWD) also has not been explored adequately. Expanding the power-split hybrid technology to a broader market while satisfying all these requirements is imperative but challenging.

The main contributions of this dissertation includes, 1) we present a systematic design methodology that enables the exhaustive search of AWD power-split hybrid powertrains; 2) the concept of relaxed optimization for additional fuel reduction; 3) a systematic framework of control design that enables automated development of real-time control strategies and ensures near-optimal performance; in addition, 4) an experimental study to verify the theoretical development.

Designing AWD power-split hybrid powertrains involves searching over a large design space. Millions of designs are possible when considering collocations of all components including planetary-gear (PG) sets, an engine, electric motor(s), and clutches. Within the developed systematic design methodology, all possible designs can be generated through an automated modeling technique; exhaustively searching through all these designs then become possible. A systematic screening process is developed to screen for feasible designs, with respect to desired performance attributes; optimal designs then can be identified by checking their launching/towing performances together with fuel efficiencies. A case study on an imagined hybrid F-150 light truck demonstrates that the

developed methodology is able to identify dozens of better designs than parallel-hybrid baseline model.

Optimization is crucial for both design and control development. An optimization of hybrid electric powertrain is defined which allows load leveling among the power source (engine), electrical energy buffer (battery). Relaxed optimization is further defined and investigated when the mechanical energy buffer (vehicle kinetic energy) is also introduced. Analysis of these optimized results are used for design screening and control development.

By understanding the analysis of optimized results, a systematic framework is developed to generate a near-optimal real-time control strategy. A set of optimal controls is generated by analyzing the hybrid powertrain system firstly; the real-time control strategy is developed by constructing the policy from the optimal control set. Near-optimal results are achieved under this development framework.

With the establishment of the design and control development frameworks, an experimental study is performed to verify this theoretical development. Preliminary results project that the developed framework of hybrid technology implementation is able to identify designs achieving fuel consumption reduction of more than 50% compared to current conventional baseline models for truck applications.

CHAPTER 1
Introduction

1.1 Motivation

Fuel efficiency continues to be a top priority in transportation especially in the previous decade because of apprehension relative to CO_2 emissions and climate change. Stringent fuel economy policies have been proposed to improve fuel efficiency. As shown in Figure 1.1, fuel economy or greenhouse-gas emission standards from six major markets worldwide (listed at the bottom) have been established or proposed for passenger vehicles and light-commercial vehicles/light trucks [1-3]. The regulations in these markets, which encompass more than 80% of the global passenger vehicle sales, influence the business decisions of major vehicle manufacturers around the world and are among the most effective climate change mitigation measures that have been implemented over the past decade [1].

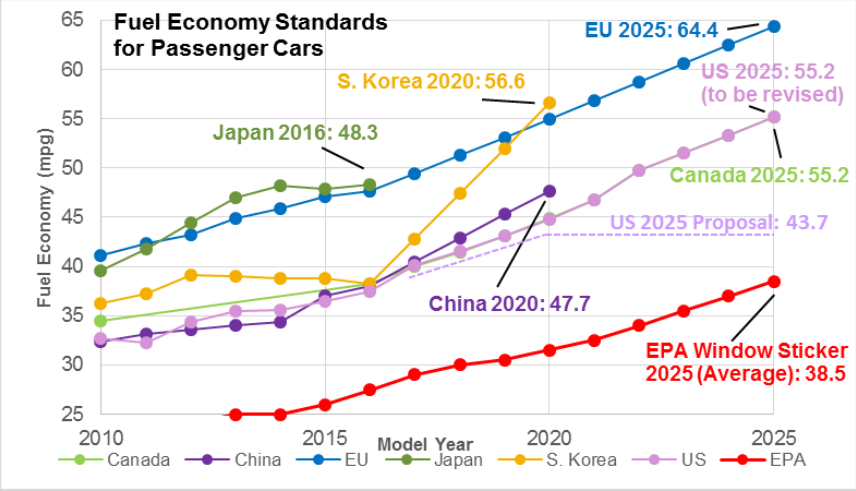

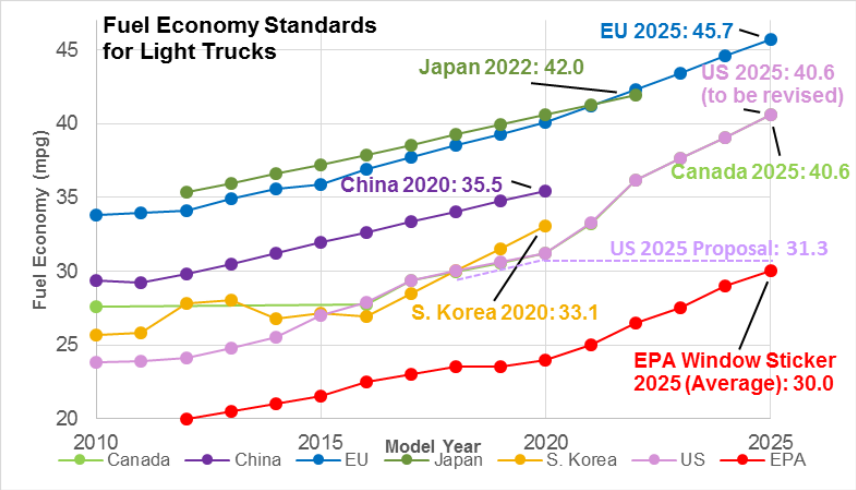

Figure 1.1 Average fuel economy standards for passenger cars and light trucks and corresponding projected achieved values for model years 2010-2025 [1-3]

It is challenging to meet these fuel economy standards. The projected fuel economy [2] for 2025 by the Environmental Protection Agency (EPA), highlighted in red in Figure 1.1, is over 20% tighter. To achieve these exigent standards, different technologies have been studied and developed. Among these, the hybrid powertrain technology is one of the most promising.

The hybrid powertrain technology has been successfully implemented in certain passenger cars. As shown in Figure 1.2, hybrid passenger cars currently available have attained fuel economy improvement of over 60% [4] compared with their conventional baseline models (equipped with an internal combustion engine only); this corresponds to a fuel economy sticker label of more than 50mpg (miles per gallon). Among full hybrids, models with power-split technology, such as Toyota Prius (2018) [4] and Toyota Hybrid Corolla (2019), exceed 58mpg. The achieved fuel economy sticker label indicates the hybrid powertrain technology has great potential to help the fleet meet those fuel economy standards.

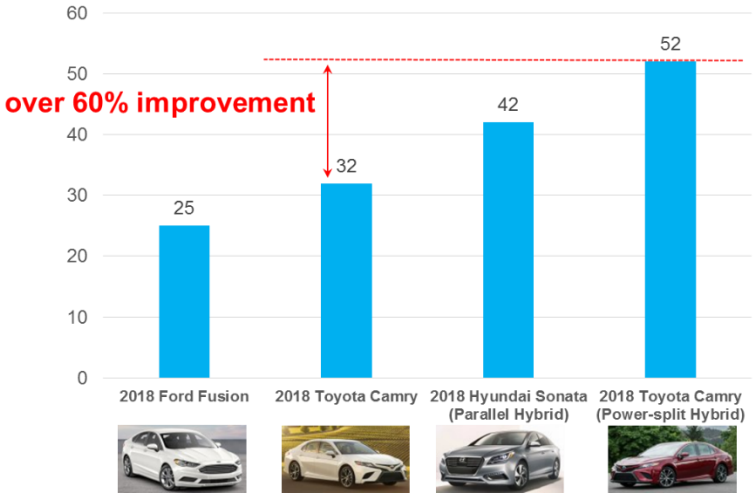

Figure 1.2 EPA fuel economy labels (combined; in mpg)

While there are successful passenger car models equipped with hybrid technology, in contrast, few strong hybrid light trucks have been available. Besides, the number of light trucks sold kept increasing in the past 8 years and in 2018 were more than twice those of passenger car models in the U.S. market, as indicated in Figure 1.3. Actions are required to expand the hybrid powertrain technology to broader markets, e.g., the light trucks.

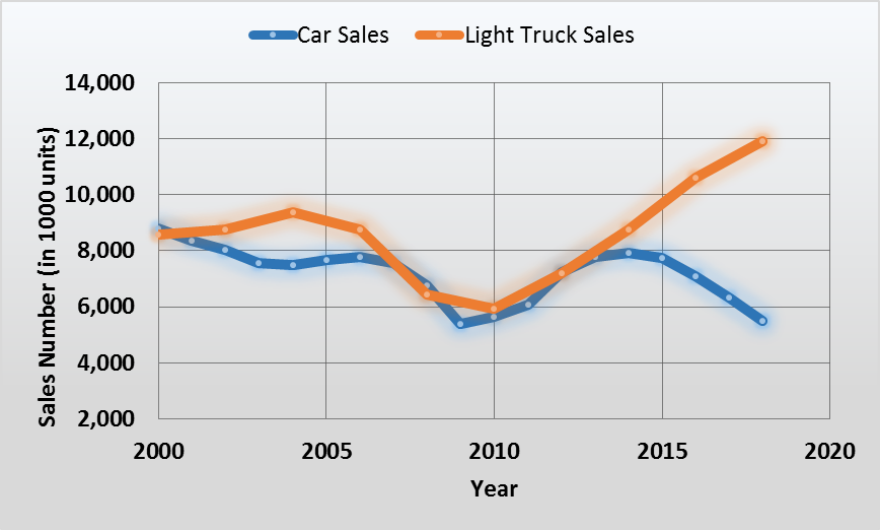

Figure 1.3 U.S. light vehicle sales [5, 6]

1.2 Background

1.2.1 Hybrid Powertrain Technologies Implementation

The implementation of hybrid technologies to light trucks require a broad set of topics to be considered (see Figure 1.4). The implementation is organized into two phases: design and control development. One important aspect in the design phase is performance. Tighter performance requirements including those related to launching, towing, and uphill grade, are expected [7]. All-wheel-drive is one desired attribute in the performance metric. The other important aspect in the design phase is fuel economy.

Given an identified hybrid powertrain design, in the control development phase, offline optimization is usually first solved. A real-time control strategy development may then be developed to approximate the behavior of the offline optimization results so it can be implemented. In the remaining section, aspects of each phase are to be explained and reviewed in the following sub-sections.

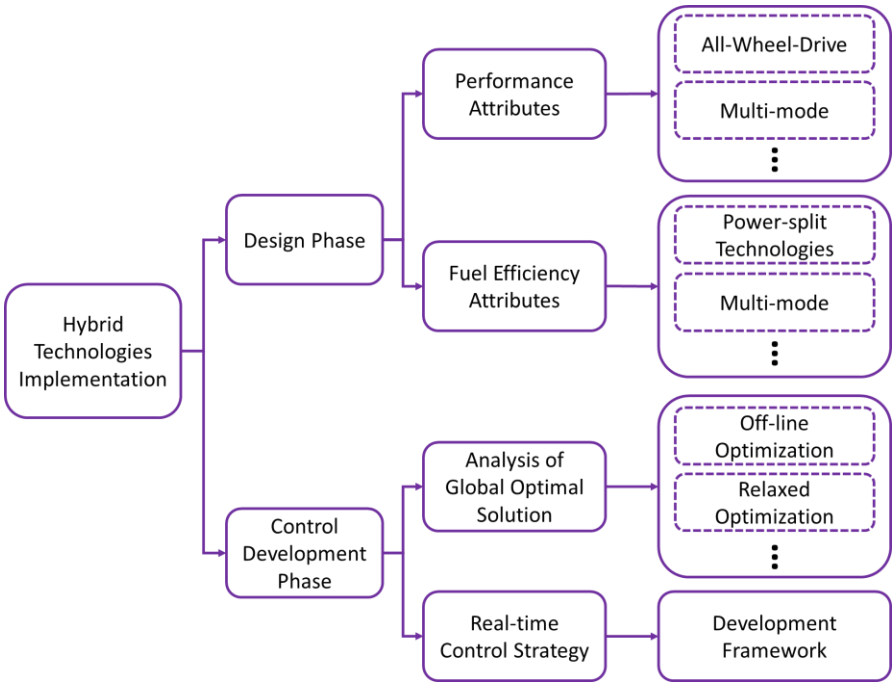

Figure 1.4 Implementation of hybrid technologies

1.2.2 AWD Hybrid Electric Vehicles

As one desired performance attribute, according to the Society of Automotive Engineers (SAE) standard J1952 [8] for the all-wheel-drive system classification, the all-wheel-drive (AWD) is defined if the drivetrain can deliver power to both axles (i.e., primary and secondary axles). In typical AWD powertrain systems available in the current market, the two output axles are connected to the front and rear wheels.

The gradeability and towing capacity of hybrid vehicles with AWD, especially on an uphill slope, are better two-wheel-drive (2WD) designs, as shown in Figure 1.5. The two output axles guarantee combined vehicle traction torque in all wheels regardless of the shift in the vehicle's center of gravity; consequently, a better traction performance in gradeability and towing capacity is achieved.

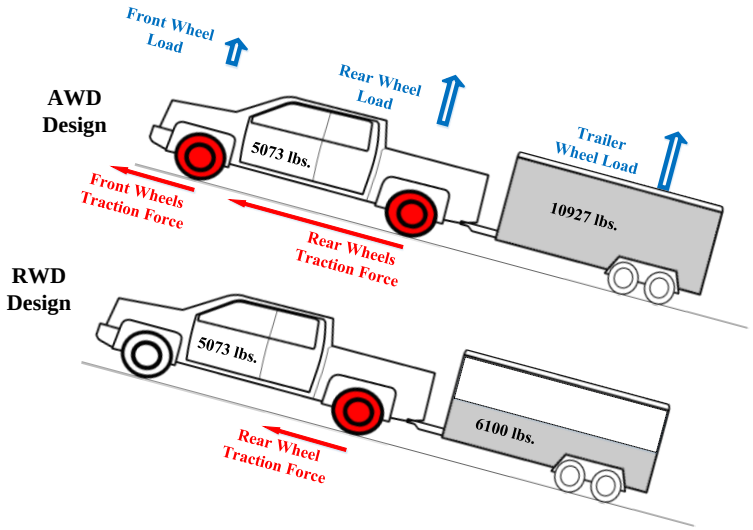

Figure 1.5 Launching and towing performance comparisons between AWD and RWD vehicle designs up a slope

One of the few AWD hybrid designs available on the market is Acura RLX Sport Hybrid [9] shown in Figure 1.6. This parallel hybrid design has three electric motors: two on the rear axle and one on the front axle. Other AWD hybrids are Toyota RAV4 Hybrid SUV [10] and Lexus RX Hybrid [11], which share the same design, as shown in Figure 1.7. This Toyota design is a power-split type AWD design, in which two motors are at the front axle for the electric-continuous variable transmission (ECVT) attribute and a motor at the rear axle for the AWD attribute.

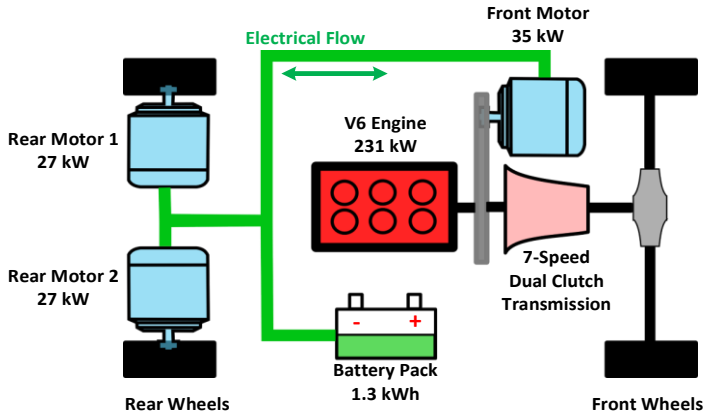

Figure 1.6 Design schematic of Acura RLX Sport Hybrid [9]

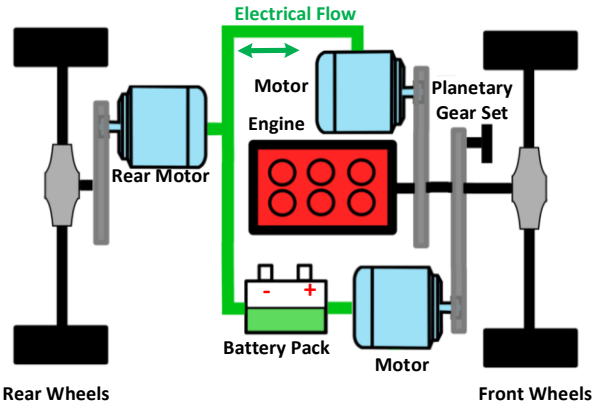

Figure 1.7 Design schematic of Toyota RAV4 Hybrid [10]

1.2.3 Power-split Hybrid Electric Vehicles

Mainly due to their superior fuel economy, the power-split hybrid powertrain technologies have been implemented on passenger cars and have secured more than 80% of the hybrid vehicle market share in calendar years 2016 and 2017 in the U.S. [12]. Typical power-split type designs utilize planetary-gear set(s), multiple clutches, two electric machines and one engine, such as those employed in Toyota Prius and Chevy Volt. The Toyota Prius 2010 [13] design is shown in Figure 1.8.

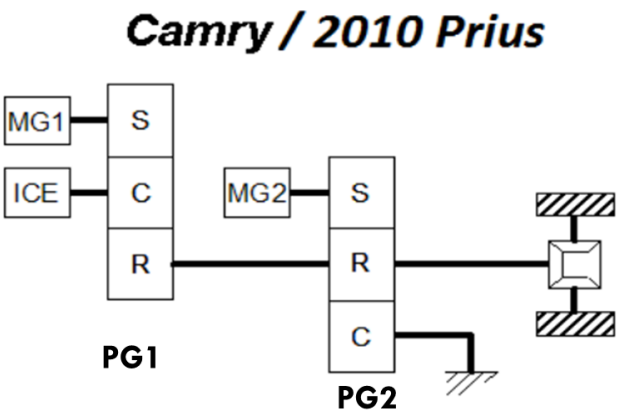

"EVALUATION OF THE 2010 TOYOTA PRIUS HYBRID SYNERGY DRIVE SYSTEM", M. Olszewski, Oak Ridge National Lab, 2011.

Figure 1.8 Toyota Prius (2010) design schematic example [13]

For a power-split vehicle with the ECVT attribute, the engine speed and torque can be controlled independent of the vehicle operating conditions. This control degree-of-freedom allows efficient engine operation as desired. In this dissertation, a systematic study of AWD power-split hybrid vehicles is performed from the modeling, control and design perspectives.

1.2.4 Control Strategy for Power-split Hybrid Electric Vehicles

In addition to configuration design, control strategy is also important to achieve superior fuel efficiency. The electric machine(s) supplement an electric power path: this aids in improving the fuel economy by engine right-sizing, load-leveling, and re-generative braking. However, the additional power component(s) add complexity to the powertrain system: the degree-of-freedom (DOF) of the powertrain system increases as the control component input(s) are added. To control this hybrid system, a control structure is generally used as shown in Figure 1.9. The control strategy determines the energy flow within the hybrid system and coordinates the torques of all components to balance the planetary gear set(s). Accordingly, the components' commands are then executed by their own controllers.

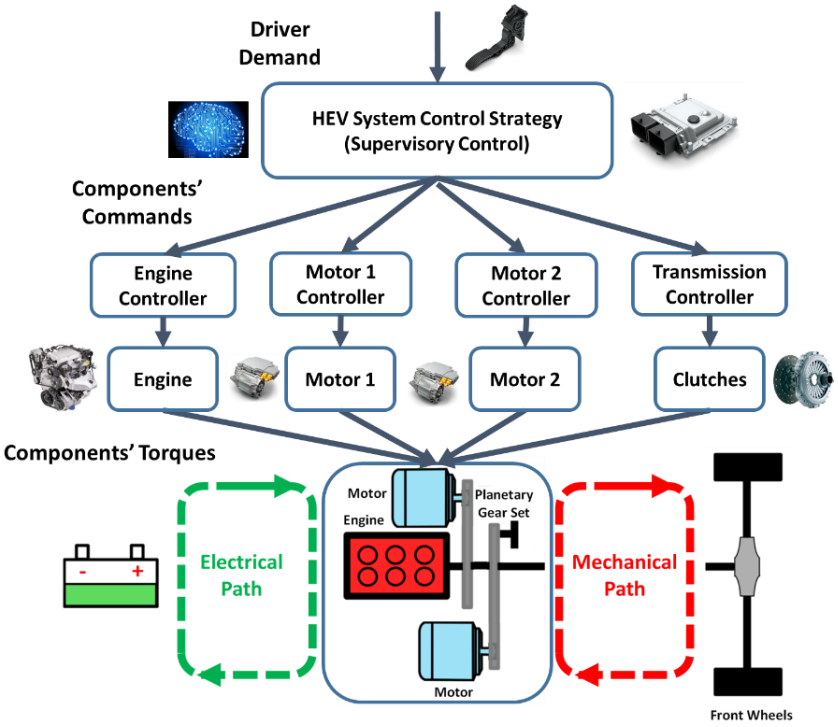

Figure 1.9 Generic control structure for power-split HEV powertrain systems

An optimized control strategy is crucial because it ensures that the hybrid powertrain system operates efficiently. The optimal results are obtained through solving the off-line optimization problem under a defined drive cycle. The optimal results become a benchmark as the best performance of the given hybrid powertrain and show how the powertrain operates to achieve the best results. Real-time implementable control strategies will need to be developed to achieve fuel economy as close as possible to the offline benchmark value.

1.2.5 Powertrain Control with Vehicle Speed Relaxation

The fuel economies are assessed under defined drive cycles. Most studies [14-20] on the powertrain controls, for both conventional and hybrid vehicles, have assumed that the vehicles follow a desired drive cycle exactly. However, real-world vehicles do not exactly follow the defined drive cycles. In fact, the Environmental Protection Agency (EPA) defined a speed tolerance for such drive cycles as shown in Figure 1.10; it is also cited by SAE standard J1711 [21]. The variation of vehicle speed within a defined speed tolerance is acceptable.

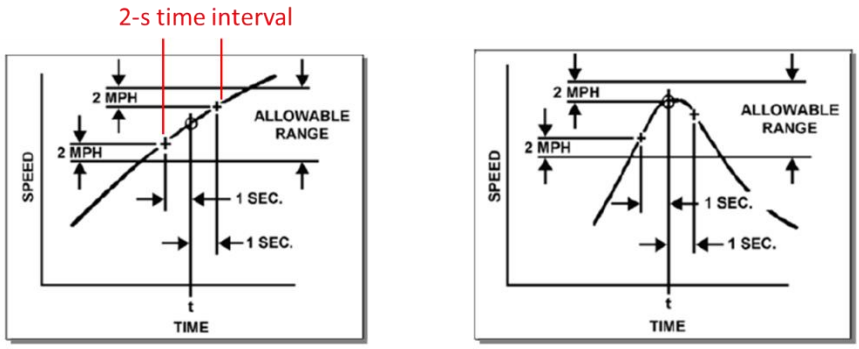

Figure 1.10 EPA-defined speed tolerance [21]

The consideration of exploring this concept is crucial especially for applications of connected and automated vehicles (CAVs). With information of surrounding vehicles, traffic lights, and speed limit available, the controlled automated vehicles do not need to follow those defined drive cycles nor the speed of leading vehicle precisely. Instead, a new speed profile can be optimized and generated as long as limits from information of connectivity are not exceeded. The automated vehicle can be control to adapt to this optimized profile for additional fuel saving [22-24], as shown in Figure 1.1.

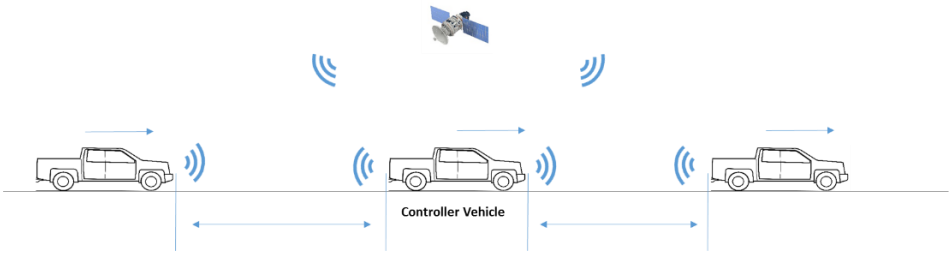

Figure 1.11 CAV scenario: optimizing a new vehicle speed profile for a controlled vehicle to follow

By utilizing this speed tolerance, the powertrain component(s) have higher degree-of-freedom than the original control optimization problem, because the speed constraint is relaxed. We call these constraint-relaxed problems the “relaxed optimization” problem.

Additional fuel consumption reduction was observed when utilizing this relaxed optimization concept. For example, the start/stop coasting (SSC) strategy from Bosch [25, 26], shown in Figure 1.12, allows the speed of tested vehicle to be within 2-5 mph of the desired speed; real-world test results exhibit a fuel consumption reduction as much as 19%. The pulse-and-glide (PnG) strategy [24, 27-29] in the highway cruising can result in a fuel

consumption reduction of up to 55%. Other studies on controls that utilize vehicle speed, have also reported fuel benefits in using this concept [22-30] as shown in Figure 1.13.

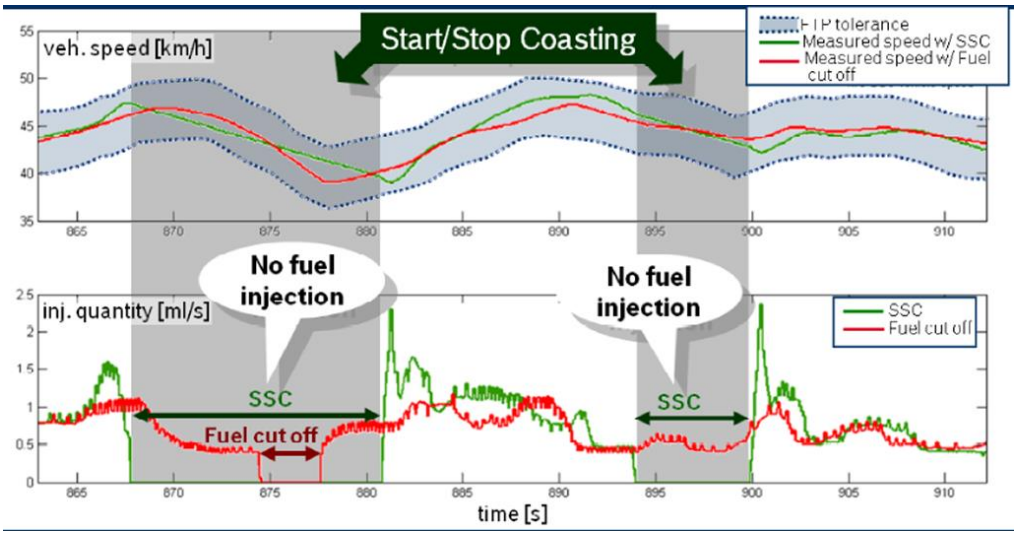

Figure 1.12 Vehicle speed and fuel rate test results using the Bosch Start/Stop Coasting strategy [25, 26]

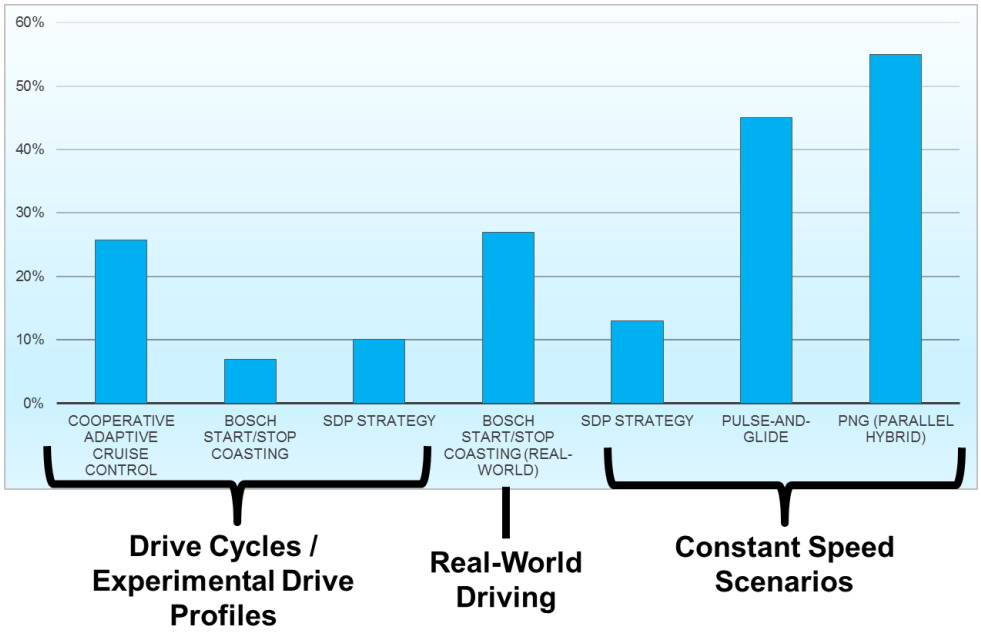

Figure 1.13 Fuel consumption reductions resulting from relaxed optimization in different studies

In this dissertation, we will incorporates this relaxation concept of the power-split hybrid powertrains, including both 2WD and AWD configurations. The systematic control strategy is developed from the analysis of this optimal control problem with vehicle relaxation.

1.3 Literature Review

1.3.1 Automated Modeling of Hybrid Powertrains

The establishment of a proper modeling method is an essential element for the model-based development of HEV design and powertrain control. A proper mathematical model of the hybrid powertrain enables the systematic modeling of all possible hybrid powertrain designs and systematic development of control strategy.

In 1999, Rizzoni et al. [31] proposed a system-oriented approach to the modeling and simulation of hybrid vehicles based on an energy conversion model of drivetrain subsystems. In 2007, Liu [32] employed a matrix representation to depict a power-split hybrid powertrain (Prius) dynamic in a universal format and to reveal patterns inside the representation. With the proposed representation and patterns, the automated modeling of power-split hybrid powertrain becomes possible by constructing the HEV dynamics in matrix form (Figure 1.14). In 2015, Zhang further extended the automated modeling technique to multi-mode power-split designs by incorporating all possible clutch collocations between two planetary gears (PGs) [33-36]. For multi-mode power-split hybrid designs, the system design procedures have been laid out: automated modeling, configuration screening, drivability screening and fuel economy evaluation.

$$\left[\begin{array}{cccc:cc} I_e+I_{c1} & 0 & 0 & 0 & R_1+S_1 & 0 \\ 0 & \frac{R_{tire}^2}{K^2}m+I_{c2} & 0 & 0 & 0 & R_2+S_2 \\ 0 & 0 & I_{MG1}+I_{s1} & 0 & -S_1 & 0 \\ 0 & 0 & 0 & I_{MG2}+I_{r1}+I_{s2} & -R_1 & -S_2 \\ \hdashline R_1+S_1 & 0 & -S_1 & -R_1 & 0 & 0 \\ 0 & R_2+S_2 & 0 & -S_2 & 0 & 0 \end{array}\right] = \left[\begin{array}{cc} J & D \\ D^T & 0 \end{array}\right]$$

D-matrix

$$\left[\begin{array}{cc} J & D \\ D^T & 0 \end{array}\right]\left[\begin{array}{c} \dot{\Omega} \\ F \end{array}\right] = \left[\begin{array}{c} T \\ 0 \end{array}\right]$$

Figure 1.14 Universal format of model matrix for power-split hybrid powertrain

Adding additional output axle to a planetary gear system can improve driving performance. To explore the entire design space (including multiple operating modes) and identify the optimal design, a systematic modeling approach is required to handle the

massive number of design candidates. For instance, for a double PG planetary gear hybrid powertrain system with two output axles, there can be over 80,000 designs and up to 18 million design candidates if component sizing is considered. Therefore, it is considerably crucial to have an automated modeling method that represents each design in order to perform an exhaustive search through the large design space.

1.3.2 Solving the Offline Optimal Control Problem

The control of hybrid vehicles typically has a two-level hierarchical architecture: the components' control/regulation and the supervisory control as already indicated in Figure 1.9 in the previous section. In general, the optimal control problem of the HEV system refers to solving the optimization problem of supervisory control, also known as energy management strategy. Algorithms for solving this optimal control problem can be categorized into three types: heuristic/rule-based control, instantaneous optimization, and horizon optimization.

Horizon optimization is usually used to obtain the globally optimal/near-optimal results of the control problem offline, these results are critical for understanding the performance of each HEV design and having a fair comparison.

A popular method for solving horizon optimization problems is dynamic programming (DP). The DP concept was proposed by Richard Bellman in the 1940s and refined by Bellman himself in 1954 and 1963 [37]. This global optimization method did became very popular in HEV control design in the previous two decades after the work of Brahma et al. in 2000 and Lin et al. in 2003 [20]. Extensive studies have been conducted [32-34, 36, 38, 39] over similar topics because the DP can easily handle the non-convexity and non-linearity of constrained problems easily. However, this method continues to suffer from the curse of dimensionality, as the number of controls and states increase; the utilization of this method to solve for higher DOF problems, such as the multi-mode hybrid powertrain, is rare.

In order to handle the issues of evaluating large-scale designs, the method developed by Zhang, the power-weighted efficiency analysis for rapid sizing (PEARS) [35], which is a near-optimal and computationally efficient method that yields near-optimal results but four orders of magnitude faster than the DP. The idea of this method is to reduce

the number of continuous controls and states of the optimization problem by pre-optimizing these continuous variables given each discrete state, for instance, the operating mode in this application. Consequently, the DOF of the optimization problem can be reduced; thus, a significantly shorter computational time is possible. This method has become effective and efficient for the HEV design evaluation.

However, when certain continuous controls and states, such as vehicle speed and vehicle range, are difficult to pre-optimize, the curse of dimensionality of PEARS persists. To appropriately resolve the high DOF optimal control problem of AWD multi-mode power-split hybrid vehicles, a fast and reliable optimization method is necessary.

A possible approach is multi-parametric programming (MPP), which refers to a class of optimization problems that involving bounded uncertainty and/or variability within the mathematical model. The concept of MPP was proposed by Pistikopoulos et al. [40]. It pertains to a hard-constrained multi-stage problem in a DP fashion; therefore, global optimality is guaranteed. The optimal solutions for every possible realization of the state vector are pre-computed as explicit functions. With this technique, the discretization of controls and states is avoided, the computational effort will be significantly reduced, and the curse of dimensionality (which exists in the DP) will cease to be a barrier.

All these HEV control approaches have pros and cons. When utilizing any of these methods, the limitation of the selected technique should be thoroughly understood to ensure proper implementation.

1.3.3 Real-time Control Strategy for HEV Powertrain and Vehicle Speed Relaxation

The heuristic/rule-based control and instantaneous optimization have been used in the real-time control strategy for the HEV powertrain and vehicle control.

The instantaneous optimization approaches minimize cost functions on the basis of current information; the equivalent consumption minimization strategy (ECMS) is one of the best-known examples. In this approach, electric power is transformed into an equivalent fuel consumption rate. By minimizing the instantaneous equivalent fuel consumption, the resulting algorithm achieves an optimized selection between engine power and battery power. The pioneering work was done by Kim et al. in 1999 and Paganelli et al. in 2000.

Rizzoni et al. [41] provided the relationship between the results of this method and the global optimal solution, together with the required condition. This methodology can be improved by introducing a periodically refreshed conversion factor on the basis of the road load condition and the state-of-charge (SOC) level [42].

The heuristic control algorithms, such as control rules, are typically based on the concept of load-leveling, which attempts to operate the internal combustion engine in an efficient region and uses the reversible energy storage (e.g., battery or vehicle inertia) as a load-leveling device to provide the rest of the power demand. Some rule-base algorithm examples were demonstrated by Jalil et al. [17] and Lin et al. [43].

With a thorough comprehension of the system and appropriate design, the rule-based control can exhibit good performance. Bosch [25, 26] developed a rule-based strategy called start/stop coasting (SSC). The excessive engine torque pulses the vehicle speed beyond the desired value; this eliminates the combustion engine's drag torque during idling and allows the vehicle to coast down.

Li et al. [28] developed a pulse-and-glide (PnG) strategy both for a conventional powertrain [24, 28, 29] and a parallel hybrid powertrain [27], as shown in Figure 1.15. The mechanism of pulse-and-glide [28], shown in Figure 1.16, take advantage of the non-convexity of the engine fuel map. This PnG strategy was also verified to be optimal/near-optimal by comparing results from solving the optimal control problem.

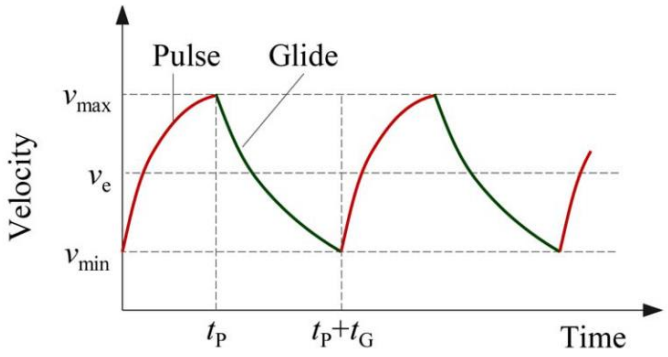

Figure 1.15 Pulse-and-Glide strategy

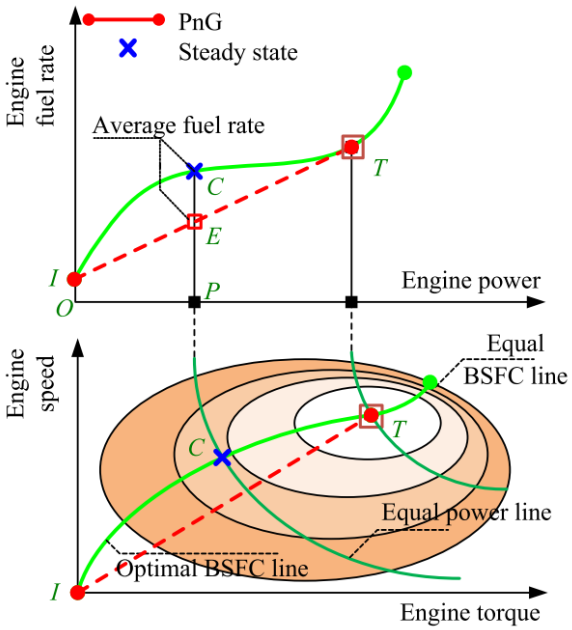

Figure 1.16 Pulse-and-Glide mechanism [29]

1.4 Contributions

Research developed in this dissertation aims to expand hybrid technologies to light trucks. It focuses on design and control strategy development of AWD multi-mode power-split which has not been systematically investigated before. The main contributions of the dissertation are summarized below:

- A systematic design process was developed for the AWD multi-mode power-split hybrid vehicles. A new modeling and screening formulation was established for AWD multi-mode power-split hybrid vehicles; this formulation distinguishes the development from existing research on 2WD and has not been explored before. The design process highlights a four-step methodology that uses automated modeling, exhaustive search in the design space, and a near-optimal control strategy to obtain optimal designs. Drivability performance and fuel economy are both considered in the evaluation stage.
- The concept of relaxed optimization for vehicle control was defined and solved. The formulations, solutions and analysis of this concept for both conventional and hybrid vehicles were systematically developed, which have not been systematically

explored. Enhanced fuel consumption reduction was demonstrated with additional relaxed constraints (vehicle speed and range). The MPP method was introduced to solve the high-dimensional non-linear non-convex optimization problem and the relaxed optimization for AWD power-split hybrid vehicles. The developed problem formulation, transformation, and solution procedure exhibit a methodology to solve this class of vehicle control optimization problems even if the problem dimension is high (6-7 variables), which is difficult to be solved using commonly explored methods (e.g., dynamic programming). The relationship and analysis between the optimal control and the resulting state trajectory were revealed from the analytical solution.

- A real-time control strategy design framework for hybrid powertrain was developed. The distinguishing framework demonstrated how to analyze the powertrain system, generate system optimal control sets, and systematically construct a near-optimal control strategy. Different from existing real-time control methods that either require prior information of speed profile to ensure near-optimal or require intensive computation for algorithm training/learning. Different HEV models, including the AWD power-split powertrain system are used to demonstrate the development and results. This framework can be expanded easily to all powertrain control design problems.
- Experimental study for the developed of framework for design and control development was performed. A prototype multi-mode power-split hybrid powertrain is developed together with the control strategy. Experiments are performed to validate this proposed design concept that achieves a fuel consumption reduction of over 50%.

1.5 Outline of the Dissertation

This dissertation is organized as follows. In Chapter 2, an automated modeling process for multi-mode power-split hybrid vehicles is presented for the AWD and the 2WD hybrid vehicles. In Chapter 3, a systematic design methodology for multi-mode power-split hybrid vehicles is shown, and the AWD hybrid powertrain is used as a design case study. In Chapter 4, the concept and formulation of relaxed optimization are presented to demonstrate the additional fuel benefits. In Chapter 5, the multi-parametric programming method is introduced and utilized to solve the relaxed optimization problem, together with

a case study on the AWD hybrid powertrain. In Chapter 6, a near optimal HEV control strategy is demonstrated based on understanding the relaxed optimization and analytical solutions from Chapter 5. In Chapter 7, the development of a prototype HEV medium duty delivery truck is described. In Chapter 8, conclusion and future work are presented.

The building-blocks of the methodologies presented in this dissertation is shown in Figure 1.17.

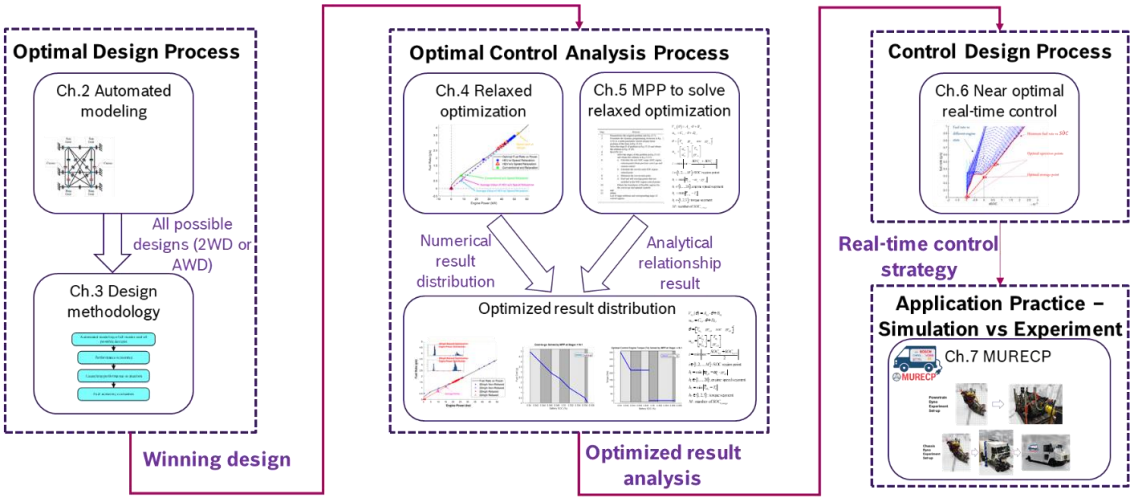

Figure 1.17 Flow-chart of organization development of this dissertation

CHAPTER 2
Automated Modeling of AWD Multi-Mode Power-Split Hybrid Vehicles

The proper modeling of the hybrid powertrains is an essential first step of implementing hybrid technologies. Including the very important goal of generating models of all possible designs automatically. In this chapter, a modeling technique for constructing mathematical models of power-split hybrid powertrains is demonstrated. Built upon prior studies, the modeling technique used in this dissertation is capable of automatically modeling both AWD multi-mode power-split hybrid powertrains and 2WD designs. To better demonstrate how the modeling technique works, an AWD power-split design is employed as an example.

Figure 2.1 illustrates an example design of the AWD power-split architecture patented by Toyota [44]. One of the key feature of power-split powertrains is that the double PG set acts as a continuous variable transmission (CVT).

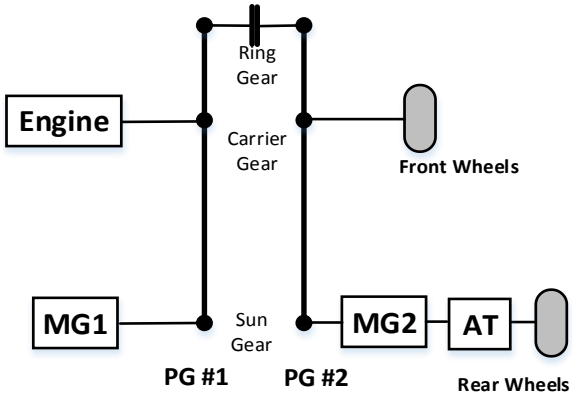

Figure 2.1 AWD power-split hybrid vehicle design example [44]

The aforementioned AWD power-split hybrid powertrains can be modeled through a matrix that represents the complete dynamic and includes the connection information of

components. This technique is used throughout this dissertation to model and simulate the powertrain dynamics as well as design screening.

The dynamic equations of the powertrain are shown in Eq. (2.1) where $T_{(\cdot)}$ denotes torque of components, $\dot{\omega}_{(\cdot)}$ denotes the angular acceleration, $I_{(\cdot)}$ denotes the corresponding inertia, $F_{(\cdot)}$ denotes internal gear force of the corresponding PG set, and $R_{(\cdot)}$ and $S_{(\cdot)}$ are the radii of the ring gear and sun gear, respectively.

$$\begin{bmatrix} I_e+I_{c1} & 0 & 0 & 0 & 0 & 0 & R_1+S_1 & 0 & 0 \\ 0 & I_F+I_{c2} & 0 & 0 & 0 & 0 & 0 & R_2+S_2 & 0 \\ 0 & 0 & I_R+I_{mg2}+I_{s2} & 0 & 0 & 0 & 0 & -S_2 & 0 \\ 0 & 0 & 0 & I_{mg1}+I_{s1} & 0 & 0 & -S_1 & 0 & 0 \\ 0 & 0 & 0 & 0 & I_{r1} & 0 & -R_1 & 0 & 1 \\ 0 & 0 & 0 & 0 & 0 & I_{r2} & 0 & -R_2 & -1 \\ R_1+S_1 & 0 & 0 & -S_1 & -R_1 & 0 & 0 & 0 & 0 \\ 0 & R_2+S_2 & -S_2 & 0 & 0 & -R_2 & 0 & 0 & 0 \\ 0 & 0 & 0 & 0 & 1 & -1 & 0 & 0 & 0 \end{bmatrix} \cdot \begin{bmatrix} \dot{\omega}_e \\ \dot{\omega}_F \\ \dot{\omega}_R \\ \dot{\omega}_{mg1} \\ \dot{\omega}_{r1} \\ \dot{\omega}_{r2} \\ F_1 \\ F_2 \\ T_{cl1} \end{bmatrix} = \begin{bmatrix} T_e \\ -T_F \\ -T_R+T_{mg2} \\ T_{mg1} \\ 0 \\ 0 \\ 0 \\ 0 \\ 0 \end{bmatrix} \tag{2.1}$$

Equation (2.1) is the complete dynamics of the powertrain. The uniqueness of each design enables automated modeling possible, the format allows screening and mode analysis, and the complete dynamics can be used to evaluate the response of the powertrain.

When a design is formulated by a matrix which represents its dynamics, dynamic performance requirements, such as acceleration, top speed, gradeability, and towing capacity, can be address. However, the capability to handle requirements for life-time usage or manufacturing feasibility might be limited. In this dissertation, dynamic performance requirements are highlight. Therefore, using the above matrix formulation is appropriate.

In this dissertation, each design candidate of the AWD power-split hybrid vehicle powertrains consists of an internal combustion engine, two electric motors, a battery pack, two PG sets, two output shafts, and three clutches. The details of constructing the complete model dynamics and assembling it into the representation in Eq. (2.1) are described in the remaining of this chapter. The dynamics of the AWD power-split hybrid powertrain is first developed. Then, the automated modeling procedure is described for generating all possible designs.

2.1 Modeling Power-Split Hybrid Powertrains

2.1.1 Vehicle Dynamics Model

A quasi-static model is used to simulate the dynamics of the vehicle. Figure 2.2 shows the free-body diagram of the longitudinal vehicle motion on a flat road. In the figure, the vehicle has a body mass m_b (without wheels) and a wheel mass m_w of both front and rear axles; the wheel inertia is denoted as I_w. The gravitational constant is g, the aerodynamic force is D_A, T is the axle output torque, K_z is the vertical force between the wheels and body, K_x is the longitudinal force between the wheels and body, N_z is the tire reaction force in the vertical direction, and F_x is the tire reaction force in the longitudinal direction. The subscripts f and r refer to the front and rear axles, respectively.

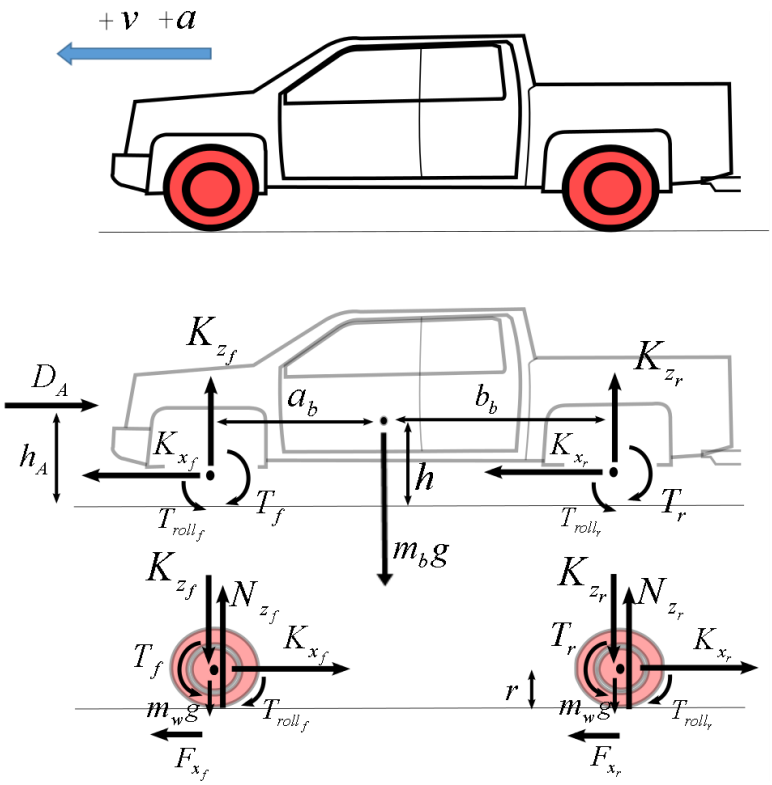

Figure 2.2 Free-body diagram of longitudinal vehicle motion on a flat road

The longitudinal dynamics and rotational dynamics of the vehicle body, front wheels, and rear wheels are given in Eqs. (2.2) – (2.10).

$$K_{x_f} + K_{x_r} - D_A = m_b a \tag{2.2}$$

$$K_{z_f} + K_{z_r} = m_b g \tag{2.3}$$

$$\begin{aligned} &-K_{z_f} a_b + K_{z_r} b_b - D_A (h_A - h) - \left(K_{x_f} + K_{x_r}\right) \cdot (h - r) \\ &+ T_f - T_{roll_f} + T_r - T_{roll_r} = 0 \end{aligned} \tag{2.4}$$

$$T_f - F_{x_f} r - T_{roll_f} = I_w \dot{\omega}_f \tag{2.5}$$

$$F_{x_f} - K_{x_f} = m_w a \tag{2.6}$$

$$N_{z_f} - K_{z_f} - m_w g = 0 \tag{2.7}$$

$$T_r - F_{x_r} r - T_{roll_r} = I_w \dot{\omega}_r \tag{2.8}$$

$$F_{x_r} - K_{x_r} = m_w a \tag{2.9}$$

$$N_{z_r} - K_{z_r} - m_w g = 0 \tag{2.10}$$

By defining the total mass M, the total rolling resistance T_{roll}, and rear-to-front torque ratio α between T_f and T_r in Eqs. (2.11) – (2.13), the two axle output torques (T_f and T_r) can be expressed as Eqs. (2.14) and (2.15), respectively.

$$M = m_b + 2m_w \tag{2.11}$$

$$T_{roll} = T_{roll_f} + T_{roll_r} \tag{2.12}$$

$$T_f = T_r \alpha \tag{2.13}$$

$$T_f = \frac{\alpha}{\alpha + 1}\left[Mar + I_w \dot{\omega}_f + I_w \dot{\omega}_r + T_{roll} + D_A \right] \tag{2.14}$$

$$T_r = \frac{1}{\alpha + 1}\left[Mar + I_w \dot{\omega}_f + I_w \dot{\omega}_r + T_{roll} + D_A \right] \tag{2.15}$$

The aerodynamic forces in Eqs. (2.14) and (2.15) can be calculated from

$$D_A = \frac{1}{2} \rho C_d A v^2 \tag{2.16}$$

where ρ is the air density, C_d is the drag coefficient, and A is the maximum vehicle cross sectional area. In this dissertation, the tire slip is not considered for simplification of the problem. The average accelerations of the to-be-evaluated drive cycles (UDDS and HWFET) are 0.4 and 0.17 m/s^2. These accelerations correspond to slip ratios of approximately 0.04 and 0.017, using the relationship of slip ratio and tire force in Figure 2.3 [45]. These slip ratios are smaller enough; therefore, their effects are neglected. Hence, all wheels have the same angular speed given by Eq. (2.17).

$$\omega_f = \omega_r = \frac{v}{r} \tag{2.17}$$

Table 2.1 Average Accelerations of Different Drive Cycles

Drive Cycles	Average Acceleration (m/s^2)
UDDS	0.40
HWFET	0.17

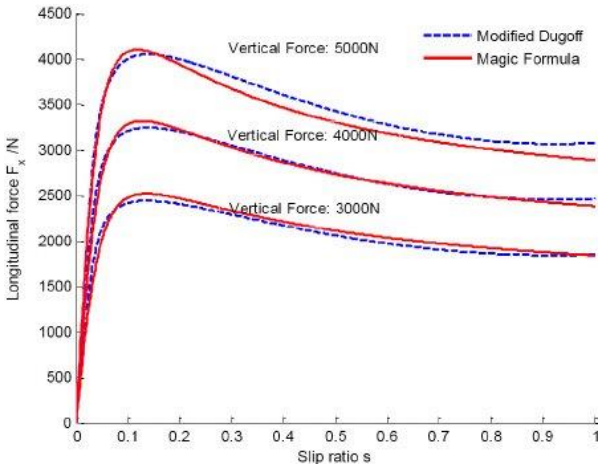

Figure 2.3 Longitudinal tire force on different road conditions [45]

2.1.2 Engine and Electric Motor Models

The fuel rate $\dot{m}_f$ is obtained from a static look-up table calculated from the brake specific fuel consumption (BSFC) map of the 3.6L boosted engine; the map is shown in Figure 2.4. The constraints of engine speed ω_e and torque T_e are indicated in the BSFC map and considered throughout the design process.

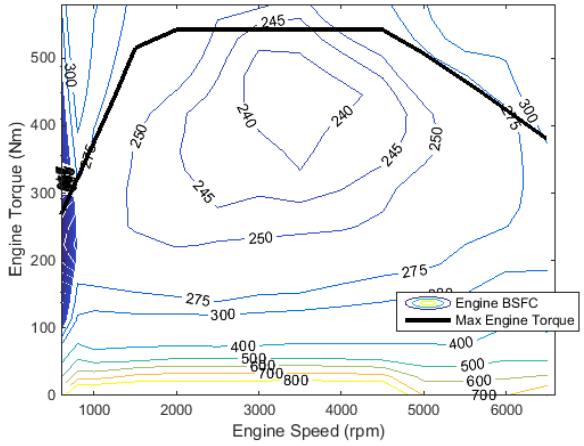

Figure 2.4 Engine BSFC map

Similarly, the efficiency of the two electric machines are obtained from a look-up table based on the efficiency map shown in Figure 2.5. Given the electric motor torques, T_{MG1} and T_{MG2}, and motor speeds, ω_{MG1} and ω_{MG2}, the power of the two electric machines is shown in Eq. (2.18), where η^{k1}_{MG1} and η^{k2}_{MG2} are the efficiency of the two motors,

respectively. If the electric machine is motoring, then *k1* and *k2* will be -1; if it is generating, then *k1* and *k2* are 1.

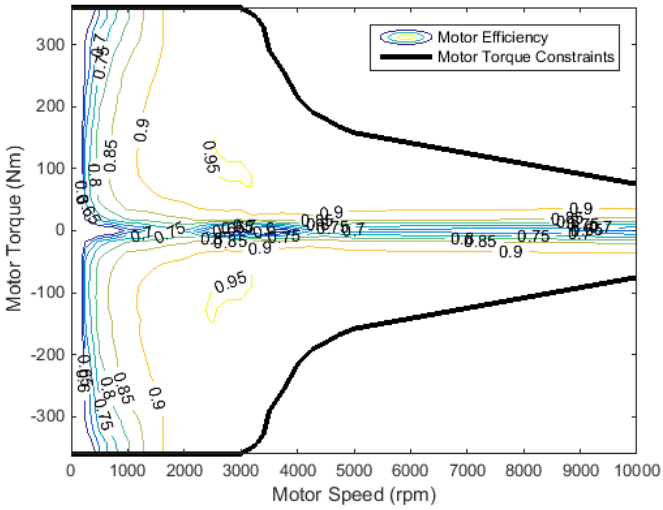

Figure 2.5 Efficiency map of electric motor

$$P_{elect} = T_{MG1}\omega_{MG1}\eta_{MG1}^{k1} + T_{MG2}\omega_{MG2}\eta_{MG2}^{k2} \tag{2.18}$$

2.1.3 Battery Model

The battery is modeled as a simple open-circuit voltage with a constant internal resistance. The battery state of charge (SOC) dynamics is described in Eq. (2.19).

$$\dot{SOC} = -\frac{V_{oc} - \sqrt{V_{oc}^{\ 2} - 4R_{bat}P_{elect}}}{2 \cdot R_{bat}} \tag{2.19}$$

2.1.4 PG Model

A typical PG set together with its equivalent lever diagram is shown in Figure 2.6. The three nodes in the lever diagram represents the ring gear, carrier gear, and sun gear of this PG; each node can be connected to a powertrain component. The kinematics of a PG set is governed by Eq. (2.20).

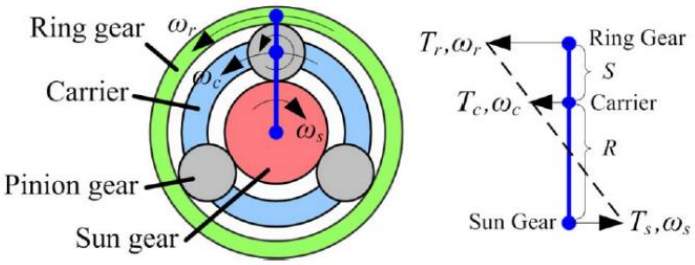

Figure 2.6 PG set and its lever diagram

$$\omega_s \cdot S + \omega_r \cdot R = \omega_c \cdot (R + S) \tag{2.20}$$

where ω_r, ω_c, and ω_s are the speeds of the ring gear, carrier, and sun gear, respectively. R and S refer to the radii of the ring gear and sun gear, respectively.

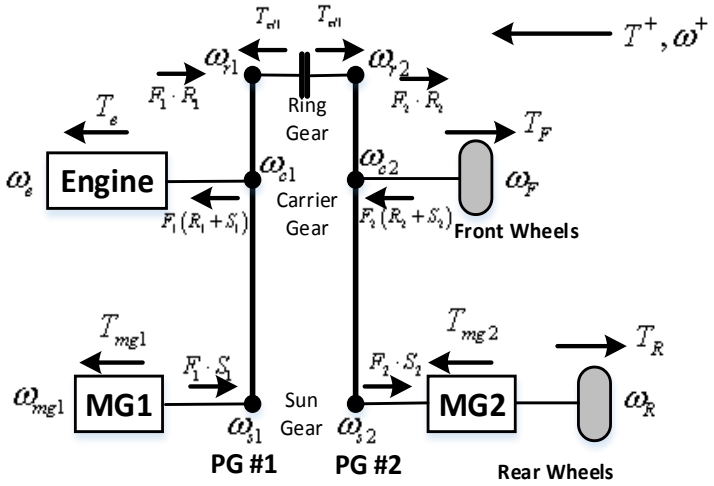

Figure 2.7 Lever diagram of Toyota AWD patent [44] (excluding the automated transmission) with significant forces and torques labeled

2.1.5 Complete Dynamics of Power-Split Hybrid Powertrain Using Matrix Representation

Given the components, the dynamics (excluding the battery dynamics) of an AWD power-split hybrid design can be represented in matrix form. To better describe the automated modeling technique, the patented Toyota design with two output shafts [44] is used (excluding the automatic transmission) shown in Figure 2.7 is used as an illustration. The dynamic equations of this powertrain are given by Eqs. (2.21) and (2.22) where $I_{(\cdot)}$

denotes the corresponding inertia, and $F_{(\cdot)}$ denotes the internal gear force of the corresponding PG set.

$$\begin{aligned}
&T_e + F_1\left(R_1 + S_1\right) = \dot{\omega}_e\left(I_e + I_{c1}\right)\\
&\left(-T_F\right) + F_2\left(R_2 + S_2\right) = \dot{\omega}_F\left(I_F + I_{c2}\right)\\
&T_{mg2} + \left(-T_R\right) + F_2\left(-S_2\right) = \dot{\omega}_R\left(I_R + I_{mg2} + I_{s2}\right)\\
&T_{mg1} + F_1\left(-S_1\right) = \dot{\omega}_{mg1}\left(I_{mg1} + I_{s1}\right)\\
&F_1\left(-R_1\right) + T_{cl1}\cdot 1 = \dot{\omega}_{r1}\cdot I_{r1}\\
&F_2\left(-R_2\right) + T_{cl1}\cdot\left(-1\right) = \dot{\omega}_{r2}\cdot I_{r2}
\end{aligned} \tag{2.21}$$

$$\begin{aligned}
&\left(R_1 + S_1\right)\dot{\omega}_e = R_1\dot{\omega}_{r1} + S_1\dot{\omega}_{mg1}\\
&\left(R_2 + S_2\right)\dot{\omega}_F = R_2\dot{\omega}_{r2} + S_2\dot{\omega}_{mg2}\\
&\dot{\omega}_{r1} - \dot{\omega}_{r2} = 0
\end{aligned} \tag{2.22}$$

T_F and T_R are the equivalent vehicle torques at the front and rear wheels which can be expressed in Eqs. (2.23) and (2.24) based on Eqs. (2.14) and (2.15), respectively. Similarly, the equivalent front wheel and rear wheel inertias can be expressed in Eqs. (2.25) and (2.26), respectively.

$$T_F = \frac{\alpha}{\alpha+1}\left(Mar + T_{roll} + D_A\right) \tag{2.23}$$

$$T_R = \frac{1}{\alpha+1}\left(Mar + T_{roll} + D_A\right) \tag{2.24}$$

$$I_F = \frac{\alpha}{\alpha+1}\left(I_f + I_r\right) \tag{2.25}$$

$$I_R = \frac{1}{\alpha+1}\left(I_f + I_r\right) \tag{2.26}$$

Equations (2.21) and (2.22) can be rearranged into the matrix representation in Eq. (2.27).

$$\begin{bmatrix} I_e + I_{c1} & 0 & 0 & 0 & 0 & 0 & R_1 + S_1 & 0 & 0 \\ 0 & I_F + I_{c2} & 0 & 0 & 0 & 0 & 0 & R_2 + S_2 & 0 \\ 0 & 0 & I_R + I_{mg2} + I_{s2} & 0 & 0 & 0 & 0 & -S_2 & 0 \\ 0 & 0 & 0 & I_{mg1} + I_{s1} & 0 & 0 & -S_1 & 0 & 0 \\ 0 & 0 & 0 & 0 & I_{r1} & 0 & -R_1 & 0 & 1 \\ 0 & 0 & 0 & 0 & 0 & I_{r2} & 0 & -R_2 & -1 \\ R_1 + S_1 & 0 & 0 & -S_1 & -R_1 & 0 & 0 & 0 & 0 \\ 0 & R_2 + S_2 & -S_2 & 0 & 0 & -R_2 & 0 & 0 & 0 \\ 0 & 0 & 0 & 0 & 1 & -1 & 0 & 0 & 0 \end{bmatrix}$$

$$\cdot \begin{bmatrix} \dot{\omega}_e \\ \dot{\omega}_F \\ \dot{\omega}_R \\ \dot{\omega}_{mg1} \\ \dot{\omega}_{r1} \\ \dot{\omega}_{r2} \\ F_1 \\ F_2 \\ T_{cl1} \end{bmatrix} = \begin{bmatrix} T_e \\ -T_F \\ -T_R + T_{mg2} \\ T_{mg1} \\ 0 \\ 0 \\ 0 \\ 0 \\ 0 \end{bmatrix} \tag{2.27}$$

In this power-split mode (with its dynamics shown in Eq. (2.27)), 14 variables are to be determined using the 9 equations above and given the component inertias and PG ratios R_1:S_1 and R_2:S_2. Given a drive cycle to follow, ω_R and ω_F are determined; T_F and T_R are also obtained when the front to rear torque ratio α is defined. The only free variable that can be controlled is either the engine speed or engine torque.

The square matrix of the integrated dynamics given in Eq. (2.27) can be decomposed into four sub-matrices as shown in Figure 2.8. The inertias of components and gears are assembled along the diagonal of the inertia matrix. The D-matrix indicates component connection, which is the key element that changes when the powertrain configuration changes.

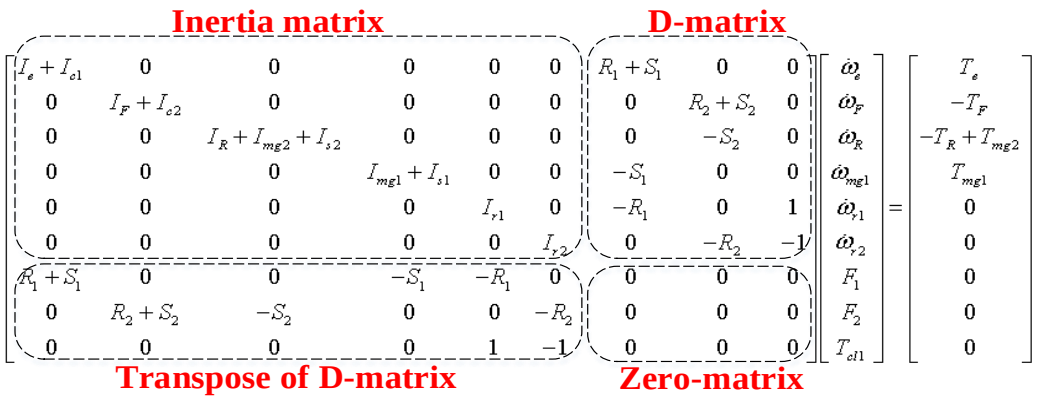

Figure 2.8 Patterns of proposed matrix representation

With the complete dynamics and generalized patterns, an automated modeling is possible. The automated modeling process (described in the next section) mainly involves generating the D-matrix given the component connections and clutch states. It consists of two steps: 1) initialize the configuration matrix of a design that shows the collocation of powertrain components excluding clutches, and 2) use clutch states to determine the dynamics.

2.2 Automated Modeling Process I: Initialization of Configuration Matrix

An 8x8 zero matrix, which is decomposed into four parts, is first created: $\begin{bmatrix} J & D_{ini} \\ D_{ini}^T & 0 \end{bmatrix}$, where J is a 6x6 matrix. The first four elements of the principal diagonal are replaced by the power source inertias in the order: engine, front output shaft, rear output shaft with MG2 and MG1.

The PG set gear inertias are added to the principal diagonal of sub-matrix J following their collocation indicated in the AWD patented design shown in Figure 2.1. For example, the engine is connected to the carrier of the first PG; thus the first element in the principal becomes I_e+I_{c1}. The last two diagonal entries of sub-matrix J are filled with the remaining gear inertias.

The entries to the upper-right 6x2 sub-matrix D_{ini} are determined by the connections to the PG set; the number of columns is equal to the number of PGs. When a powertrain component is connected to a PG node, the "node coefficient" will be $-S_{(\cdot)}$ if it is connected to the sun gear; $-R_{(\cdot)}$ if it is connected to the ring gear; $S_{(\cdot)}+R_{(\cdot)}$ if it is connected to the

carrier. By defining the component torque T_{ini} and acceleration vectors $\dot{\Omega}_{ini}$, the following matrices are obtained:

$$J = \begin{bmatrix} I_e + I_{c1} & 0 & 0 & 0 & 0 & 0 \\ 0 & I_F + I_{c2} & 0 & 0 & 0 & 0 \\ 0 & 0 & I_R + I_{mg2} + I_{s2} & 0 & 0 & 0 \\ 0 & 0 & 0 & I_{mg1} + I_{s1} & 0 & 0 \\ 0 & 0 & 0 & 0 & I_{r1} & 0 \\ 0 & 0 & 0 & 0 & 0 & I_{r2} \end{bmatrix}$$

$$D_{ini} = \begin{bmatrix} R_1 + S_1 & 0 \\ 0 & R_2 + S_2 \\ 0 & -S_2 \\ -S_1 & 0 \\ -R_1 & 0 \\ 0 & -R_2 \end{bmatrix} \tag{2.28}$$

$$T_{ini} = \begin{bmatrix} T_e & (-T_F) & (-T_R) + T_{mg2} & T_{mg1} & 0 & 0 & 0 & 0 \end{bmatrix}^T$$

$$\dot{\Omega}_{ini} = \begin{bmatrix} \dot{\omega}_e & \dot{\omega}_F & \dot{\omega}_R & \dot{\omega}_{mg1} & \dot{\omega}_{r1} & \dot{\omega}_{r2} & F_1 & F_2 \end{bmatrix}^T$$

2.3 Automated Modeling Process II: Use of Clutch States to Obtain the Dynamic Equations

Following a similar process described in [46], whenever a clutch connection exists, the sub-matrix D_{ini} will be augmented with a zero column and is defined as matrix D. When a clutch connects two PG nodes, the corresponding two entries of the augmented column is replaced with 1 and -1; the same procedure applies to D_{ini}^T. It should be mentioned that the augmented elements 1 and -1 indicate that the two nodes share the same rotational speed and acceleration. In the example, they indicate the coefficients of the relationship $(1) \cdot \dot{\omega}_{r1} + (-1) \cdot \dot{\omega}_{r2} = 0$.

Note that $\dot{\Omega}_{ini}$ is augmented with element $T_{cl(\cdot)}$, which indicates the internal torque of the added clutch and defined as $\dot{\Omega}$. T_{ini} is augmented with a zero and is denoted as T. By defining the obtained 8x8 matrix as the A matrix, the complete dynamics of the design indicated in the referred Toyota patent (Figure 2.1) is given by Eq. (2.29), and the augmented sub-matrix D is given by Eq. (2.30). It can be observed that Eq. (2.29) is the

matrix representation of the dynamics in Eqs. (2.21) and (2.22). The filled entries, such as $-S_{(\cdot)}$, $-R_{(\cdot)}$, 1and -1, determine the internal forces/torques acting on the corresponding nodes.

$$A=\begin{bmatrix} I_e+I_{c1} & 0 & 0 & 0 & 0 & 0 & R_1+S_1 & 0 & 0 \\ 0 & I_F+I_{c2} & 0 & 0 & 0 & 0 & 0 & R_2+S_2 & 0 \\ 0 & 0 & I_R+I_{mg2}+I_{s2} & 0 & 0 & 0 & 0 & -S_2 & 0 \\ 0 & 0 & 0 & I_{mg1}+I_{s1} & 0 & 0 & -S_1 & 0 & 0 \\ 0 & 0 & 0 & 0 & I_{r1} & 0 & -R_1 & 0 & 1 \\ 0 & 0 & 0 & 0 & 0 & I_{r2} & 0 & -R_2 & -1 \\ R_1+S_1 & 0 & 0 & -S_1 & -R_1 & 0 & 0 & 0 & 0 \\ 0 & R_2+S_2 & -S_2 & 0 & 0 & -R_2 & 0 & 0 & 0 \\ 0 & 0 & 0 & 0 & 1 & -1 & 0 & 0 & 0 \end{bmatrix} \tag{2.29}$$

$$T=\begin{bmatrix} T_e & (-T_F) & (-T_R)+T_{mg2} & T_{mg1} & 0 & 0 & 0 & 0 & 0 \end{bmatrix}^T$$

$$\dot{\Omega}=\begin{bmatrix} \dot{\omega}_e & \dot{\omega}_F & \dot{\omega}_R & \dot{\omega}_{mg1} & \dot{\omega}_{r1} & \dot{\omega}_{r2} & F_1 & F_2 & T_{cl1} \end{bmatrix}^T$$

$$D=\begin{bmatrix} R_1+S_1 & 0 & 0 \\ 0 & R_2+S_2 & 0 \\ 0 & -S_2 & 0 \\ -S_1 & 0 & 0 \\ -R_1 & 0 & 1 \\ 0 & -R_2 & -1 \end{bmatrix} \tag{2.30}$$

Grounding clutch connections can be added in a similar manner by putting 1 in the corresponding node entry. The augmented element 1 indicates that the connected node has a zero rotational speed and acceleration. For example, if the ring gear node of the 1st PG is grounded, the coefficients of the relationship are indicated as $(1)\cdot\dot{\omega}_{r1}=0$.

For all the power-split designs that use two PG sets, two output shafts, and three clutches, if the MG2 is collocated with the rear output shaft, the total number of designs is $0.5\cdot P_6^4\cdot C_{15}^3 = 180\cdot 455 = 81900$. When considering that the PG gear ratio varies from 2:1 to 4:1, and the final drive ratio varies between 2:1 to 6:1 (both with step size 1), the total number of design candidates is 18,427,500.

CHAPTER 3
Systematic Design Methodology for AWD Multi-Mode Power-Split Hybrid Vehicles

With the modeling technique for both AWD and 2WD multi-mode power-split hybrid powertrains described in Chapter 2, all possible designs are generated. A systematic design methodology developed in this chapter is for screening all these possibilities according to the desired criteria and achieving good designs.

Before introducing the detailed procedure of the design methodology, the criteria for desired designs should be clearly defined first. In this dissertation, such criteria include but not limited to powertrain attributes and performance requirements. The attributes highlighted in this dissertation are assumed to be necessary in the target AWD hybrid pickup truck design:

- *All-wheel-drive (AWD)*: the engine can drive both output shafts forward.
- *All-wheel-regenerative braking (AWRB)*: both output shafts can be controlled by the two electric motors during braking.
- *Driving backward using engine power*: the engine can drive the vehicle backwards (when the output shaft speeds are negative).

The AWD attribute ensures a truck design's towing and grade performance; the AWRB attribute assures better regenerative braking; the capability of driving backward using the engine power attribute ensures the truck design's performance when backing up a towed load on a slope even when the battery SOC is low.

Performance requirements, such as vehicle top speed and maximum acceleration, are also considered. The vehicle's top speed must at least be 90 mph, and the average acceleration from speeds of 0 to 60 mph must be higher than 3.6 m/s^2. These two requirements ensure that the obtained designs are competitive against the benchmark (the conventional, non-hybrid vehicle).

With the foregoing criteria definition, the methodology to obtain good designs is described in the remaining of this chapter.

3.1 Four-Step Systematic Design Process

The design problem for optimal configurations, sizing, and control can involve a considerably large number of design candidates. A brute-force search is neither warranted nor efficient. Our proposed design process starts by screening out infeasible or incapable designs; consequently, the number of design candidates that require heavy computations is significantly reduced.

This four-step design process is outlined in Figure 3.1.

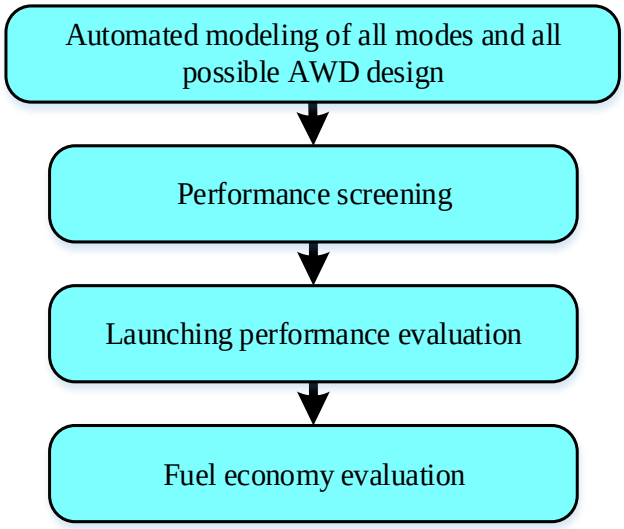

Figure 3.1 Four-step systematic design process

Step 1 – Automated modeling is a proposed procedure to model all modes of all potential AWD designs; the search space is limited to designs that use three clutches.

Step 2 – Performance screening involves screening for two aspects: attributes and criteria. Performance attributes are characteristics required by the designer that can include but not limited to AWD, all-wheel-regenerative-braking, and driving backward using the engine power. Performance criteria can include average acceleration and towing capability on a slope. Criteria can be based on standards, such as the SAE Standard J2807 for light trucks. This screening step is critical to weed out inferior designs so that only feasible designs are passed to succeeding steps.

Step 3 – Launching performance evaluation obtains the best launching performance of each design candidate at speeds of 0-60 mph by solving an optimization problem.

Step 4 – Fuel consumption evaluation involves fuel economy assessment using the PEARS method [35]. This evaluation step is applied to all feasible designs with an acceptable launching performance.

The terms frequently used in this dissertation are summarized in Table 3.1.

Table 3.1 Frequently Used Terms in Systematic Design Process

Terms	Definition
Node	An available collocation point of a PG set (i.e., sun, carrier, and ring gears)
Configuration	A given topology of how components (i.e., engine, motors, and output shafts) are connected to nodes
Design	A configuration plus a selected set of clutches
Design Candidate	A design with given component sizing (e.g., gear ratios for the PG set and final drive ratio)
Mode	Clutch state (i.e., open and close)

3.2 Performance Attribute Screening

Given the complete HEV dynamic in Eq. (2.29), the augmented element $\dot{\omega}$ (with rotational speed and internal force) is expressed in Eq. (3.1) by inverseing the dynamic equation, where $A_{inv(i,j)}$ refers to the element in the i^{th} row and j^{th} column of the inverse matrix A^{-1}.

$$\dot{\Omega} = A^{-1} \cdot T$$

$$A^{-1} = \begin{bmatrix} A_{inv(1,1)} & A_{inv(1,2)} & A_{inv(1,3)} & A_{inv(1,4)} & A_{inv(1,5)} & \cdots & \cdots \\ A_{inv(2,1)} & \cdots & \cdots & & & & \cdots \\ A_{inv(3,1)} & \cdots & & & & & \\ A_{inv(4,1)} & & & & & & \\ A_{inv(5,1)} & & & & & & \\ A_{inv(6,1)} & & & & & & \\ \cdots & & & & & & \\ & & & & & & \\ \cdots & \cdots & & & & & \cdots \end{bmatrix} \tag{3.1}$$

$$T = \begin{bmatrix} T_e & (-T_F) & (-T_R) + T_m & T_g & 0 & 0 & 0 & 0 & 0 \end{bmatrix}^T$$

$$\dot{\Omega} = \begin{bmatrix} \dot{\omega}_e & \dot{\omega}_F & \dot{\omega}_R & \dot{\omega}_g & \dot{\omega}_{r1} & \dot{\omega}_{r2} & F_1 & F_2 & T_{cl1} \end{bmatrix}$$

The elements $A_{inv(i,j)}$ in matrix A^{-1} are used for attribute screening according to the rules listed in Table 3.2.

Table 3.2 Performance Attribute Screening Rules

Desired Attributes	Screening Condition
AWD	$A_{inv(2,1)} > 0, A_{inv(3,1)} > 0$
AWRB	$A_{inv(2,4)} \neq 0, A_{inv(2,1)} = 0, A_{inv(3,1)} = 0$
Driving backward using engine power	$A_{inv(2,1)} < 0, A_{inv(3,1)} < 0$

Note that $A_{inv(2,1)}$ and $A_{inv(3,1)}$ relate the engine torque to the front and rear output shaft, respectively. $A_{inv(2,4)}$ relates the MG1 torque with the front output shaft.

3.3 Efficient Performance Criterion Screening

To implement a computationally efficient performance screening, a torque relationship derived from the static balanced state is used. The torque relationships and speed relationships of all six PG nodes are obtained from dynamics $A\dot{\omega} = T$ through sub-matrix D. Using the Toyota patent [44] shown in Figure 2.1 as an example again, the two

relationships are obtained in Eq. (3.2) by neglecting the gear inertias. Note that after neglecting the gear inertias, the last two elements of the torque vector in Eq. (3.2) are zeros.

$$D\begin{bmatrix} F_1 \\ F_2 \\ T_{cl1} \end{bmatrix} = \begin{bmatrix} T_e \\ (-T_F) \\ (-T_R)+T_{mg2} \\ T_{mg1} \\ 0 \\ 0 \end{bmatrix}, \quad D^T \begin{bmatrix} \dot{\omega}_e \\ \dot{\omega}_F \\ \dot{\omega}_R \\ \dot{\omega}_{mg1} \\ \dot{\omega}_{r1} \\ \dot{\omega}_{r2} \end{bmatrix} = \begin{bmatrix} 0 \\ 0 \\ 0 \end{bmatrix} \tag{3.2}$$

Considering the torque relationship in Eq. (3.2) and neglecting all inertias except that of the vehicle (I_v), the best average acceleration rate of each design can be calculated by Eqs. (3.3) – (3.4) and used to estimate the launching performance. To complete the calculation for the best possible acceleration, the vehicle speed grid *n* and targeted speed 60 mph are used. The maximum acceleration at the i^{th} grid point is calculated in Eq. (3.3) based on the maximum combined output torque from Eq. (3.2). In the former equation, R_{tire} is the tire radius, and *FR* is the final drive gear ratio; T_{Fmax}, T_{Rmax}, and T_{vmax} refer to the maximum output torques at the front wheels, rear wheels, and vehicle, respectively; μ_{tire} is the tire road friction coefficient and is fixed at 0.8 in this study. To obtain T_{Fmax} and T_{Rmax}, all the combinations of T_e, T_{MG1}, and T_{MG2} are used to calculate T_F and T_R through Eq. (3.2); T_{Fmax}, T_{Rmax}, and T_{vmax} are the maximum values obtained. Details in calculating the acceleration are found in the Appendix A.

$$\begin{aligned} a_i &= \frac{T_{v\max}}{I_v} \cdot \frac{R_{tire}}{FR} \\ T_{v\max} &= T_{F\max} + T_{R\max} \\ T_{F\max} &\le N_{z_f} \cdot \mu_{tire} \\ T_{R\max} &\le N_{z_r} \cdot \mu_{tire} \end{aligned} \tag{3.3}$$

$$\bar{a} = \frac{n}{\sum_1^n \frac{1}{a_i}} \tag{3.4}$$

The launching acceleration in SAE Standard J2807 [7, 47] or the acceleration rate of the benchmark (non-hybrid) vehicle can be used as the threshold for acceptable

acceleration. These design requirements not only screen for competent designs but also substantially reduce the size of the feasible design pool for a more efficient design search.

After the first two steps, feasible designs are identified. The remaining two steps of the design methodology are to examine the acceleration performance and fuel economy of those feasible designs. Optimal or near-optimal control results must be used to ensure fair comparison at these two stages of evaluation. For evaluating launching performance, dynamic programming (DP) is used to obtain the optimal result. For evaluating fuel economy, although DP guarantees global optimality, it is sometimes impractical to use because of its high computational cost. In a large scale design search, it may take months or even years to finish the exhaustive search [35]. The PEARS method reported in [35] employs a near-optimal energy management that is ten thousand times faster than the DP. We choose to use the PEARS method for fuel economy evaluation in this study.

3.4 Acceleration Performance Evaluation

In the following case study, the performance of the conventional (non-hybrid) F-150 vehicle is used as the benchmark that sets the design requirement. The following performance attributes are used for the case study: AWD, AWRB, and AWD backward using engine power. Given the above requirements, size designs with 328 different gear sizing (i.e., PG gear ratio and final drive ratio) combinations survive the screening.

In the third step of the design methodology, acceleration performance for all surviving design candidates is evaluated. Different from the performance criterion screening in the second step, which primarily estimates an approximate average acceleration for the consideration of reducing computational cost, the performance evaluation in this section simulates the acceleration time with more detailed dynamics captured. The objective of this evaluation step is to find the control inputs that accelerate the vehicle to reach the targeted speed. The control problem is then an optimization problem at each time step as shown in Eq. (3.5).

$$
\begin{aligned}
&\max \quad a(k) \\
&s.t. \qquad v(k) = \sum_{i=1}^{k} a_{\max}(i) \cdot \Delta t + v_0 \\
&\qquad\qquad t(k) = k \cdot \Delta t \\
&\qquad\qquad v_0 = 0 \\
&\qquad\qquad v(k) \le v_{target} \\
&\qquad\qquad \forall k \in 1,2,...,N
\end{aligned}
\tag{3.5}
$$

The target speed v_{target} is 60 mph. The step size is $\Delta t = 0.1\ s$. $v(k)$ is the vehicle speed at time step k, and $a(k)$ is calculated from Eq. (*3.6*).

$$
a(k) = \dot{\omega}_r r = \dot{\omega}_f r \tag{3.6}
$$

The optimization problem is solved through brute force search, by examining all the combinations of T_e, T_{MG1}, and T_{MG2} to obtain the maximum acceleration. This free-terminal-time optimization continues until the vehicle speed reaches 60 mph. The battery SOC constraint is not considered, because the 0 – 60 mph launching action only lasts briefly.

3.5 Fuel Economy Evaluations Using Power-Weighted Efficiency Analysis for Rapid Sizing Method

To evaluate the optimal performance of fuel consumption of each design, it is formulated as a minimization problem as follows:

$$
\begin{aligned}
&\min \qquad J = \sum_{k=0}^{N-1} \dot{m}_f(k) \\
&s.t. \qquad \dot{\Omega} = A^{-1} \cdot T \\
&\qquad\qquad S\dot{O}C = f_{bat}(P_{bat}) \\
&\qquad\qquad \dot{m}_f = f_e(\omega_e, T_e) \\
&\\
&\underline{x} \le x_k \le \overline{x}, \forall k \\
&\underline{u} \le u_k \le \overline{u}, \forall k
\end{aligned}
\tag{3.7}
$$

where $\dot{m}_f$ is the engine fuel rate; $\dot{\omega} = A^{-1} T$ is the inverse complete dynamics of Eq. (2.29); $S\dot{O}C$ represents the battery dynamics.

The PEARS method is a near-optimal energy management methodology which was originally designed for component sizing [35]. It first analyzes the target cycle by discretizing the drive cycle in two dimensions: vehicle speed and vehicle torque demand. Thereafter, it uses the discretized information to calculate the optimal control input for all operating modes based on the defined power-weighted efficiency. Finally, the DP is incorporated to determine mode selection over the horizon. The PEARS process the with DP method is outlined in Figure 3.2.

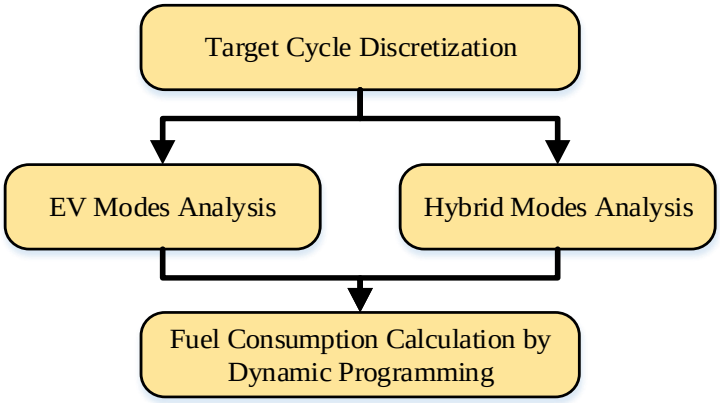

Figure 3.2 PEARS method [35]

For EV (electric vehicle) modes, the electric motor powers P_{MG1} and P_{MG2} are obtained given a combination of the rear-to-front torque ratio α as well as their corresponding torques. Subsequently, the electrical system loss in P^{loss}_{EV} and battery power P^{in}_{EV} can be calculated. Thereafter, the best possible efficiency for an EV mode is obtained from Eqs. (3.8) and (3.9).

$$\eta_{EV} = 1 - \frac{P_{EV}^{loss}}{P_{EV}^{in}} \tag{3.8}$$

$$\eta_{EV}^{*}|_{v,a} = \max\left[\eta_{EV}\left(\alpha, T_{MG1}, T_{MG2}\right)\right]|_{v,a} \tag{3.9}$$

For hybrid modes, four power flows P_{e_1}, P_{e_2}, P_{e_3}, and P_{batt} are defined and summarized in Table 3.3. Similar to the EV mode analysis, by examining all the

combinations of rear-to-front torque ratio, speed and torque, the highest power-weighted efficiency is defined and calculated using Eqs. (3.10) and (3.11).

Table 3.3 Power-Flow of Hybrid System

Power Flow	Description
P_{e_1}	Engine power through generator
P_{e_2}	Engine power through generator to motor
P_{e_3}	Engine power that directly flows to final drive
P_{batt}	Battery power that drives the motor

$$\eta_{Hybrid}\left(\alpha,\omega_e,T_e\right)=\frac{P_{e\_1}\eta_G\eta_{batt}/\left(\eta_{e\_\max}\eta_{G\_\max}\right)}{P_{fuel}+\mu P_{batt}} + \frac{P_{e\_2}\eta_G\eta_M/\left(\eta_{e\_\max}\eta_{G\_\max}\eta_{\mathrm{M}\_\max}\right)}{P_{fuel}+\mu P_{batt}} + \frac{P_{e\_3}/\eta_{e\_\max}+\mu P_{batt}\eta_{batt}\eta_M/\eta_{\mathrm{M}\_\max}}{P_{fuel}+\mu P_{batt}} \tag{3.10}$$

$$\eta_{Hybrid}{}^{*}\big|_{v,a}=\max\left[\eta_{Hybrid}\left(\alpha,\omega_e,T_e\right)\right]\big|_{v,a} \tag{3.11}$$

In Eq. (3.10) and (3.11), η_G, η_M, and η_{batt} refer to the efficiency of generator, motor, and battery, respectively. P_{fuel} refers to engine power, and μ is a flag to indicate whether the battery assist is on or not. The power-weighted efficiency η_{Hybrid} relates the fuel and battery cost for the multi-object optimization. More details of PEARS can be found in [35].

3.6 AWD Design Case Study of Hybrid F-150

In the following, a conceptual parallel-hybrid Ford F-150 light truck is chosen for the case study. The comparisons made are among the conventional F-150, a pre-transmission parallel hybrid F-150 (Figure 3.3), and AWD hybrid F-150. The key parameters of the vehicle are listed in Table 3.4. The powertrain design pool of components includes three power sizes for the engine (163, 217, and 272 kW) and three power sizes for the two electric motors (66, 88, and 110 kW). It should be mentioned that the two motors can have different sizes. In this case study, an electric motor is assumed to be collocated with the rear output shaft; however, the proposed design methodology can be easily applied to other scenarios.

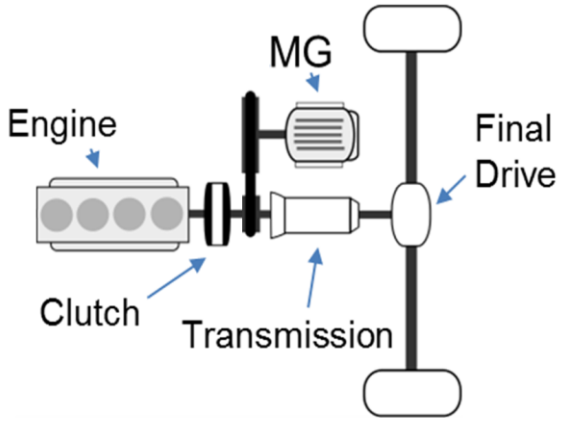

Figure 3.3 Schematic of pre-transmission parallel hybrid design benchmark

Table 3.4 Parameters of Vehicle Used in Case Study (F-150)

Component / Vehicle	Parameters: Conventional	Parallel	AWD Hybrid
Engine	272 kw at 5200rpm 569 Nm at 2500rpm	272 kw at 5200rpm 569 Nm at 2500rpm	163 – 272 kw at 5200rpm
MG1 power	N/A	90 kW	66 – 110 kW
MG2 power	N/A	N/A	66 – 110 kW
Transmission	6-speed	6-speed	2-PG set
Drivetrain	RWD	RWD	AWD

The combined launching performance and fuel economy results of the winning design candidates are shown in Figure 3.4. There is a family of designs that achieve better accelerations and better fuel economy than the conventional and parallel hybrid vehicles. Two designs (Design *A* and Design *B*) are highlighted in Figure 3.5 and Figure 3.6, respectively. Both families have a large number of design candidates (i.e., designs with different component size combinations) that achieve excellent launching and fuel economy performance. More details of mechanical connections and operations for these designs can be found in U.S. Patent Application No. 15/763,722 [48].

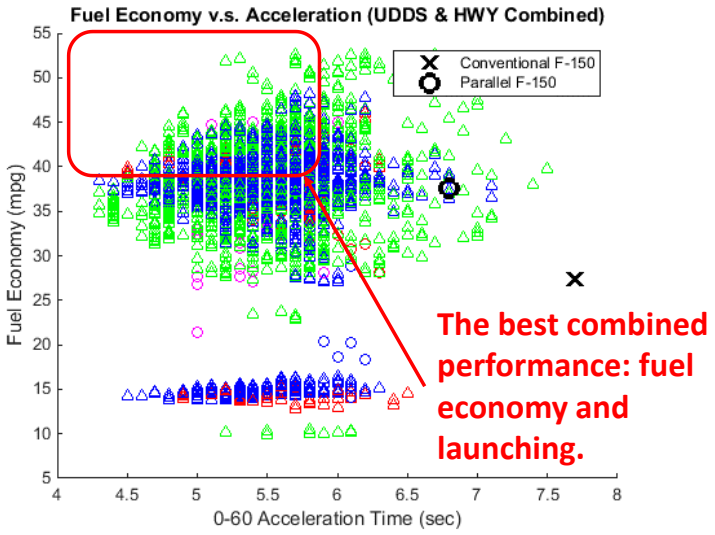

Figure 3.4 Combined performance and fuel economy results of various hybrid design candidates

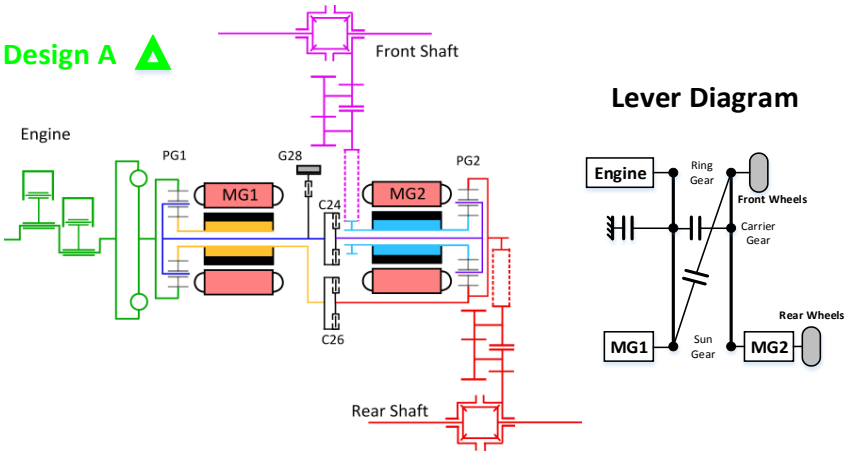

Figure 3.5 Diagram of Design *A*

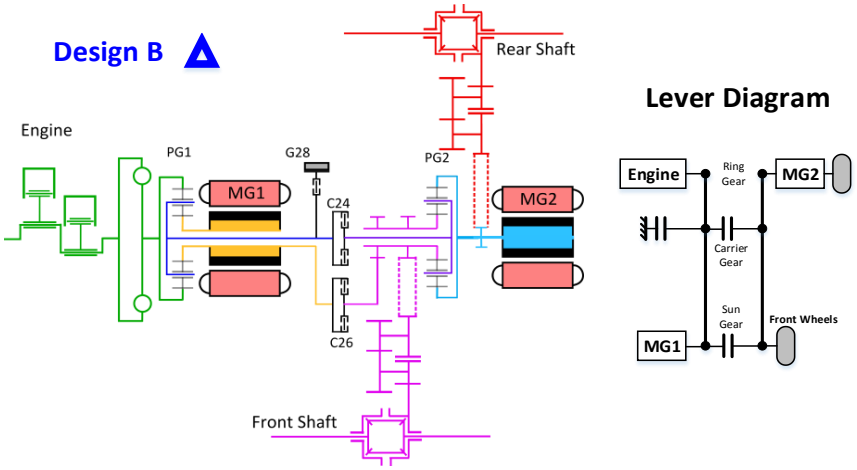

Figure 3.6 Diagram of Design *B*

An optimal design candidate from Design *A* is selected for further analysis; its powertrain component sizes are listed in Table 3.5. This highlighted design has the same total system power as the benchmark parallel hybrid design. Its performance is compared to the conventional and parallel designs listed in Table 3.6. Selected results are shown in Figure 3.7 and Figure 3.8.

Table 3.5 Powertrain Parameters of Design *A*

Engine	MG1	MG2	R/S Ratio (PG1)	R/S Ratio (PG2)	Final Drive (Front)	Final Drive (Rear)
163 kW	110 kW	88 kW	2:1	4:1	5:1	6:1

Table 3.6 Performance Summary

Vehicle	Launching Time (s) (16000 lbs.)	Launching Time (s) (5073 lbs.)	Fuel Economy – UDDS (mpg) (5073 lbs.)	Fuel Economy – HWFET (mpg) (5073 lbs.)
Conventional	21.6	7.7	25.0	30.3
Parallel	17.3	7.1	42.3	31.7
AWD Winning Design *A*	13.5	5.1	50.0	34.8

Figure 3.7 illustrates how the highlighted winning design accelerates from 0 to 60 mph. The power-split mode is used to achieve the best launching in 5.1s because the operating mode can produce maximum power with all propulsion components engaged; the power-split mode controls the engine speed for maximum engine torque at any vehicle speeds.

Compared to the parallel hybrid F-150 design, the winning Design *A* exhibits launching that is 28% faster, and fuel economies that are 18.2% and 9.8% better in the UDDS and HWFET cycles, respectively. These indicate that the proposed systematic design methodology successfully identifies a family of good AWD designs.

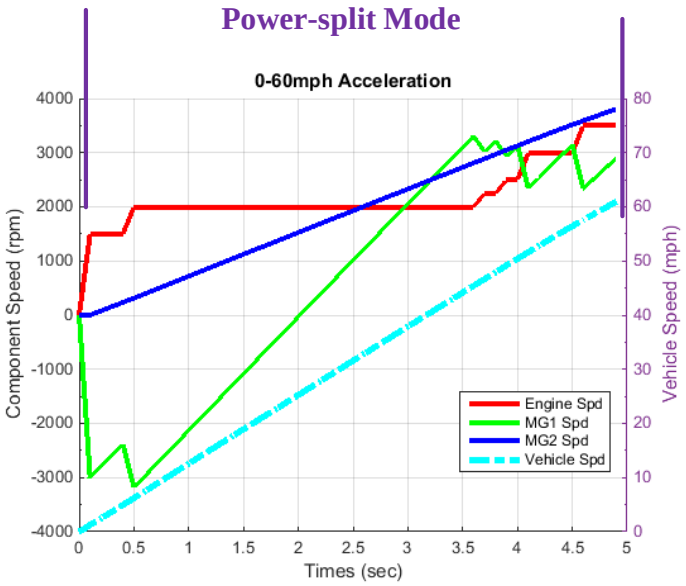

Figure 3.7 Results of 0-to-60 launching performance

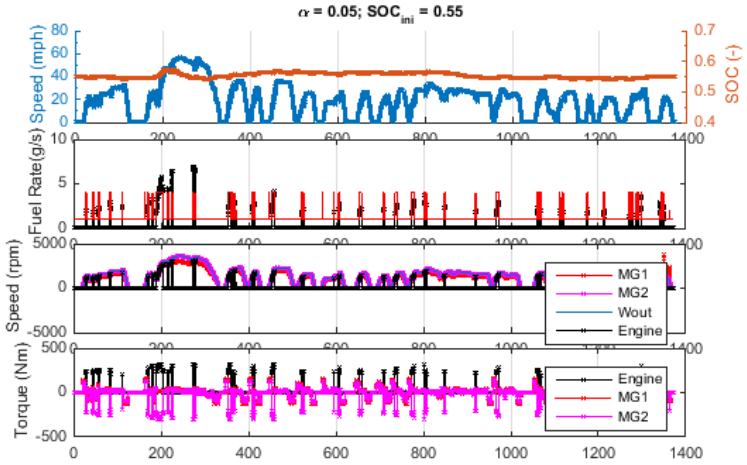

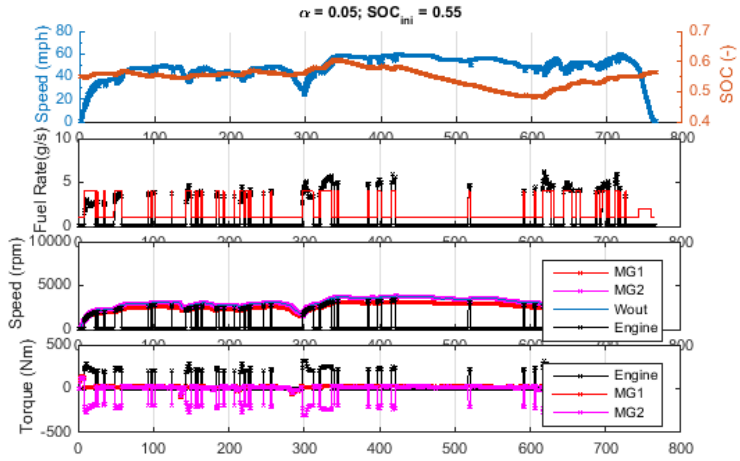

Figure 3.8 Simulation results of UDDS and HWFET drive cycles

3.7 Analysis of Highlighted AWD Hybrid Power-Split Vehicle Designs

3.7.1 Common Features of the Two Winning Designs

It is observed that the two highlighted designs (Design *A* and Design *B*) share several common features; each design has a clutch that connects the carrier nodes of the two PG sets; and the two output shafts are on the same PG set that connects to the sun gear node and the ring gear node. These common features allow a good torque balance of the second PG set.

The torque balance analysis in Figure 3.9 shows that in equilibrium state torques at the ring gear and sun gear are in the same direction while the torque at the carrier is in the opposite direction. Therefore, the two output shafts of AWD designs will be collocated to either the ring gear or sun gear, respectively.

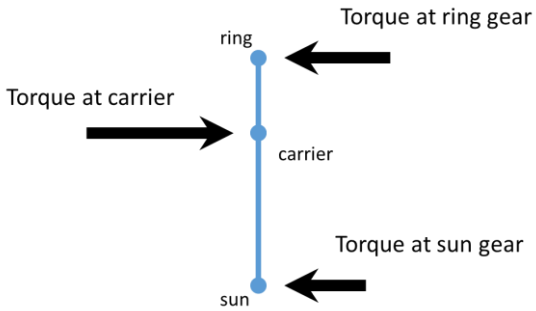

Figure 3.9 Torque balance analysis of a PG set using the lever diagram

By understanding the torque balance analysis, quick examination for rationality of AWD power-split designs becomes possible.

3.7.2 Fuel-Saving Control Policy from Optimization Results

From the results in the two drive cycles, it was observed that the EV mode and parallel mode are frequently used: the parallel mode is used in high power driving and the EV mode is used for low-power driving and braking. To better understand this observation, the mode distribution is shown in Figure 3.10. The two operating modes are shown in Figure 3.11.

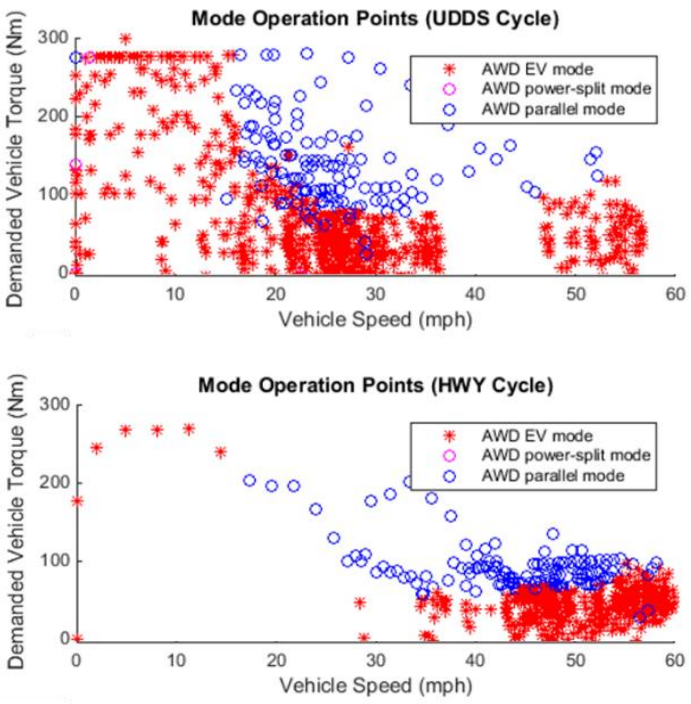

Figure 3.10 Operation mode analysis of UDDS and HWFET cycles

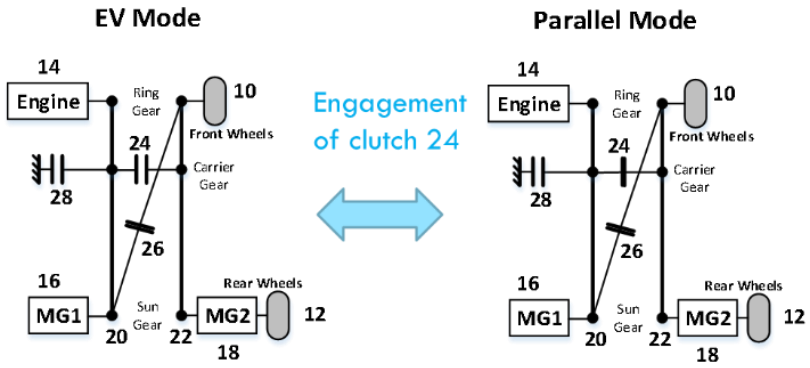

Figure 3.11 Lever diagram of EV mode and parallel mode

Based on the observation of 0-60 launching (when power-split mode is used) and the fuel-efficient driving in the EPA cycles, a mode selection policy is generated and shown in Figure 3.12. Although this mode selection map is simple and may lose certain optimality, it summarizes from optimal control results and is implementable.

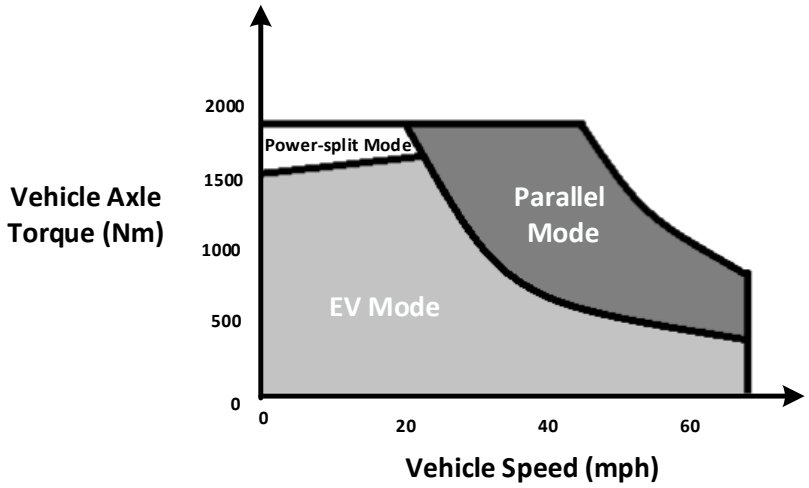

Figure 3.12 Policy for mode selection

3.7.3 Comparison of Launching Performance and Gradeability of AWD and FWD Hybrid Vehicles and RWD Hybrid Vehicles

To better understand the performance of the highlighted AWD hybrid design, the analyses of acceleration and grade performance are presented in this subsection. Two tests are designed based on the towing-vehicle propulsion requirements from SAE Standard J2807. The AWD hybrid Design *A*, a FWD parallel design and a RWD parallel design are compared at the same gross combination weight rating (GCWR) of 16000 lbs. The vehicle dynamics of the AWD design are shown in the Appendix A.

Test 1 – Launch on 12% grade: time for launching the towing vehicle from 0 to 10 mph on a 12% grade.

Test 2 – Gradeability test: maximum grade on a slope while maintaining the vehicle speed at 40 mph.

In the summarized results in Table 3.7, it can note that the AWD power-split hybrid design is able to accelerate from 0 to 10 mph in 5.3 seconds, whereas the RWD parallel design requires 7.3 seconds to launch; the FWD parallel design cannot even launch from the 12% grade slope. The AWD design can launch on a slope that is 55% steeper than the RWD parallel design can. The RWD design performs better than the FWD design does because of the vehicle load transfer. Overall, the AWD power-split hybrid design presents the best performance.

Figure 3.13 demonstrates the gradeability of these three designs by showing the tow-weight capability on different slopes. The AWD hybrid design can tow heavier weights because it uses both axles. The FWD design tows less than the RWD design can because of load transfer; it is unable to drive the vehicle up a slope with an 11% grade or higher at a fully loaded weight.

Table 3.7 Launch Performance on 12% Grade and Gradeability

Vehicle (GCWR: 16000 lbs.)	Launch on 12% Grade	Gradeability (at 40 mph)
FWD Parallel	Infeasible	9.2 %
RWD Parallel	7.3 s	13.2 %
AWD Winning Design *A*	5.3 s	20.5 %

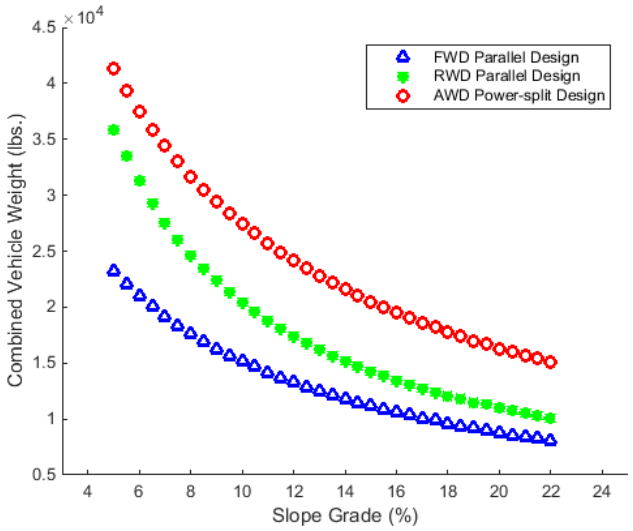

Figure 3.13 Gradeability performance (at 40 mph) of the three designs

CHAPTER 4
Relaxed Optimization for Vehicle Control

Subsequent to the modeling and design processes in Chapter 2 and Chapter 3, respectively, a group of good HEV designs are identified. Given an identified design, the control strategy development then becomes the next important stage. To properly design a control strategy and compare its fuel efficiency performance, the global optimal results that are solved offline are usually generated for the following:

1. Benchmark comparison for justifying "good" performance of the control strategy
2. Analysis of results with the optimal control for control strategy development

The offline evaluation of fuel economy is commonly performed by following certain drive cycles, such as UDDS and HWFET, precisely. However, in the real-world a vehicle never follows defined drive cycles exactly, and can "wander" around the desired speed profile instead, within the EPA defined speed tolerance (±2 mph) [21]. In this dissertation, the relaxed optimization is introduced to explore this concept.

In this chapter, the relaxed optimization is defined, formulated, and solved given an HEV design. The resulting optimal controls are analyzed, and the knowledge acquired over different powertrain platforms is summarized. These will be useful for the control strategy development that is presented in the later part of this dissertation. With this established study framework, the analysis of system optimal control for the AWD power-split HEV becomes possible.

4.1 Constraint Relaxation

In this dissertation, the relaxed optimization for vehicle control is defined under the condition that the dynamic constraints of powertrain and vehicle are relaxed. In particular,

the relaxed constraints that are investigated include: vehicle speed, range to the leading vehicle, and battery SOC. The relaxation of vehicle speed constraint allows the control strategy to vary the vehicle speed in the proximity of the desired speed profile; relaxing the vehicle range constraint represents the controlled vehicle being limited by the leading and tailing vehicle in the real-world scenario; relaxing the battery SOC allows the control strategy to optimize the distribution between the mechanical and electrical power paths. The battery SOC, as an additional energy storage, along with the vehicle kinetic energy storage (vehicle speed and range to the leading vehicle) can be used a strike a better balance between fuel consumption and vehicle ride. The studies and comparison of these constraint relaxations over the conventional vehicle and HEV are performed.

4.1.1 Conventional Vehicles – No Relaxations

For conventional vehicles with a step-gear automatic transmission, gear position is the only control available to optimize the vehicle's fuel consumption according to defined drive cycles. At a desired vehicle speed and engine power, the engine torque and engine speed are dependent on the gear position. A general problem formulation is shown in Eq. (4.1), where $\dot{m}_f$ refers to the engine fuel rate, ω_e is the engine speed, T_e is the engine torque, and f_e is the function that relates $\dot{m}_f$, T_e, and ω_e; T_{v_k} and v_k represent the vehicle torque and speed at time step k, respectively; R_{tire} is the tire radius; J is the accumulated cost of fuel consumption.

$$\begin{aligned} \min \quad & J = \sum_{k=0}^{N-1} \dot{m}_f(k) \\ s.t. \quad & T_e = \frac{T_{v_k}}{n_{gear}} \\ & \omega_e = v_k \cdot \frac{1}{R_{tire}} \cdot n_{gear} \\ & \dot{m}_f = f_e(\omega_e, T_e) \end{aligned} \tag{4.1}$$

4.1.2 Constraint Relaxation for Conventional Vehicles

The vehicle speed in the relaxed control problem can follow the speed profile approximately instead of exactly. In this case, it is not necessary for the torque output from

the transmission to deliver exactly the demanded value at the given speed level; in other words, the vehicle speed and vehicle range constraints are relaxed. A general problem formulation is shown in Eq. (4.2), where v_k and s_k represent vehicle speed and range (or the distance between the controlled vehicle and leading vehicle), respectively; $\underline{v}_k$, $\overline{v}_k$, $\underline{s}_k$, and $\overline{s}_k$ are the lower and upper limits of each state, respectively.

$$\begin{aligned}
\min \quad & J = \sum_{k=0}^{N-1} \dot{m}_f(k) \\
s.t. \quad & \dot{\Omega} = A^{-1} \cdot T \\
& \omega_e = v_k \cdot \frac{1}{R_{tire}} \cdot n_{gear} \\
& \dot{m}_f = f_e(\omega_e, T_e) \\
& s_k = \sum_{i=1}^{k} v_k dt \\
& \underline{v}_k \le v_k \le \overline{v}_k, \forall k \\
& \underline{s}_k \le s_k \le \overline{s}_k, \forall k
\end{aligned} \tag{4.2}$$

4.1.3 Hybrid Electric Vehicle and Its Relaxation

Hybrid electric vehicles possess additional DOFs because power can be generated from the engine or battery. This additional flexibility results in a larger feasible control set, i.e., opportunity for better fuel economy. The battery SOC can be any value within its range (0.3-0.8); this condition allows the engine to change its torque and/or speed given a desired vehicle command. Therefore, it can be interpreted that the battery SOC is a relaxed constraint to the optimal power generation problem. A general problem formulation for the HEV is shown in Eq. (4.3), where P_{batt} is the battery power, f_{batt} represents the battery dynamics related to motor speed ω_m, motor torque T_m, and motor efficiency η_m; $\dot{SOC}$ represents the change rate of SOC, and SOC_{min} and SOC_{max} are the lower and upper limits, respectively.

$$
\begin{aligned}
\min \quad & J = \sum_{k=0}^{N-1} \dot{m}_f(k) \\
s.t. \quad & \dot{\Omega} = A^{-1} \cdot T \\
& \omega_e = v_k \cdot \frac{1}{R_{tire}} \cdot n_{gear} \\
& \dot{m}_f = f_e(\omega_e, T_e) \\
& s_k = \sum_{i=1}^{k} v_k dt \\
& \dot{SOC} = f_{bat}(P_{bat}) \\
& P_{bat} = \omega_m \cdot T_m \cdot \eta_m \\
& SOC_{\min} \le SOC \le SOC_{\max}
\end{aligned}
\tag{4.3}
$$

The vehicle speed control problem can be relaxed to add flexibility to the optimal search. By combining all relaxations including battery SOC constraints, vehicle speed constraints, and range constraints, the general relaxed optimization problem of the HEV is developed, as shown in Eq. (4.4).

$$
\begin{aligned}
\min \quad & J = \sum_{k=0}^{N-1} \dot{m}_f(k) \\
s.t. \quad & \dot{\Omega} = A^{-1} \cdot T \\
& \omega_e = v_k \cdot \frac{1}{R_{tire}} \cdot n_{gear} \\
& \dot{m}_f = f_e(\omega_e, T_e) \\
& s_k = \sum_{i=1}^{k} v_k dt \\
& \dot{SOC} = f_{bat}(P_{bat}) \\
& P_{bat} = \omega_m \cdot T_m \cdot \eta_m \\
& SOC_{\min} \le SOC \le SOC_{\max} \\
& \underline{v}_k \le v_k \le \overline{v}_k, \forall k \\
& \underline{s}_k \le s_k \le \overline{s}_k, \forall k
\end{aligned}
\tag{4.4}
$$

Details of the dynamics in the above equations are shown in the next section.

4.2 Formulation of the Relaxed Optimization Problem

To start the investigation of this topic, a conventional powertrain and a pre-transmission parallel hybrid powertrain are used for the case study as shown in Figure 4.1. The conventional powertrain consists of an internal combustion engine (ICE) and a 6-speed automatic transmission; the parallel hybrid powertrain has an additional electric motor before the transmission. There is a clutch between the engine and transmission that can disconnect the engine from the powertrain.

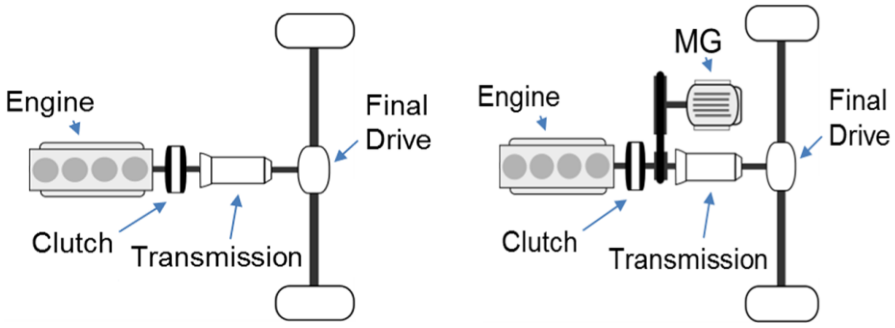

Figure 4.1 Schematic of conventional powertrain and pre-transmission parallel hybrid design

The fuel/electrical efficiencies of the powertrain components are shown in Figure 4.2. The fuel rate $\dot{m}_f$ is obtained from the BSFC map shown in Figure 4.2. The constraints of engine speed ω_e and torque T_e are indicated in the BSFC map by the black line and considered throughout the design process. Similarly, the efficiency of the electric machine is obtained from the motor map shown in Figure 4.2.

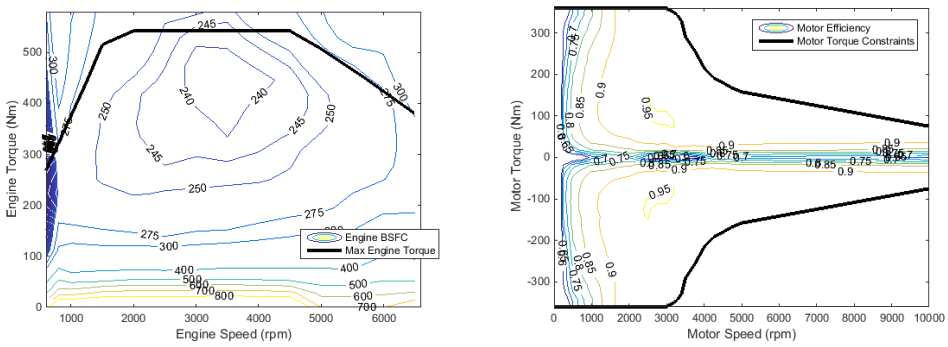

Figure 4.2 Engine BSFC map (left) and motor efficiency map (right)

The battery is modeled by a simple open-circuit voltage model with a constant internal resistance. The battery SOC is described in Eq. (4.5), where V_{oc} is the open-circuit voltage, and R_{batt} is the battery internal resistance.

$$S\dot{O}C = -\frac{V_{oc} - \sqrt{V_{oc}^{\ 2} - 4R_{bat}P_{batt}}}{2 \cdot R_{bat}} \tag{4.5}$$

The automatic transmission is modeled by gear ratios with a different efficiency for each gear. The relationships of speed and torque are given in Eq. (4.6), together with the vehicle dynamics shown in Eq. (4.7), where a_v represents the vehicle acceleration, m is the vehicle mass, g is the gravitational constant, μ is the rolling resistance coefficient, ρ is the air density, C_d is the drag coefficient, A is the vehicle cross sectional area, and R_{tire} is the tire radius.

$$\begin{aligned} \omega_e &= v_k \cdot n_{gear} \\ T_e &= \frac{T_{v_k}}{n_{gear}} \end{aligned} \tag{4.6}$$

$$T_v = \left(mg\mu + \frac{1}{2}\rho C_d A v^2 + ma_v \right) \cdot R_{tire} \tag{4.7}$$

Combining all the models in Eqs. (4.4) – (4.7), the optimal control problem with relaxed speed and range constraints for the conventional vehicle and the hybrid vehicle are formulated in Eqs. (4.8) and (4.9), respectively.

$$\begin{aligned} \min \quad & J = \sum_{k=0}^{N-1} \dot{m}_f(k) \\ s.t. \quad & T_e = \frac{T_{v_k}}{n_{gear}} \\ & \omega_e = v_k \cdot \frac{1}{R_{tire}} \cdot n_{gear} \\ & \dot{m}_f = f_e(\omega_e, T_e) \\ & s_k = \sum_{i=1}^{k} v_k dt \\ & T_v = \left(mg\mu + \frac{1}{2}\rho C_d A v^2 + ma_v \right) \cdot R_{tire} \\ & \underline{v}_k \le v_k \le \overline{v}_k, \forall k \\ & \underline{s}_k \le s_k \le \overline{s}_k, \forall k \end{aligned} \tag{4.8}$$

$$
\begin{aligned}
\min \quad & J = \sum_{k=0}^{N-1} \dot{m}_f(k) \\
s.t. \quad & T_e = \frac{T_{v_k}}{n_{gear}} \\
& \omega_e = v_k \cdot \frac{1}{R_{tire}} \cdot n_{gear} \\
& \dot{m}_f = f_e(\omega_e, T_e) \\
& s_k = \sum_{i=1}^{k} v_k dt \\
& T_v = \left(mg\mu + \frac{1}{2}\rho C_d A v^2 + m a_v \right) \cdot R_{tire} \\
& S\dot{O}C = -\frac{V_{oc} - \sqrt{V_{oc}^{\ 2} - 4R_{bat}P_{elect}}}{2 \cdot R_{bat}} \\
& P_{bat} = \omega_m \cdot T_m \cdot \eta_m \\
& \eta_m = f_m(\omega_m, T_m) \\
& \underline{v}_k \le v_k \le \overline{v}_k, \forall k \\
& \underline{s}_k \le s_k \le \overline{s}_k, \forall k
\end{aligned}
\tag{4.9}
$$

The relaxed optimization for the conventional vehicle has two controls (engine torque and transmission gear) and two states (vehicle speed and vehicle range), whereas the optimization problem for the parallel hybrid electric vehicle has three controls (engine torque, motor torque, and transmission gear) and three states (SOC, vehicle speed, range to the leading vehicle). The problem is nonlinear and non-convex that is inherited from the vehicle dynamics and the components' efficiency maps. Moreover, the problem has both continuous and discrete controls. In the following section, the DP method is employed to solve this problem by discretizing the continuous states and controls.

4.3 Dynamic Programming

DP is commonly used to solve non-linear non-convex optimal control problems because it can guarantee global optimality and manage constraints. To implement the DP algorithm, the original problem in Eq. (4.10) is decomposed into a set of sub-optimization problems for each time step k as shown in Eq. (4.11), where r_k represents the transitional

cost at step k, R_N represents the final cost at step N, and J_k refers to the optimal cost-to-go from step k to the final step N.

$$\min \quad J = \left(R_N\left(x_N\right) + \sum_{k=0}^{N-1} r_k\left(x_k, u_k\right) \right) \tag{4.10}$$

$$J_k\left(x_k\right) = \min\left\{ r_k\left(x_k, u_k\right) + J_{k+1}\left(x_{k+1}\right) \right\} \tag{4.11}$$

As shown in Figure 4.3, given all feasible controls (shown in green) and states, all sub-problems in Eq. (4.11) are optimized backward until the 1st stage is reached. Based on the Bellman's principle of optimality, the obtained results are guaranteed to be global optimal.

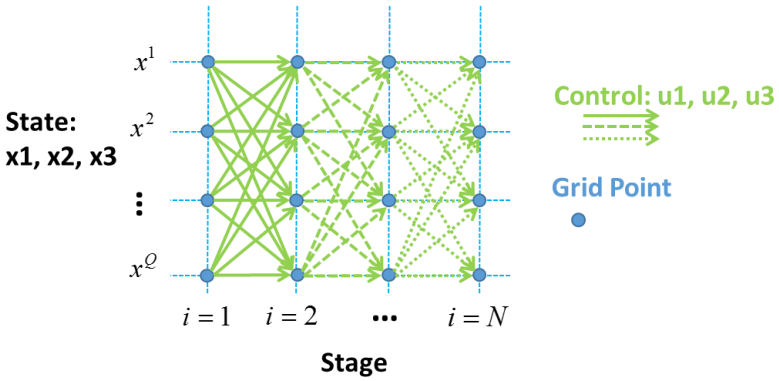

Figure 4.3 Backward optimization of DP process

4.4 Optimization Results

The simulation studies to be presented below cover four problem formulations: conventional (non-relaxed), conventional (relaxed), HEV (non-relaxed), and HEV (relaxed). Various driving scenarios are included and categorized into two types: constant speed scenarios (20, 30, 40 and 50 mph) for 200s and drive cycles (UDDS, HWFET, and NYCC). The vehicle speed constraint is set to ±2 mph, following the SAE fuel economy testing standard; the vehicle range difference is set to ±50 m. The major constraints are listed in Table 4.1, and key powertrain parameters are summarized in Table 4.2.

Table 4.1 Case Study Setup(F-150)

	Vehicle Speed (mph)	Vehicle Range Difference (m)	Battery SOC (%)
Constraint Range	±2 mph	±50 m	40 – 60

Table 4.2 Other Vehicle Parameters Used in Case Study (F-150)

Powertrain	Engine	MG Power	Battery Size	Vehicle Mass
Conventional	272 kW at 5200 rpm	N/A	N/A	2300 kg
Parallel Hybrid	272 kW at 5200 rpm	90 kW	1.35 kWh	2300 kg

4.4.1 Fuel Consumption Comparison

Fuel consumption results are shown in Figure 4.4 and Figure 4.5. These results confirm that relaxing the vehicle speed and battery SOC constraints can reduce fuel consumption. Relaxing the constraints within the EPA-defined tolerance can result in a fuel reduction of 2% - 73% compared to the optimal results without relaxations.

For constant speed driving, the fuel saving benefit from the HEV powertrain largely depends on the driving speed. Because the ICE operates efficiently, speed relaxation shows consistent and significant fuel saving even at high speeds. In this case, the hybrid system (i.e., battery SOC relaxation) does not present significant amount fuel saving. For low-speed drive cycles (NYCC, UDDS, and FTP-75), the HEV with speed relaxation presents the best fuel saving results; however, it seems that regenerative braking becomes a more important factor compared with relaxation. Overall, it could be inferred that the HEV powertrain is important in dynamic cycles with several opportunities for regenerative braking, whereas speed relaxation is more effective during constant-speed driving.

Moreover, results indicate that further fuel consumption reduction benefits can be derived if the average speed is low. At low-speed scenarios, engine operation in a conventional vehicle is considerably inefficient. Therefore, significant fuel consumption reduction opportunities exist for battery SOC relaxation and for speed relaxation. At high-

speed scenarios, the engine already operates at regions close to its "sweet spots" (optimum); consequently, less fuel consumption reduction benefit is observed. The average speed in different drive cycles are summarized in Table 4.3; the speed profile is shown in Figure 4.6.

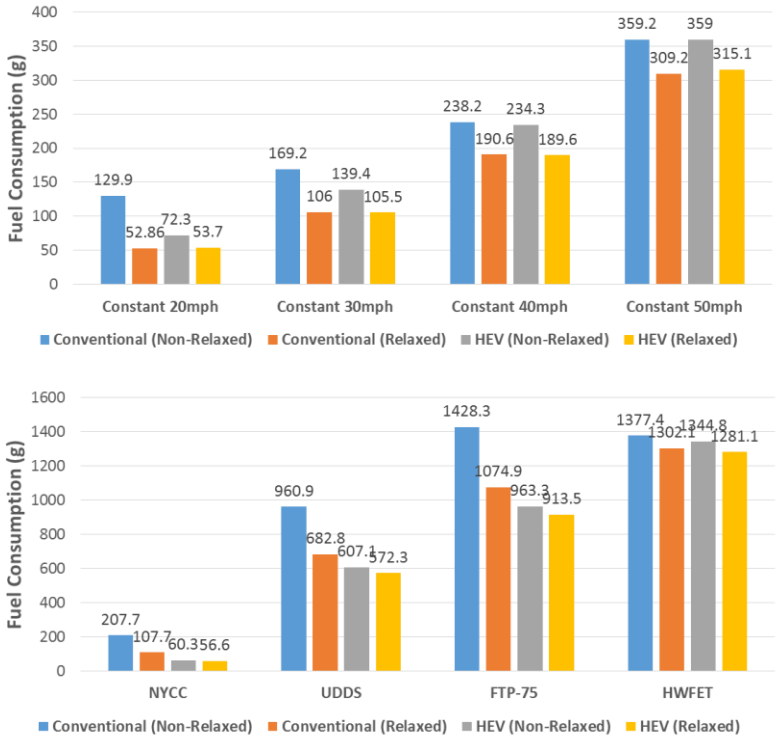

Figure 4.4 Fuel consumption comparison between constant speed scenarios and general drive cycle scenarios

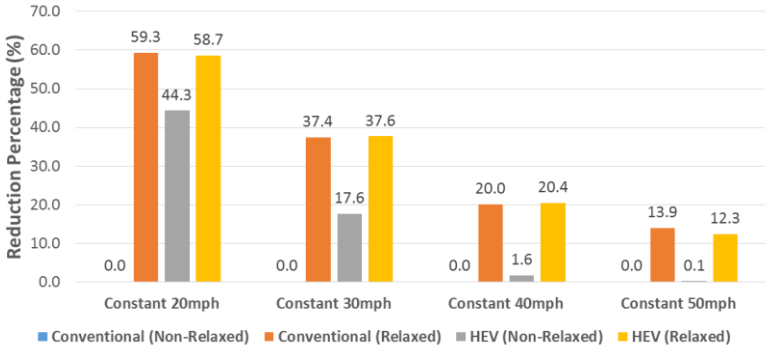

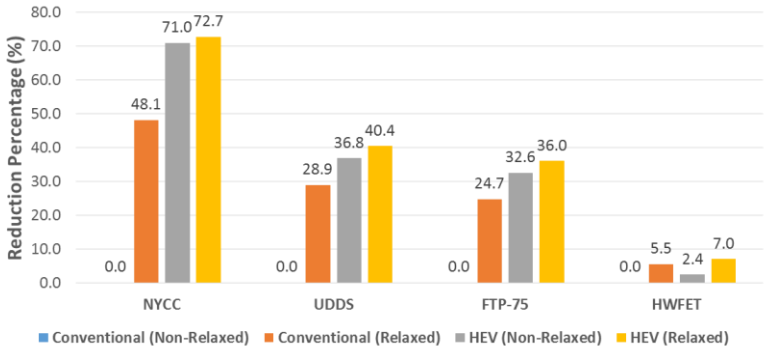

Figure 4.5 Fuel consumption reduction percentage in constant speed scenarios and general drive cycle scenarios

Table 4.3 Average Speeds of Studied Driving Scenarios (Excluding Stop Event)

Driving Scenarios	Constant 20mph	Constant 30mph	Constant 40mph	Constant 50mph
Average Speed	20mph	30mph	40mph	50mph
Driving Scenarios	New York City Cycle (NYCC)	Urban Dynamometer Driving Schedule (UDDS)	Federal Test Procedure (FTP-75)	Highway Fuel Economy Test (HWFET)
Average Speed	10.9mph	24.2mph	26.2mph	48.6mph

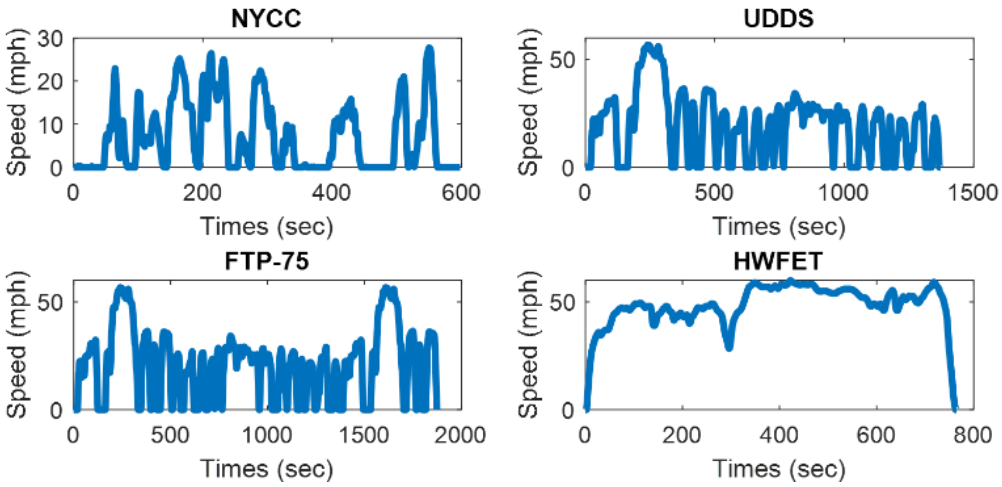

Figure 4.6 Speed profiles of NYCC, UDDS, FTP-75, and HWFET drive cycles

4.4.2 Speed and Battery SOC Trajectory Comparison

The optimized trajectories of vehicle speed and/or battery SOC of the three relaxed optimization cases (relaxed speed, relaxed SOC, and combined speed and SOC relaxation) at a constant speed of 30 mph and NYCC cycles are shown in Figure 4.7 – Figure 4.9.

Figure 4.7 shows the trajectory in the case study of the speed relaxation of the conventional vehicle. A pulse-and-glide behavior is observed in the vehicle speed trajectory. For the constant speed cases, the optimized vehicle speed fluctuates in the proximity of the desired speed, showing a period of approximately 5s. For the NYCC case, the optimized vehicle speed also fluctuates in the proximity of the desired speed and smooths out the profile if the original profile frequently changes.

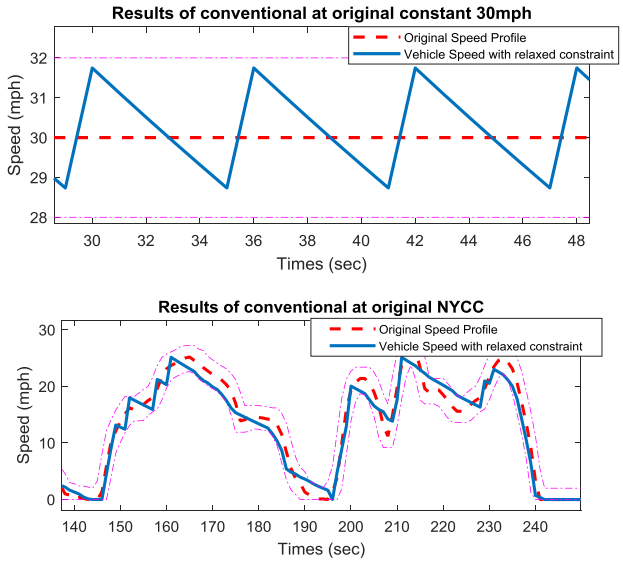

Figure 4.7 Optimized vehicle speed of relaxed optimization at 30mph and NYCC cycle

Figure 4.8 shows the trajectories of the case study for the battery SOC-only relaxation of the parallel HEV, i.e., a classic HEV. Pulse-and-glide behavior is observed for the SOC trajectory in the proximity of the desired final SOC value. In this case, vehicle speed follows the original profile exactly but SOC "pulses and glides".

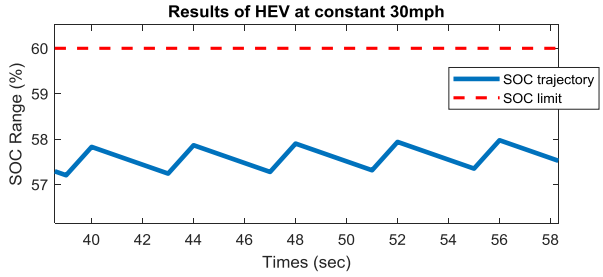

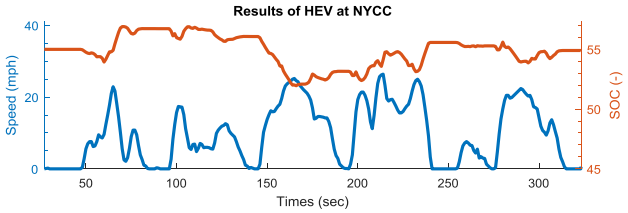

Figure 4.8 Optimized battery SOC trajectories (partial) of HEV at 30mph and NYCC

Figure 4.9 shows the trajectories of the case study for both vehicle speed and battery SOC relaxation of the parallel HEV. In the original constant speed case, the vehicle speed shows pulse-and-glide behavior while the battery SOC remains constant, implying that vehicle speed pulse-and-glide is preferred over battery SOC pulse-and-glide. In the NYCC case, both vehicle speed and battery SOC exhibit a pulse-and-glide behavior. Compared to the previous HEV case, the battery SOC changes are smaller and occur mostly during braking. The vehicle speed changes are still noticeable and occur along the whole horizon.

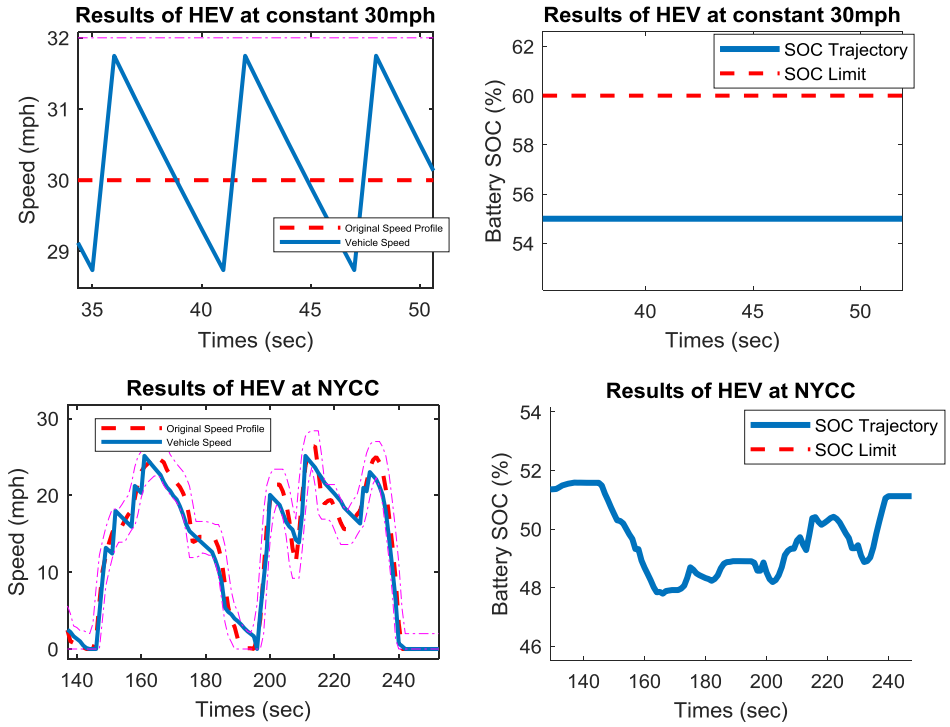

Figure 4.9 Optimized speed and battery SOC trajectories of HEV at 30mph and NYCC

Overall, pulse-and-glide behaviors are observed in the vehicle speed and battery SOC. From these comparisons, exploring the relaxation of both the speed and battery SOC constraints can balance the vehicle ride while achieving the lowest fuel consumption.

4.5 Optimization Analysis

Figure 4.10 shows the fuel consumption rates of different relaxation at the original constant driving scenario of 30 mph. Generally, the optimal engine powers are mostly at approximately 50 kW (near the "sweet spot" of the engine) or zero (engine shut-down). The final average fuel rates are lower than that at the same average power level as highlighted in the figure. Therefore, the overall fuel consumption is reduced.

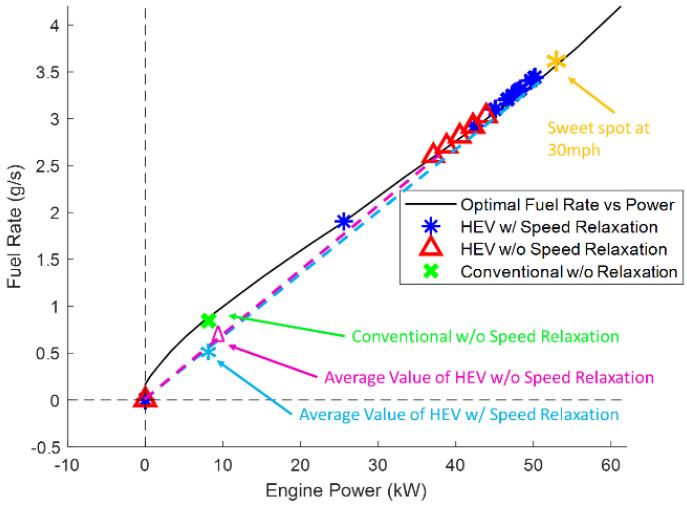

Figure 4.10 Optimized speed and battery SOC trajectories (partial) of HEV at 30mph and NYCC

Relaxing the vehicle speed allows the vehicle (body) to act as an (kinetic) energy storage system. The battery can replace the vehicle body to act as the energy buffer. Instead of speed fluctuation, the battery SOC will fluctuate up and down. As a result of the approximate 20% energy losses (charge and discharge) at the motor/power electronics and battery, the "SOC pulse-and-glide" is less efficient compared with the "Speed pulse-and-glide". The optimal results show that the kinetic energy storage (vehicle body) is preferred because it is more efficient. Because of the regenerative energy, the SOC will continue to still fluctuate to some extent. The energy flow of the HEVs relaxed optimization is shown in Figure 4.11.

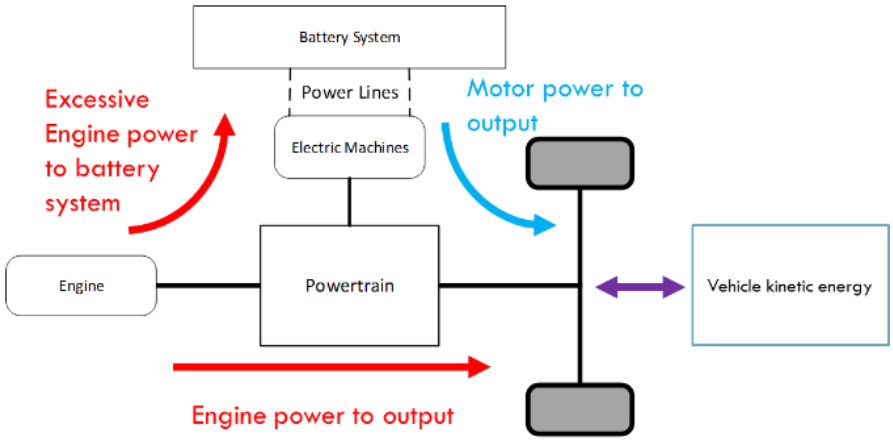

Figure 4.11 Energy flow in the relaxed optimization

4.6 Effects of the Boundary Conditions

The benefits of relaxed optimization depend on other conditions, such as the defined speed constraint bounds (at a given drive cycle, not at a constant speed), range constraint bounds, and drive cycle attributes. To further analyze these problems, simulations with different speed bounds, range bounds, and SOC bounds are performed. The constraint bounds are summarized in Table 4.4. The comparison in corresponding fuel consumption reduction percentages with the extended constraint bounds is shown in Figure 4.12.

Table 4.4 Extended Constraint Bounds used in Simulations

	Vehicle Speed (mph)	Vehicle Position Offset (m)	Battery SOC (%)
Constraint Range	±10	±250	10 – 90

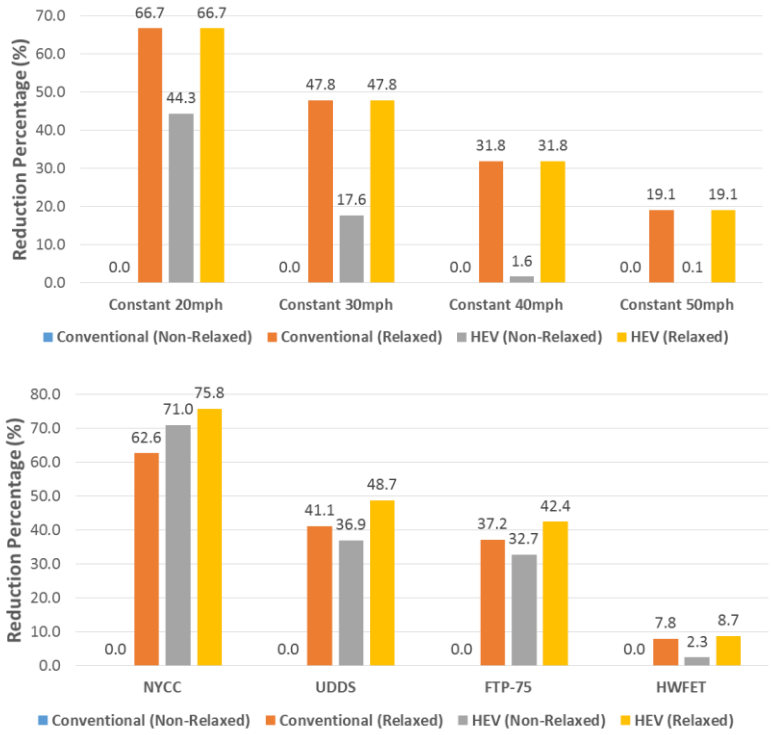

Figure 4.12 Percentages of fuel consumption reduction in constant speed scenarios and general drive cycle scenarios, with extended constraint bounds

Results show that further fuel consumption reductions of up to 76% are achieved. Larger constraint bounds generally result in higher fuel consumption reductions.

Figure 4.13 shows vehicle speed trajectories with the extended constraints. The speed profiles still exhibit the pulse-and-glide behavior. The speed trajectory becomes smoother because the pulse-and-glide period is longer. It can be noted that the vehicle speed does not always fully utilize an upper bound higher than 7mph, because a higher speed indicates a higher aerodynamic-drag.

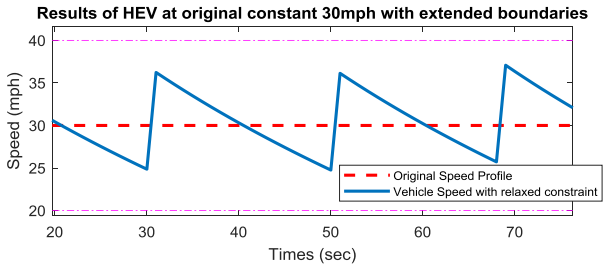

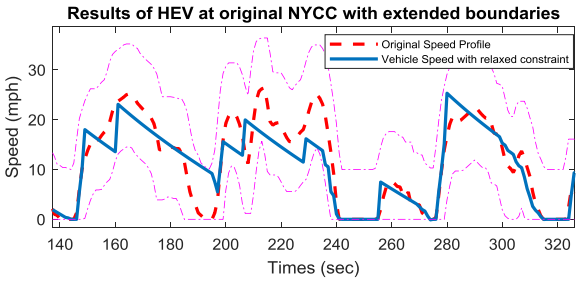

Figure 4.13 Speed trajectories of relaxed optimization using the extended constraint bounds at original constant 30 mph and NYCC drive cycles

Among all constraints, the effects of speed constraint are most significant. Additional case studies on other constraints (range and battery SOC) are provided in Appendix B.

Table 4.5 Extended Constraint Bounds in Different Constraint Case Studies

	Vehicle Speed (mph)	Vehicle Position Offset (m)	Battery SOC (%)
Constraint Range (Case 1: Speed)	±2 – ±10	±50	40 – 60

Figure 4.14 shows the fuel consumption reduction when speed relaxation is made to vary. Results show that for both powertrains, generally, a larger speed bound results in lower fuel consumptions when the bounds are smaller than ±10 mph from the nominal speed. Larger speed bounds allow the vehicle to pulse with a larger acceleration. This permits a larger output power from the powertrain and allows the engine to operate closer to the sweet-spot power points, as indicated in Figure 4.10. The benefits saturate when these sweet-spot power operating points are reached. On the other hand, the overall driving becomes smoother because the larger speed bound results in a longer pulse-and-glide period.

For the conventional vehicle, results show more fuel consumption reduction improvements at lower speeds. Speed bounds larger than ±7 mph stop generating more fuel saving. A similar trend is observed in the HEV case; however, fuel saving is lower. This is because the HEV is already more efficient.

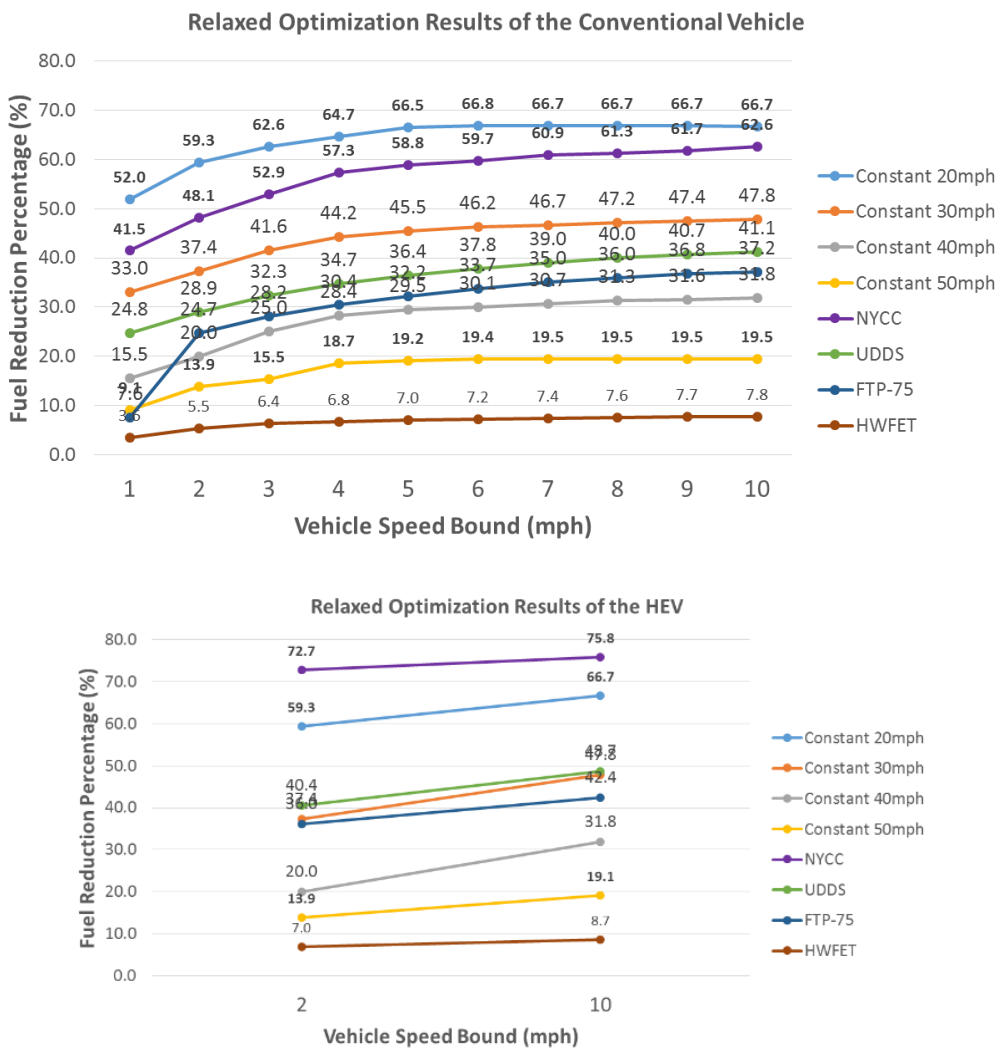

Figure 4.14 Fuel consumption reduction for varying speed constraints under different driving scenarios

To further analyze these problems in the general driving scenarios, more simulations are desired. However, using DP to solve the problem is time consuming: more than nine days to complete the simulation in the HWFET cycle and two weeks in the UDDS cycle for the relaxed optimization. This is because the DP is unable to manage the curse of dimensionality. Different methods are required to handle these optimization problems.

Additional studies are also conducted on computational cost to identify methods that can be used to solve mixed-integer optimization problems, such as the DP and MIP. As shown in Figure 4.15, two methods are used to solve a conventional vehicle optimal control problem over different drive cycles with only one control (transmission gear). The DP requires more computational time than MIP when the drive cycle is short; more, the

time consumed by the DP increases linearly as the drive cycle extends. The time consumed by the MIP increases exponentially, and eventually takes longer time than the DP. The MIP method is not an ideal option for solving long horizon problems.

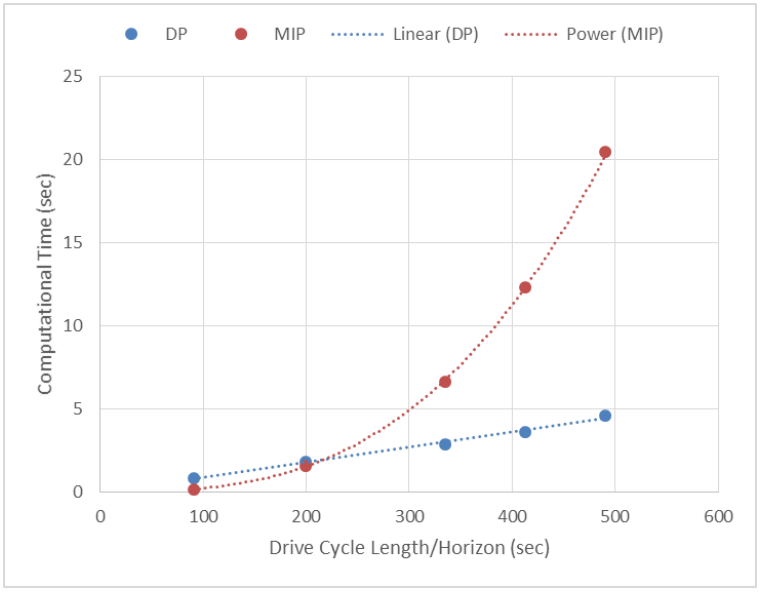

Figure 4.15 Computational time of different cycles using DP and MIP

Figure 4.16 shows how the computational time of the DP increases exponentially when the number of states/controls increases. The exponential increase is due to the curse of dimensionality, and shows that DP is not an ideal option for the relaxed optimization of HEVs because of the increased number of states.

Therefore, in this dissertation we propose to use the multi-parametric programming method to solve the relaxed optimization problems for HEVs in the next Chapter.

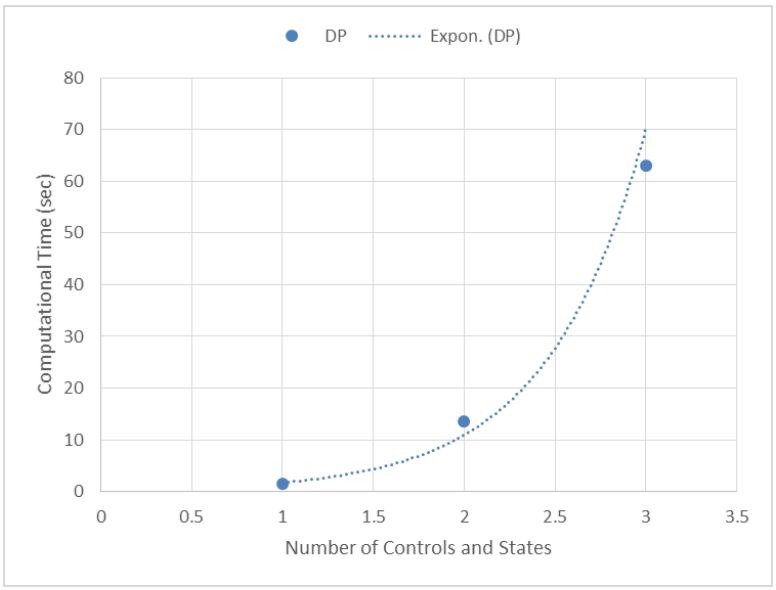

Figure 4.16 Computational time of number of controls and states using DP to solve a 200s drive cycle

CHAPTER 5
Multi-Parametric Programming for Hybrid Vehicle Control Optimization

In Chapter 4, the relaxed optimization for vehicle control is defined, formulated, and solved for conventional and parallel hybrid powertrains. The optimal fuel benefits and optimized control are analyzed.

However, solving the relaxed optimization for the parallel HEV suffers from the curse of dimensionality (e.g., two controls and two states for this problem) when the DP method is applied. This indicates that it is limited to solve higher degrees-of-freedom (DOFs) optimization problems, such as the relaxed optimization of the AWD power-split HEV, using the DP method, except for people who have access to significant computation resources.

In this chapter, the multi-parametric programming (MPP) method is introduced and utilized to solve the HEV control optimization problem. The generic solution formulation is developed, and the optimality and computational efficiency of this method are verified. The developed solution formulation is also adapted for the relaxed optimization of the AWD power-split HEV.

5.1 Problem Approximation and Reformulation

The HEV optimization problems are typically either non-convex problems or mixed-integer non-convex problems. To solve these high-order optimization problems using the MPP method, the optimization problem is approximated and parameterized instead of discretizing or approximating controls and states. Thereafter, the high-dimensional non-convex non-linear HEV optimization problem is firstly analyzed:

1. The mechanical path of the powertrain dynamic is linear;

2. The battery dynamic is non-linear (a square root function);

3. The map data of components is non-convex (e.g., engine fuel map and motor efficiency map).

Then, the following technique and approximation are adopted:

1. The linear dynamic of the mechanical path remains;

2. The non-linear battery dynamics is replaced by a linear energy model;

3. The non-convex engine fuel map and motor efficiency maps(s) are approximated with piece-wise linear maps.

The original HEV optimization problem then becomes a piece-wise linear convex optimization problem. The process of this approximation is shown by the diagram in Figure 5.1. Further details are provided in the next section.

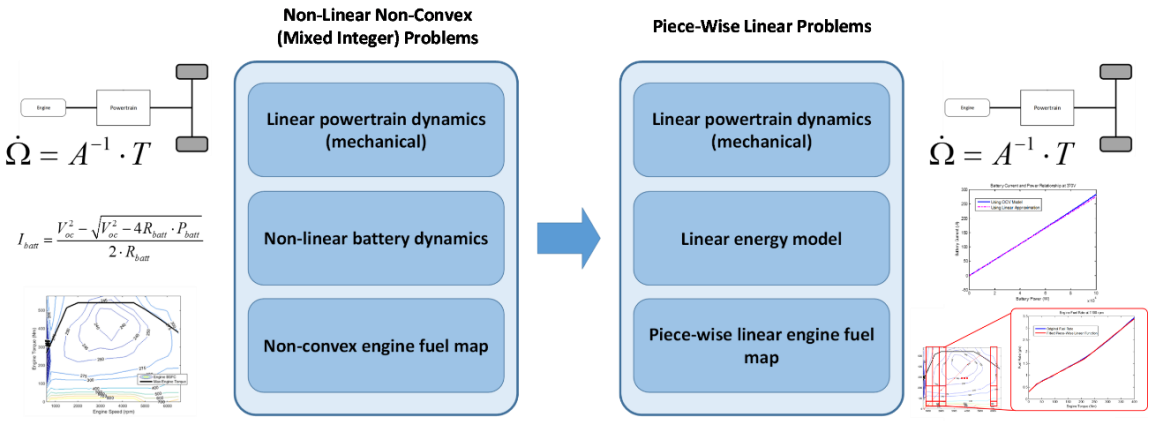

Figure 5.1 Approximation of HEV optimization problems

5.1.1 Linearization of Engine Fuel Map

The engine fuel map is first decomposed into several engine map segments based on engine speed and torque, shown in Figure 5.2. The fuel rate in each engine map segment is approximated by a linear function of the engine torque. Figure 5.3 shows an example of the resulting fuel rate approximation at engine speed of 1100 rpm.

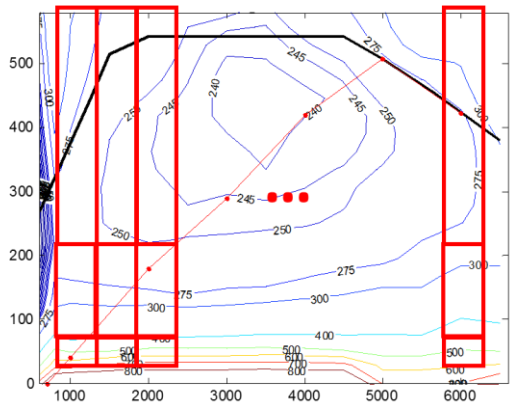

Figure 5.2 Engine fuel map decomposed into several smaller segments (in red)

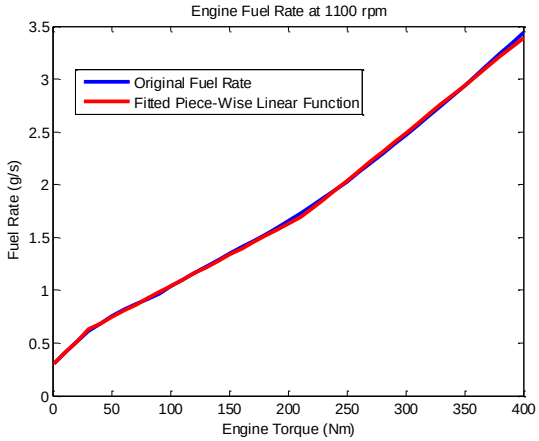

Figure 5.3 Approximated fuel consumption using a piece-wise linear function at engine speed of

The engine fuel rate map is then decomposed into a group of piece-wise linear functions. The general approximation is given in Eq. (5.1), where $\bar{\omega}_{e,i}$ is the average engine speed in the i^{th} engine speed segment to approximate ω_e within that segment.

$$\dot{m}_{fuel} = \alpha_0^{h_1,h_2} + \alpha_1^{h_1,h_2} \cdot \bar{\omega}_{e,i} + \alpha_2^{h_1,h_2} \cdot T_e$$
$$h_1 \in \{1,2,...,20\}; h_2 \in \{1,2,3\} \qquad (5.1)$$
$$h_1 : \text{engine speed segment}, h_2 : \text{torque segment}$$

The analysis of Figure 5.4 shows that 99% of the approximation data points are less than 5% different from the original data points and the remaining 1% approximated points are between 5-10% from the original points. Moreover, the non-convexity of the original fuel map is inherited in this approximation. Therefore, the approximated piece-wise linear

fuel functions are valid to replace the original fuel map in the optimization problem. The factors $\alpha^{h1,h2}{}_0$, $\alpha^{h1,h2}{}_1$ and $\alpha^{h1,h2}{}_2$ of those piece-wise linear functions in Eq. (5.1) are constant; they are determined from the fuel map through least square regression.

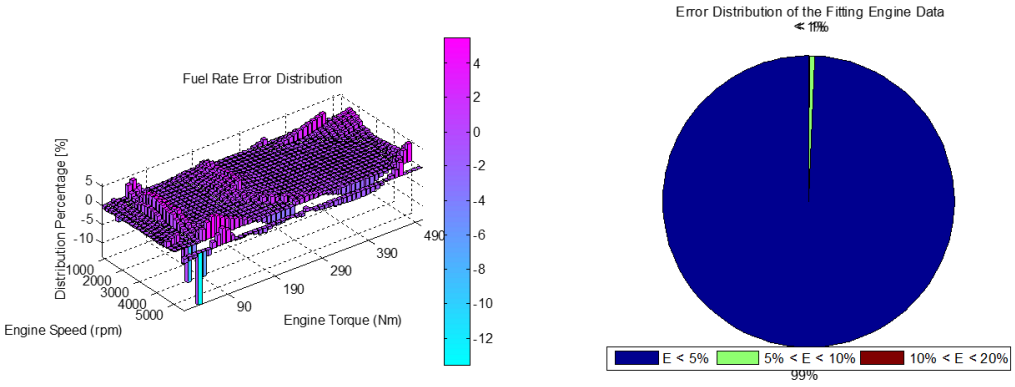

Figure 5.4 Analysis using engine fuel map approximation

5.1.2 Approximation of Motor Speed

Because the engine speed is approximated by the average speed ($\bar{\omega}_{e,h_1}$) in the corresponding segment, the motor speed is approximated by Eq. (5.3) for this parallel hybrid vehicle design.

$$\omega_m = \bar{\omega}_{e,h_1} \quad h_1 : \text{engine segment} \tag{5.2}$$

The motor speed approximation is dependent on the engine grid point. For example, if the engine speed is 1000 rpm and the engine grid point is 100 rpm, then the approximation error is less than 5% within the segment of approximately 1000 rpm.

It should be noted that this approximation is only for the purpose of converting the problem to be piece-wise mixed-integer linear programming. If the problem is formulated as a quadratic programming, then this approximation for motor speed is not necessary.

5.1.3 Linearized Energy Model

The mostly frequently used open circuit voltage (OCV) battery model, shown in Figure 5.5, consists of a square root function of the battery power in terms of the battery current. This is given by in Eq. (5.3), where V_{oc} is the battery open circuit voltage, R_{batt} is the internal resistance, I_{batt} is the battery current, and P_{batt} is the battery output power. Eq.

(5.4) shows the relationship between the battery state of charge (SOC) and the battery current. E_{tot} is the total energy of the battery pack, and ΔSOC is the battery SOC change rate.

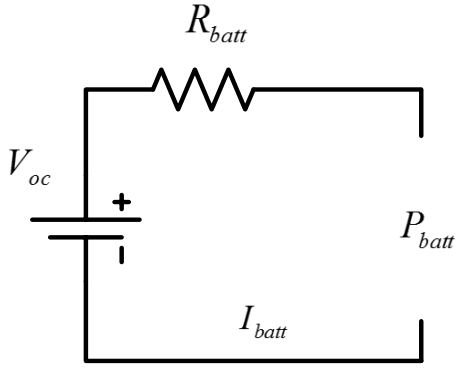

Figure 5.5 Battery open circuit voltage model

$$I_{batt} = \frac{V_{oc}^2 - \sqrt{V_{oc}^2 - 4R_{batt} \cdot P_{batt}}}{2 \cdot R_{batt}} \tag{5.3}$$

$$\Delta SOC = \frac{I_{batt}}{E_{total}} \tag{5.4}$$

Because the battery internal resistance can be relatively small, the battery current is then approximated as an affine function of the battery power, i.e., a linear energy model. Figure 5.6 shows the comparison of the calculated battery current from Eq. (5.3) and from an approximate affine function in Eq. (5.5), and the results verify the OCV model is closely approximated by the linear energy model. An analysis of the comparison in Figure 5.7 shows that 57% of the data are within a 1% difference and over 97% of the data are within a 5% error. The remaining 3% with a larger error locates at areas with considerably low power. The factors β_0 and β_1 of the affine function in Eq. (5.5) are constant and determined through least square regression from the OCV model.

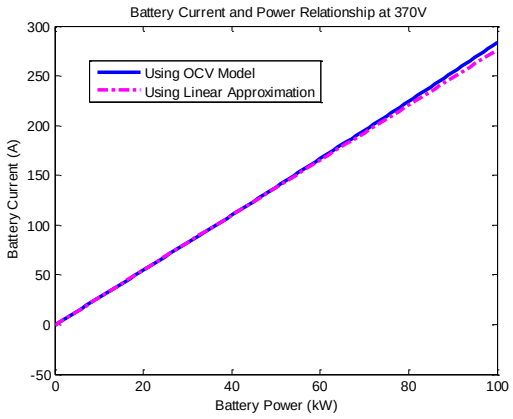

Figure 5.6 Battery OCV model and its linear approximation

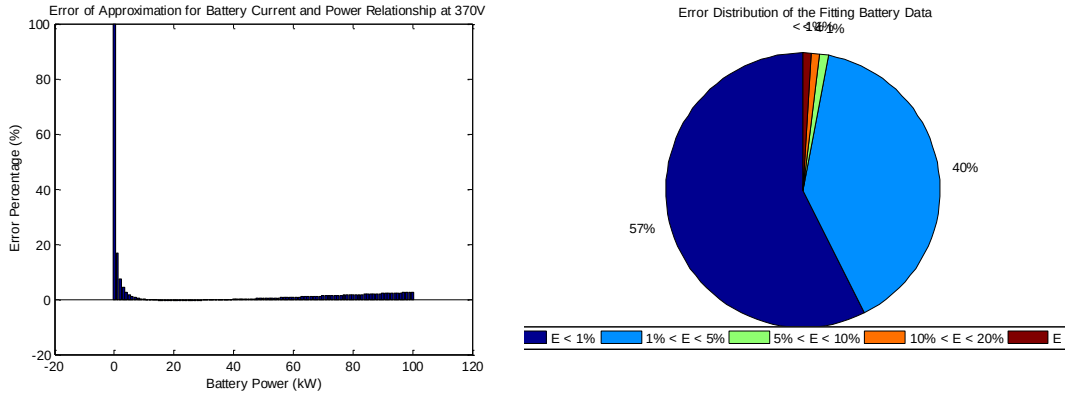

Figure 5.7 Analysis using the linear battery model approximation accuracy

$$I_{batt} = \beta_1 \cdot P_{batt} + \beta_0 \tag{5.5}$$

$$\Delta SOC = \frac{I_{batt}}{E_{total}} \tag{5.6}$$

5.1.4 Problem Formulation

By incorporating the above approximations, the piece-wise linear convex optimization of the HEV is formulated in the below, where $\bar{T}_{e,h_2}$ is the mid-point of each torque segment and *gr* is the transmission gear ratio:

$$
\begin{aligned}
&\min \quad \sum_{t=1}^{N} f(t) \\
&f(t) = \left(\alpha_0^{h_1,h_2} + \alpha_1^{h_1,h_2} \cdot \omega_e(t) + \alpha_2^{h_1,h_2} \cdot T_e(t)\right) \\
&\omega_e(t) = \omega_m(t) = \bar{\omega}_{e,i} \\
&T_m(t) = \frac{T_v(t)}{gr} - T_e(t) \\
&P_m(t) = \omega_m(t) \cdot T_m(t) \\
&\Delta SOC(t) = \frac{1}{E_{total}} \cdot \left(\beta_1 \cdot P_m(t) + \beta_0\right) \\
&h_1 = \min\left|\bar{\omega}_{e,h_1} - \omega_v(t) \cdot gr\right|, h_1 \in \{1,2,...,20\} \\
&h_2 = \min\left|\bar{T}_{e,h_2} - T_e\right|, h_2 \in \{1,2,3\}
\end{aligned}
\tag{5.7}
$$

The MPP method is used to solve this optimization as explained in the next section. As an example, the problem is optimized over a 55-mph cruising cycle for 8s.

5.2 Use of MPP to Solve Hybrid Vehicle Non-Relaxed Optimization Problem

5.2.1 Multi-Parametric Programming Process

The optimization of a parallel hybrid vehicle (Eq. (5.7)) is formulated as a series of stage decision processes represented in Figure 5.8, where u^1_t is the control of motor torque T_m at time t, u^2_t is the control of the transmission gear N_{gear} at time t, x^1_t is the state of battery SOC SOC_{bat} at time t, x^2_t is the state of transmission gear N_{gear} at time t, and s_t is the cost-to-go of fuel cost $fuel_t$ at time t.

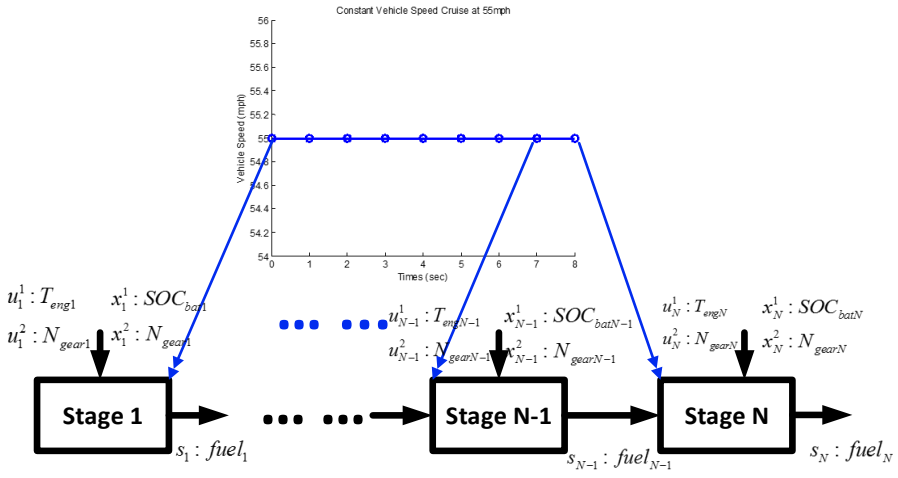

Figure 5.8 Schematic of HEV optimization problem with N ($N=8$) stages

Following a process similar to solving dynamic programming of solving a group of sub-problems in Eq. (5.7), the MPP method starts from the end stage $i=N$. At this stage, the optimization in Eq. (5.7) has the decision vector $X_N=[u^1_N, u^2_N, x^1_N, x^2_N]$, which includes both the control and state vector, and the parameter vector θ for the cost-to-go function as $V_{i=N}(\theta)$. In this case of HEV optimization, the decision vector includes MG1 torque command T_{mg1}, gear ratio command gr (for next time-step), current SOC state soc, and current gear ratio state gr. The sub-problem at stage $i=N$ is then developed as Eq. (5.8), where soc_N is the SOC state at time step N, $SOC_{desired}$ is the desired SOC, $\omega_{v\_desired}$ is the desired transmission speed, and $T_{v\_desired}$ is the desired vehicle torque. The cost-to-go and its complete representation format are described in Eqs. (5.9) and (5.10). The cost-to-go is also plotted in Figure 5.9. The optimal control of the sub-problem Eq. (5.8) is expressed in Eq. (5.11).

$$
\begin{aligned}
&V_N = \min \quad f\left(N\right)\\
&f\left(N\right) = f\left(\omega_{e_N}, T_{e_N}\right) = \left(\alpha_0^{h_1,h_2} + \alpha_1^{h_1,h_2}\cdot\omega_{e_N} + \alpha_2^{h_1,h_2}\cdot T_{e_N}\right)\\
&\omega_{e_N} = \omega_{m_N} = \bar{\omega}_{e_N,h}\\
&T_{m_N} = \frac{T_{v_N}}{gr_{c,N}} - T_{e_N}\\
&P_{m_N} = \omega_{m_N}\cdot T_{m_N}\\
&\Delta SOC_N = \frac{1}{E_{total}}\cdot\left(\beta_1^{h_1}\cdot P_{m_N} + \beta_0^{h_1}\right)\\
&\Delta SOC_N = \left(soc_N - SOC_{desired}\right)/\Delta t\\
&\omega_{v_N} = \omega_{v\_desired}\\
&T_{v_N} = T_{v\_desired}\\
&h_1 = \min\left|\bar{\omega}_{e_N,h_1} - \omega_{v_N}\cdot gr_{c,N}\right|\\
&h_1 \in \{1,2,...,20\}: \text{engine speed segment}\\
&h_2 = \min\left|\bar{T}_{e,h_2} - T_e\right|\\
&h_2 \in \{1,2,3\}: \text{torque segment}
\end{aligned}
\tag{5.8}
$$

$$
\begin{aligned}
V_{N,i} \quad = \quad & \alpha_0^{h_1,h_2} + \alpha_1^{h_1,h_2} \cdot \bar{\omega}_{e_N,h_1} \\
& + \alpha_2^{h_1,h_2} \cdot \left[\frac{T_{v_N}}{gr_N} + \frac{E_{total} \cdot SOC_{desired} + \beta_0^{h_1} \cdot \Delta t}{\bar{\omega}_{e_N,h} \cdot \beta_1^h \cdot \Delta t} \right] \\
& - \frac{\alpha_2^{h_1,h_2} \cdot E_{total}}{\bar{\omega}_{e_N,h_1} \cdot \beta_1^{h_1} \cdot \Delta t} \cdot soc_N
\end{aligned} \tag{5.9}
$$

$i \in \{1,2,3\}$: battery SOC region

$$
\begin{aligned}
V_{N,i}(\theta) \quad = \quad & A_N' \cdot \theta + B_N' \\
= \quad & \begin{bmatrix} a_1 & a_2 & a_3 & a_4 \end{bmatrix} \begin{bmatrix} u_N^1 \\ u_N^2 \\ x_N^1 \\ x_N^2 \end{bmatrix} + B_N' \\
= \quad & \begin{bmatrix} 0 & 0 & -\frac{\alpha_2^{h_1,h_2} \cdot E_{total}}{\bar{\omega}_{e_N,h_1} \cdot \beta_1^h \cdot \Delta t} & 0 \end{bmatrix} \begin{bmatrix} u_N^1 \\ u_N^2 \\ x_N^1 \\ x_N^2 \end{bmatrix} \\
& + \alpha_0^{h_1,h_2} + \alpha_1^{h_1,h_2} \cdot \bar{\omega}_{e_N,h_1} \\
& + \alpha_2^{h_1,h_2} \cdot \left[\frac{T_{v_N}}{gr_{c,N}} + \frac{E_{total} \cdot SOC_{desired} + \beta_0^{h_1} \cdot \Delta t}{\bar{\omega}_{e_N,h_1} \cdot \beta_1^{h_1} \cdot \Delta t} \right]
\end{aligned} \tag{5.10}
$$

$$
\theta = \begin{bmatrix} u_N^1 & u_N^2 & x_N^1 & x_N^2 \end{bmatrix}' = \begin{bmatrix} T_{m_N} & gr_{c,N} & soc_N & gr_{s,N} \end{bmatrix}'
$$

$$
\begin{aligned}
u_{N,i}{}' &= \begin{bmatrix} u_{N,i}^{1}{}' \\ u_{N,i}^{2}{}' \end{bmatrix} = \begin{bmatrix} T_{m_N} \\ gr_{c,N} \end{bmatrix} \\
u_{N,i}{}' &= C_N{}' \cdot \theta + D_N{}' \\
&= \begin{bmatrix} c_{N,1}{}' & c_{N,2}{}' & c_{N,3}{}' & c_{N,4}{}' \\ c_{N,5}{}' & c_{N,6}{}' & c_{N,7}{}' & c_{N,8}{}' \end{bmatrix} \begin{bmatrix} u_N^1 \\ u_N^2 \\ x_N^1 \\ x_N^2 \end{bmatrix} + \begin{bmatrix} d_{N,1}{}' \\ d_{N,2}{}' \end{bmatrix} \\
&= \begin{bmatrix} 0 & 0 & \dfrac{E_{total}}{\bar{\omega}_{e_N,h_1} \cdot \beta_1^{h_1} \cdot \Delta t} & 0 \\ 0 & 0 & 0 & 0 \end{bmatrix} \begin{bmatrix} u_N^1 \\ u_N^2 \\ x_N^1 \\ x_N^2 \end{bmatrix} \\
&\quad + \begin{bmatrix} -\dfrac{E_{total} \cdot SOC_{desired} + \beta_0^{h_1} \cdot \Delta t}{\bar{\omega}_{e_N,h_1} \cdot \beta_1^{h_1} \cdot \Delta t} \\ gr_{opt} \end{bmatrix}
\end{aligned}
\tag{5.11}
$$

$$\left\{ f_{N-1}\left(\omega_v, T_v, gr_{opt}\right)\big|_{\omega_v, T_v, \Delta soc} \Rightarrow \text{minimum} \right\}$$

$i \in \{1,2,3\}$: battery SOC region

$x_N^1 = soc_N \in \left[SOC_{N,i}, SOC_{N,i+1} \right]$

$$
\begin{aligned}
SOC_{N,1} &= SOC_{desired} + \frac{\Delta t}{E_{total}} \cdot \left[\left(\frac{T_{v_N}}{gr_{c,N}} - T_{e_N,4} \right) \cdot \bar{\omega}_{e_N,h_1} \cdot \beta_1^{h_1} + \beta_0^{h_1} \right] \\
SOC_{N,2} &= SOC_{desired} + \frac{\Delta t}{E_{total}} \cdot \left[\left(\frac{T_{v_N}}{gr_{c,N}} - T_{e_N,3} \right) \cdot \bar{\omega}_{e_N,h_1} \cdot \beta_1^{h_1} + \beta_0^{h_1} \right] \\
SOC_{N,3} &= SOC_{desired} + \frac{\Delta t}{E_{total}} \cdot \left[\left(\frac{T_{v_N}}{gr_{c,N}} - T_{e_N,2} \right) \cdot \bar{\omega}_{e_N,h_1} \cdot \beta_1^{h_1} + \beta_0^{h_1} \right] \\
SOC_{N,4} &= SOC_{desired} + \frac{\Delta t}{E_{total}} \cdot \left[\left(\frac{T_{v_N}}{gr_{c,N}} - T_{e_N,1} \right) \cdot \bar{\omega}_{e_N,h_1} \cdot \beta_1^{h_1} + \beta_0^{h_1} \right]
\end{aligned}
\tag{5.12}
$$

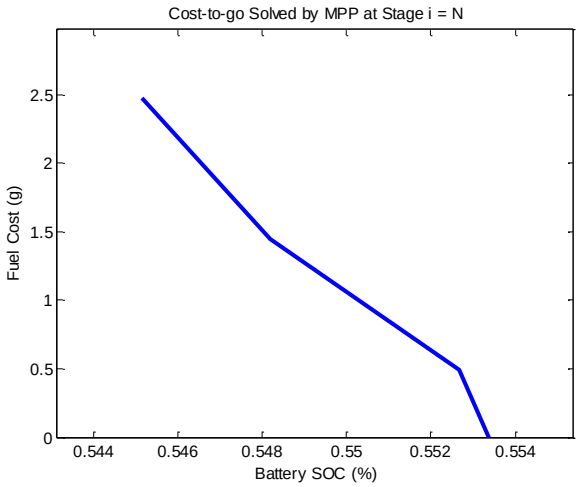

Figure 5.9 Cost-to-go function at stage $i=N$

The optimization problem in Eq. (5.7) is then solved from stage $i=N$ back to stage $i=1$ based on the optimality principle proposed by Bellman [49]. In general terms, this principle states that, given an optimal path V_i, from i to N, the optimal path from k to N, that passes by i, also contains V_i.

At stage $i=N-1$, the sub-problem of Eq. (5.7) is shown in Eq. (5.13). To solve Eq. (5.13), all the constants in the transitional cost are replaced by B_{N-1} and factors related to the controls and states as A_{N-1}. Then, the solution to the sub-optimization problem is shown in Eqs. (5.14) – (5.20), with the cost-to-go in Eqs. (5.14) – (5.16) and optimal control in Eqs. (5.17) – (5.20).

$$
\begin{aligned}
&V_{N-1} = \min \quad f_{N-1}\left(u_{N-1}^{1}, u_{N-1}^{2}, x_{N-1}^{1}, x_{N-1}^{2}, \theta_N\right) + V_{N,j}\left(\theta_N\right)\big|_{x_N^1} \\
&f_{N-1}\left(\omega_{e_{N-1}}, T_{e_{N-1}}\right) = \left(\alpha_0^{h_{1,N-1},h_{2,N-1}} + \alpha_1^{h_{1,N-1},h_{2,N-1}} \cdot \omega_{e_{N-1}} + \alpha_2^{h_{1,N-1},h_{2,N-1}} \cdot T_{e_{N-1}}\right) \\
&V_{N,i}\left(\theta\right) = \begin{bmatrix} 0 & 0 & -\dfrac{\alpha_2^{h_{1,N},h_{2,N}} \cdot E_{total}}{\bar{\omega}_{e_N,h_{1,N}} \cdot \beta_1^{h_N} \cdot \Delta t} & 0 \end{bmatrix} \begin{bmatrix} T_{m_N} \\ gr_{c,N} \\ soc_N \\ gr_{s,N} \end{bmatrix} \\
&\qquad + \alpha_0^{h_{1,N},h_{2,N}} + \alpha_1^{h_{1,N},h_{2,N}} \cdot \bar{\omega}_{e_N,h_{1,N},h_{2,N}} \\
&\qquad + \alpha_2^{h_{1,N},h_{2,N}} \cdot \left[\frac{T_{v_N}}{gr_{c,N}} + \frac{E_{total} \cdot SOC_i + \beta_0^{h_{1,N}} \cdot \Delta t}{\bar{\omega}_{e_N,h_{1,N}} \cdot \beta_1^{h_{1,N}} \cdot \Delta t}\right] \\
&\omega_{e_{N-1}} = \omega_{m_{N-1}} = \bar{\omega}_{e_{N-1},h_{1,N-1}} \\
&T_{m_{N-1}} = \frac{T_{v_{N-1}}}{gr_{c,N-1}} - T_{e_{N-1}} \\
&P_{m_{N-1}} = \omega_{m_{N-1}} \cdot T_{m_{N-1}} \\
&\Delta SOC_{N-1} = \frac{1}{E_{total}} \cdot \left(\beta_1^{h_{1,N-1}} \cdot P_{m_{N-1}} + \beta_0^{h_{1,N-1}}\right) \\
&\Delta SOC_{N-1} = \left(SOC_{N-1} - SOC_N\right) / \Delta t \\
&i \in \{1,2,3\} : \text{battery SOC region} \\
&h_{1,N-1} = \min\left|\bar{\omega}_{e_{N-1},h_1} - \omega_{v_{N-1}} \cdot gr_{c,N-1}\right| \\
&h_{1,N-1} \in \{1,2,...,20\} : \text{engine speed segment} \\
&h_{2,N-1} = \min\left|\bar{T}_{e,h_2} - T_e\right| \\
&h_{2,N-1} \in \{1,2,3\} : \text{torque segment}
\end{aligned}
\tag{5.13}
$$

$$
\begin{aligned}
&V_{N-1,i}\left(\theta\right) = A_{N-1,i}{}' \cdot \theta + B_{N-1,i}{}' \\
&i \in \left\{1,2,3,4,5,6\right\} : \text{battery SOC region} \\
&h_{1,N-1} = \min\left|\bar{\omega}_{e_{N-1},h_{1,N-1}} - \omega_{v_{N-1}} \cdot gr_{c,N-1}\right| \\
&h_{1,N-1} \in \left\{1,2,...,20\right\} : \text{engine speed segment} \\
&h_{1,N} = \min\left|\bar{\omega}_{e_N,h_{1,N}} - \omega_{v_N} \cdot gr_{c,N}\right| \\
&h_{1,N} \in \left\{1,2,...,20\right\} : \text{engine speed segment} \\
&h_{2,N-1} = \min\left|\bar{T}_{e,h_2} - T_e\right| \\
&h_{2,N-1} \in \left\{1,2,3\right\} : \text{torque segment} \\
&h_{2,N} = \min\left|\bar{T}_{e,h_2} - T_e\right| \\
&h_{2,N} \in \left\{1,2,3\right\} : \text{torque segment}
\end{aligned}
\tag{5.14}
$$

$$
\begin{aligned}
&A_{N-1,i}{}' = \left[\, a^1_{N-1,i} \quad a^2_{N-1,i} \quad a^3_{N-1,i} \quad a^4_{N-1,i} \,\right] \\
&a^1_{N-1,i} = 0 \\
&a^2_{N-1,i} = 0 \\
&a^4_{N-1,i} = 0
\end{aligned}
$$

$$
a^3_{N-1,i} = \begin{cases}
a^3_{N,1} & , \quad i = 1, SOC_{N-1} \in \left[\, SOC_{N-1,1}, SOC_{N-1,2} \,\right] \\
-\dfrac{\alpha^3_2 \cdot E_{total}}{\bar{\omega}_{e_{N-1},h_{1,N-1}} \cdot \beta_1^{h_{1,N-1}} \cdot \Delta t} & , \quad i = 2, SOC_{N-1} \in \left[\, SOC_{N-1,2}, SOC_{N-1,3} \,\right] \\
a^3_{N,2} & , \quad i = 3, SOC_{N-1} \in \left[\, SOC_{N-1,3}, SOC_{N-1,4} \,\right]
\end{cases}
\tag{5.15}
$$

$$
a^3_{N-1,i} = \begin{cases}
-\dfrac{\alpha^3_2 \cdot E_{total}}{\bar{\omega}_{e_{N-1},h_{1,N-1}} \cdot \beta_1^{h_{1,N-1}}{}_1 \cdot \Delta t} & , \quad i = 4, SOC_{N-1} \in \left[\, SOC_{N-1,4}, SOC_{N-1,5} \,\right] \\
-\dfrac{\alpha^2_2 \cdot E_{total}}{\bar{\omega}_{e_{N-1},h_{1,N-1}} \cdot \beta_1^{h_{1,N-1}} \cdot \Delta t} & , \quad i = 5, SOC_{N-1} \in \left[\, SOC_{N-1,5}, SOC_{N-1,6} \,\right] \\
-\dfrac{\alpha^1_2 \cdot E_{total}}{\bar{\omega}_{e_{N-1},h_{1,N-1}} \cdot \beta_1^{h_{1,N-1}} \cdot \Delta t} & , \quad i = 6, SOC_{N-1} \in \left[\, SOC_{N-1,6}, SOC_{N-1,7} \,\right]
\end{cases}
$$

$$B_{N-1,i}{}' = \begin{cases} \dfrac{\alpha_2^3 \cdot E_{total} \cdot SOC_{N-1,3}}{\bar{\omega}_{e_{N-1},h_{1,N-1}} \cdot \beta_1^{h_{1,N-1}} \cdot \Delta t} \\ -\dfrac{\alpha_2^2 \cdot E_{total} \cdot \left(SOC_{N-1,4} - SOC_{N-1,3}\right)}{\bar{\omega}_{e_{N-1},h_{1,N-1}} \cdot \beta_1^{h_{1,N-1}} \cdot \Delta t} + \alpha_0^3 + \alpha_1^3 \cdot \bar{\omega}_{e_N,h_{1,N}} \\ +\alpha_2^3 \cdot \left[\dfrac{T_{v_N}}{gr_{c,N}} + \dfrac{E_{total} \cdot \left(SOC_{N,4} - SOC_{N-1,4}\right) + \beta_0^{h_{1,N}} \cdot \Delta t}{\bar{\omega}_{e_N,h_{1,N}} \cdot \beta_1^{h_{1,N}} \cdot \Delta t} \right] \end{cases} , \quad i = 1$$

$$B_{N-1,i}{}' = \begin{cases} \dfrac{\alpha_2^3 \cdot E_{total} \cdot SOC_{N-1,3}}{\bar{\omega}_{e_{N-1},h_{1,N-1}} \cdot \beta_1^{h_{1,N-1}} \cdot \Delta t} \\ -\dfrac{\alpha_2^2 \cdot E_{total} \cdot \left(SOC_{N-1,4} - SOC_{N-1,3}\right)}{\bar{\omega}_{e_{N-1},h_{1,N-1}} \cdot \beta_1^{h_{1,N-1}} \cdot \Delta t} + \alpha_0^3 + \alpha_1^3 \cdot \bar{\omega}_{e_N,h_{1,N}} \\ +\alpha_2^3 \cdot \left[\dfrac{T_{v_N}}{gr_{c,N}} + \dfrac{E_{total} \cdot \left(SOC_{N,4} - SOC_{N-1,4}\right) + \beta_0^{h_{1,N}} \cdot \Delta t}{\bar{\omega}_{e_N,h_{1,N}} \cdot \beta_1^{h_{1,N}} \cdot \Delta t} \right] \end{cases} , \quad i = 2$$

$$B_{N-1,i}{}' = \begin{cases} \dfrac{\alpha_2^2 \cdot E_{total} \cdot SOC_{N-1,4}}{\bar{\omega}_{e_{N-1},h_{1,N-1}} \cdot \beta_1^{h_{1,N-1}} \cdot \Delta t} + \alpha_0^3 + \alpha_1^3 \cdot \bar{\omega}_{e_N,h_{1,N}} \\ +\alpha_2^3 \cdot \left[\dfrac{T_{v_N}}{gr_{c,N}} + \dfrac{E_{total} \cdot \left(SOC_{N,4} - SOC_{N-1,4}\right) + \beta_0^{h_{1,N}} \cdot \Delta t}{\bar{\omega}_{e_N,h_{1,N}} \cdot \beta_1^{h_{1,N}} \cdot \Delta t} \right] \end{cases} , \quad i = 3$$

$$B_{N-1,i}{}' = \begin{cases} \alpha_0^3 \\ +\alpha_1^3 \cdot \bar{\omega}_{e_N,h_{1,N}} + \alpha_2^3 \cdot \left[\dfrac{T_{v_N}}{gr_{c,N}} + \dfrac{E_{total} \cdot SOC_{N,4} + \beta_0^{h_{1,N}} \cdot \Delta t}{\bar{\omega}_{e_N,h_{1,N}} \cdot \beta_1^{h_{1,N}} \cdot \Delta t} \right] \end{cases} , \quad i = 4$$

$$B_{N-1,i}{}' = \begin{cases} \alpha_0^2 \\ +\alpha_1^2 \cdot \bar{\omega}_{e_N,h_{1,N}} + \alpha_2^2 \cdot \left[\dfrac{T_{v_N}}{gr_{c,N}} + \dfrac{E_{total} \cdot SOC_{N,4} + \beta_0^{h_{1,N}} \cdot \Delta t}{\bar{\omega}_{e_N,h_{1,N}} \cdot \beta_1^{h_{1,N}} \cdot \Delta t} \right] \end{cases} , \quad i = 5$$

$$B_{N-1,i}{}' = \begin{cases} \alpha_0^1 \\ +\alpha_1^1 \cdot \bar{\omega}_{e_N,h_{1,N}} + \alpha_2^1 \cdot \left[\dfrac{T_{v_N}}{gr_{c,N}} + \dfrac{E_{total} \cdot SOC_{N,} + \beta_0^{h_{1,N}} \cdot \Delta t}{\bar{\omega}_{e_N,h_{1,N}} \cdot \beta_1^{h_{1,N}} \cdot \Delta t} \right] \end{cases} , \quad i = 6$$

(5.16)

$$u_{N-1,i}{}' = \begin{bmatrix} u^1_{N-1,i}{}' \\ u^2_{N-1,i}{}' \end{bmatrix} = \begin{bmatrix} T_{m_{N-1}} \\ gr_{c,N-1} \end{bmatrix}$$

$$u_{N-1,i}{}' = C_{N-1}{}' \cdot \theta + D_{N-1}{}'$$

$$= \begin{bmatrix} c_{N-1,1} & c_{N-1,2} & c_{N-1,3} & c_{N-1,4} \\ c_{N-1,5} & c_{N-1,6} & c_{N-1,7} & c_{N-1,8} \end{bmatrix} \begin{bmatrix} u^1_{N-1} \\ u^2_{N-1} \\ x^1_{N-1} \\ x^2_{N-1} \end{bmatrix} + \begin{bmatrix} d_{N-1,1} \\ d_{N-1,2} \end{bmatrix} \qquad (5.17)$$

$i \in \{1,2,3\}$: control region for stage N-1

$j \in \{1,2,3\}$: soc region for stage N

$$C_{N-1,i}{}' = \begin{bmatrix} c^1_{N-1,i} & c^2_{N-1,i} & c^3_{N-1,i} & c^4_{N-1,i} \\ c^5_{N-1,i} & c^6_{N-1,i} & c^7_{N-1,i} & c^8_{N-1,i} \end{bmatrix}$$

$$c^1_{N-1,i} = 0, \quad c^2_{N-1,i} = 0$$

$$c^4_{N-1,i} = 0$$

$$c^5_{N-1,i} = 0, \quad c^6_{N-1,i} = 0$$

$$c^7_{N-1,i} = 0, \quad c^8_{N-1,i} = 0$$

$$c^3_{N-1,i} = \begin{cases} 0 & , \quad i = 1 \\ \dfrac{T_{e,3} - T_{e,4}}{SOC_{N-1,2} - SOC_{N-1,3}} & , \quad i = 2 \end{cases} \qquad (5.18)$$

$$c^3_{N-1,i} = \begin{cases} 0 & , \quad i = 3 \\ \dfrac{T_{e,3} - T_{e,4}}{SOC_{N-1,2} - SOC_{N-1,3}} & , \quad i = 4 \end{cases}$$

$$c^3_{N-1,i} = \begin{cases} \dfrac{T_{e,2} - T_{e,3}}{SOC_{N-1,5} - SOC_{N-1,6}} & , \quad i = 5 \\ \dfrac{T_{e,1} - T_{e,2}}{SOC_{N-1,6} - SOC_{N-1,7}} & , \quad i = 6 \end{cases}$$

$$D_{N-1,i}{}' = \begin{bmatrix} d^1_{N-1,i} \\ d^2_{N-1,i} \end{bmatrix} \qquad (5.19)$$

$$d^2_{N-1,i} = gr_{opt}, \left\{ f_{N-1}\left(\omega_v, T_v, gr_{opt}\right)|_{\omega_v, T_v, \Delta soc} \Rightarrow \text{minimum} \right\}$$

$$d_{N-1,i}^{1}=\begin{cases}\dfrac{T_{v_{N-1}}}{gr_{c,N-1}}-T_{e,4} & , \quad i=1\\ -\dfrac{T_{e,3}-T_{e,4}}{SOC_{N-1,2}-SOC_{N-1,3}}\cdot SOC_{N-1,2}+\dfrac{T_{v_{N-1}}}{gr_{c,N-1}}-T_{e,4} & , \quad i=2\end{cases}$$

$$d_{N-1,i}^{1}=\begin{cases}\dfrac{T_{v_{N-1}}}{gr_{c,N-1}}-T_{e,3} & , \quad i=3\\ -\dfrac{T_{e,3}-T_{e,4}}{SOC_{N-1,2}-SOC_{N-1,3}}\cdot SOC_{N-1,5}+\dfrac{T_{v_{N-1}}}{gr_{c,N-1}}-T_{e,3} & , \quad i=4\end{cases}$$

$$d_{N-1,i}^{1}=\begin{cases}-\dfrac{T_{e,2}-T_{e,3}}{SOC_{N-1,5}-SOC_{N-1,6}}\cdot SOC_{N-1,5}+\dfrac{T_{v_{N-1}}}{gr_{c,N-1}}-T_{e,3} & , \quad i=5\\ -\dfrac{T_{e,1}-T_{e,2}}{SOC_{N-1,6}-SOC_{N-1,7}}\cdot SOC_{N-1,6}+\dfrac{T_{v_{N-1}}}{gr_{c,N-1}}-T_{e,2} & , \quad i=6\end{cases}$$

$$\Delta SOC_{N-1,4:5}=\frac{V_{N,3}-\dfrac{V_{N,2}-V_{N,3}}{SOC_{N,2}-SOC_{N,3}}\cdot SOC_{N,3}}{-\dfrac{\alpha_2^3\cdot\cdot E_{total}}{\beta_1^{h_{1,N-1}}\cdot\bar{\omega}_{e_{N-1},h_{1,N-1}}\cdot\Delta t}-\dfrac{V_{N,2}-V_{N,3}}{SOC_{N,2}-SOC_{N,3}}} \tag{5.20}$$

All the above expressions of cost-to-go and optimal controls are valid within the corresponding region. Therefore, it is also important to identify the feasible regions of the solution.

The feasible regions at stage *i=N* and *i=N-1* are expressed in Eqs. (5.21) and (5.22), respectively. The cost-to-go and the corresponding feasible region at stage *i=N*, *i=N-1* and *i=1* are shown in Figure 5.10 – Figure 5.12, respectively.

$$
\begin{aligned}
&SOC_N \in \left[SOC_{N,1}, SOC_{N,4} \right] \\
&SOC_{N,1} = SOC_{desired} + \frac{\Delta t}{E_{total}} \cdot \left[\left(\frac{T_v}{gr_{c,N}} - T_{e,4} \right) \cdot \bar{\omega}_{e,h_{1,N}} \cdot \beta_1^{h_{1,N}} + \beta_0^{h_{1,N}} \right] \\
&SOC_{N,2} = SOC_{desired} + \frac{\Delta t}{E_{total}} \cdot \left[\left(\frac{T_v}{gr_{c,N}} - T_{e,3} \right) \cdot \bar{\omega}_{e,h_{1,N}} \cdot \beta_1^{h_{1,N}} + \beta_0^{h_{1,N}} \right] \\
&SOC_{N,3} = SOC_{desired} + \frac{\Delta t}{E_{total}} \cdot \left[\left(\frac{T_v}{gr_{c,N}} - T_{e,2} \right) \cdot \bar{\omega}_{e,h_{1,N}} \cdot \beta_1^{h_{1,N}} + \beta_0^{h_{1,N}} \right] \\
&SOC_{N,4} = SOC_{desired} + \frac{\Delta t}{E_{total}} \cdot \left[\left(\frac{T_v}{gr_{c,N}} - T_{e,1} \right) \cdot \bar{\omega}_{e,h_{1,N}} \cdot \beta_1^{h_{1,N}} + \beta_0^{h_{1,N}} \right]
\end{aligned}
\tag{5.21}
$$

$$
\begin{aligned}
&SOC_{N-1} \in \left[SOC_{N-1,1}, SOC_{N-1,7} \right] \\
&SOC_{N-1,1} = SOC_{N-1,2} + \frac{\Delta t}{E_{total}} \cdot \left[\left(\frac{T_v}{gr_{c,N-1}} - \left(T_{e,4} - T_{e,3} \right) \right) \cdot \bar{\omega}_{e,h_{1,N-1}} \cdot \beta_1^{h_{1,N-1}} + \beta_0^{h_{1,N-1}} \right] \\
&SOC_{N-1,2} = SOC_{N-1,3} + \frac{\Delta t}{E_{total}} \cdot \left[\left(\frac{T_v}{gr_{c,N-1}} - \left(T_{e,4} - T_{e,3} \right) \right) \cdot \bar{\omega}_{e,h_{1,N-1}} \cdot \beta_1^{h_{1,N-1}} + \beta_0^{h_{1,N-1}} \right] \\
&SOC_{N-1,3} = SOC_{N-1,5} - \left(SOC_{N,4} - SOC_{N,2} \right) \\
&SOC_{N-1,4} = SOC_{N-1,5} - \Delta SOC_{N-1,4:5} \\
&SOC_{N-1,5} = SOC_{N,4} + \frac{\Delta t}{E_{total}} \cdot \left[\left(\frac{T_v}{gr_{c,N-1}} - T_{e,3} \right) \cdot \bar{\omega}_{e,h_{1,N-1}} \cdot \beta_1^{h_{1,N-1}} + \beta_0^{h_{1,N-1}} \right] \\
&SOC_{N-1,6} = SOC_{N,4} + \frac{\Delta t}{E_{total}} \cdot \left[\left(\frac{T_v}{gr_{c,N-1}} - T_{e,2} \right) \cdot \bar{\omega}_{e,h_{1,N-1}} \cdot \beta_1^{h_{1,N-1}} + \beta_0^{h_{1,N-1}} \right] \\
&SOC_{N-1,7} = SOC_{N,4} + \frac{\Delta t}{E_{total}} \cdot \left[\left(\frac{T_v}{gr_{c,N-1}} - T_{e,1} \right) \cdot \bar{\omega}_{e,h_{1,N-1}} \cdot \beta_1^{h_{1,N-1}} + \beta_0^{h_{1,N-1}} \right]
\end{aligned}
\tag{5.22}
$$

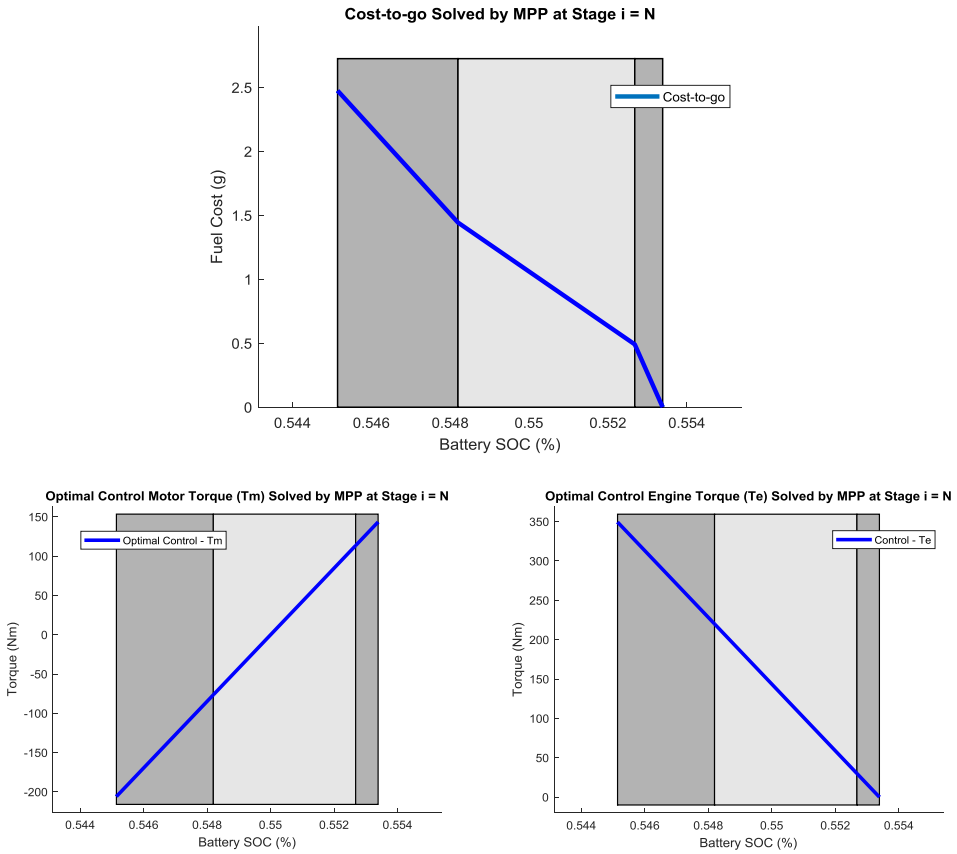

Figure 5.10 Map of critical regions [Eq. (5.21)] to solve Eq. (5.8) with stage $i=N$

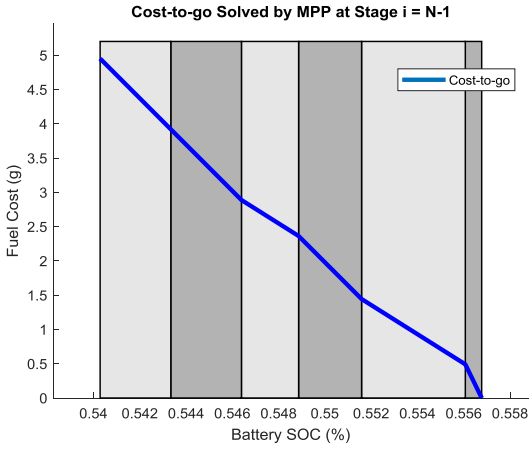

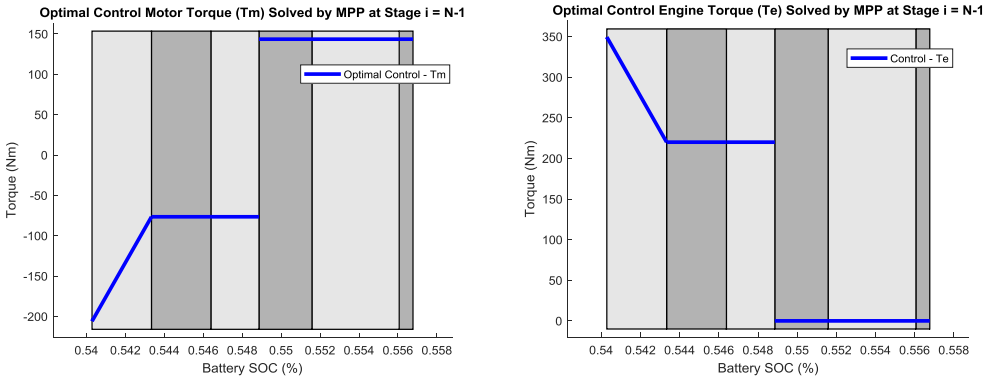

Figure 5.11 Map of critical regions [Eq. (5.22)] to solve Eq. (5.13) with stage *i=N-1*

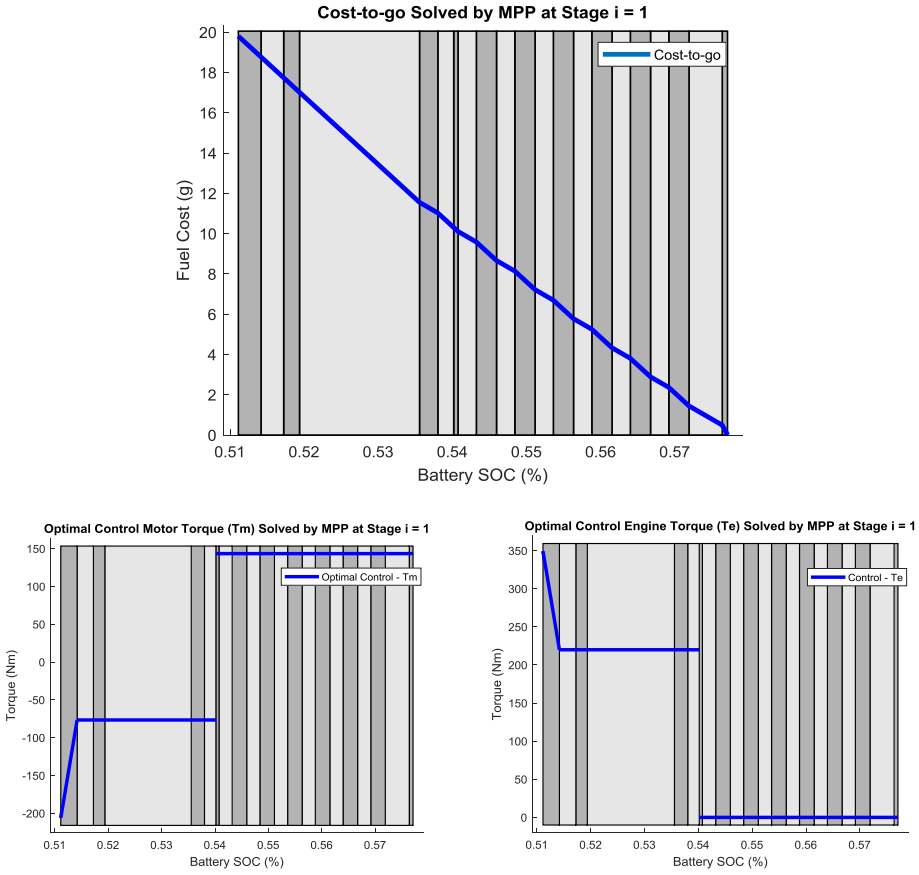

Figure 5.12 Map of critical regions at stage *i=1*

Using the same approach, at stage *k* of the sub-optimization problem, the optimal cost-to-go and optimal control are obtained in below.

$$
\begin{aligned}
&V_{k,i}\left(\theta\right) = A_{k,i}\cdot\theta + B_{k,i}\\
&u_{k,i} = C_{k,i}\cdot\theta + D_{k,i}\\
&\theta = \begin{bmatrix} T_{m_k} & gr_{c,k} & soc & gr_{s,k} \end{bmatrix}'\\
&u_{k,i} = \begin{bmatrix} u_{k,i}^{1\ '} \\ u_{k,i}^{2\ '} \end{bmatrix} = \begin{bmatrix} T_{m_k} \\ gr_{c,k} \end{bmatrix}\\
&i = \min\left| soc - \frac{SOC_{k,i} + SOC_{k,i+1}}{2} \right|\\
&i \in \left\{1,2,...,M\right\}: \text{SOC region point}\\
&h_1 = \min\left|\bar{\omega}_{e_k,h} - \omega_{v_k}\cdot gr_{c,k}\right|\\
&h_1 \in \left\{1,...,20\right\}, \text{engine speed segment}\\
&h_2 = \min\left|\bar{T}_{e,h_2} - T_e\right| = \min\left|\bar{T}_{e,h_2} - \frac{T_{v_k}}{gr_{c,k}}\right|\\
&h_2 \in \left\{1,2,3\right\}: \text{torque segment}\\
&M: \text{number of } SOC_{k,range}
\end{aligned}
\tag{5.23}
$$

$$
\begin{aligned}
&A_{k,i}{}' = \begin{bmatrix} a_{k,i}^1 & a_{k,i}^2 & a_{k,i}^3 & a_{k,i}^4 \end{bmatrix}\\
&a_{k,i}^1 = 0\\
&a_{k,i}^2 = 0\\
&a_{k,i}^3 = \frac{V_{k,i} - V_{k,i+1}}{SOC_{k,i} - SOC_{k,i+1}}\\
&a_{k,i}^4 = 0
\end{aligned}
\tag{5.24}
$$

$$
B_{k,i}{}' = -\frac{V_{k,i} - V_{k,i+1}}{SOC_{k,i} - SOC_{k,i+1}}\cdot SOC_{k,i} + V_{k,i} \tag{5.25}
$$

$$
\begin{aligned}
&C_{k,i}{}' = \begin{bmatrix} c_{k,i}^1 & c_{k,i}^2 & c_{k,i}^3 & c_{k,i}^4 \\ c_{k,i}^5 & c_{k,i}^6 & c_{k,i}^7 & c_{k,i}^8 \end{bmatrix} \\
&c_{k,i}^1 = 0, \quad c_{k,i}^2 = 0 \\
&c_{k,i}^3 = \left(1 + \frac{SOC_{k,i+1+J_{i+1}} - SOC_{k,i+J_i}}{SOC_{k,i} - SOC_{k,i+1}}\right) \frac{E_{total}}{\beta_1^{h_1} \cdot \bar{\omega}_{e_k,h_1} \cdot \Delta t} \\
&c_{k,i}^4 = 0 \\
&c_{k,i}^5 = 0, \quad c_{k,i}^6 = 0 \\
&c_{k,i}^7 = 0, \quad c_{k,i}^8 = 0
\end{aligned}
\tag{5.26}
$$

$$
\begin{aligned}
&D_{k,i}{}' = \begin{bmatrix} d_{k,i}^1 \\ d_{k,i}^2 \end{bmatrix} \\
&d_{k,i}^1 = -\left(1 + \frac{SOC_{k,i+1+J_{i+1}} - SOC_{k,i+J_i}}{SOC_{k,i} - SOC_{k,i+1}}\right) \frac{E_{total} \cdot SOC_{k,i}}{\beta_1^{h_1} \cdot \bar{\omega}_{e_k,h_1} \cdot \Delta t} \\
&\qquad + \frac{\left(SOC_{k,i} - SOC_{k,i+J_i}\right) \cdot E_{total} - \beta_0^{h_1} \cdot \Delta t}{\beta_1^{h_1} \cdot \bar{\omega}_{e_k,h_1} \cdot \Delta t} \\
&d_{k,i}^2 = gr_{opt}, \left\{ f_{k-1}\left(\omega_{v_k}, T_{v_k}, gr_{opt}\right)\big|_{\omega_{v_k}, T_{v_k}, \Delta soc} \Rightarrow \text{minimum} \right\}
\end{aligned}
\tag{5.27}
$$

$$
\begin{aligned}
&V_{k,i} = \min\left[v_i, ..., v_{i+M}\right] \\
&v_j = V_{k+1,I}\left(soc_i\right) + \alpha_0^{h_1,h_2} + \alpha_1^{h_1,h_2} \cdot \bar{\omega}_{e_k,h_1} \\
&\qquad + \alpha_2^{h_1,h_2} \cdot \left(\frac{T_{v_k}}{gr_{c,k}} + \frac{\beta_0^{h_1}}{\beta_1^{h_1} \cdot \bar{\omega}_{e_k,h_1}}\right) - \alpha_2^{h_1,h_2} \cdot \frac{E_{total}}{\beta_1^{h_1} \cdot \bar{\omega}_{e_k,h_1}} \cdot \left(soc_i - soc_j\right) \\
&soc_{i+M} = soc_i + \Delta SOC_{k,4} \\
&j \in \left\{i, ..., i+M\right\} \\
&soc_j \in \left\{soc_i, ..., soc_{i+M}\right\} \\
&soc_i \in SOC_{k,range} \\
&J_i : \text{index of } V_{k,i} \text{ for the minimum} \\
&I = \min\left| soc_i - \frac{SOC_{k+1,I} + SOC_{k+1,I+1}}{2} \right|
\end{aligned}
\tag{5.28}
$$

$$
\begin{aligned}
SOC_{k,range} = &\left\{SOC_{k+1,range} + \Delta SOC_{k,1}\right\} \cup \left\{SOC_{k+1,range} + \Delta SOC_{k,2}\right\} \\
&\cup \left\{SOC_{k+1,range} + \Delta SOC_{k,3}\right\} \cup \left\{SOC_{k+1,range} + \Delta SOC_{k,4}\right\}
\end{aligned}
\tag{5.29}
$$

$$
\begin{aligned}
\Delta SOC_{k,1} &= \frac{\Delta t}{E_{total}} \cdot \left[\left(\frac{T_{v_k}}{gr_{c,k}} - T_{e,4} \right) \cdot \bar{\omega}_{e_k,h_1} \cdot \beta_1^{h_1} + \beta_0^{h_1} \right] \\
\Delta SOC_{k,2} &= \frac{\Delta t}{E_{total}} \cdot \left[\left(\frac{T_{v_k}}{gr_{c,k}} - T_{e,3} \right) \cdot \bar{\omega}_{e_k,h_1} \cdot \beta_1^{h_1} + \beta_0^{h_1} \right] \\
\Delta SOC_{k,3} &= \frac{\Delta t}{E_{total}} \cdot \left[\left(\frac{T_{v_k}}{gr_{c,k}} - T_{e,2} \right) \cdot \bar{\omega}_{e_k,h_1} \cdot \beta_1^{h_1} + \beta_0^{h_1} \right] \\
\Delta SOC_{k,4} &= \frac{\Delta t}{E_{total}} \cdot \left[\left(\frac{T_{v_k}}{gr_{c,k}} - T_{e,1} \right) \cdot \bar{\omega}_{e_k,h_1} \cdot \beta_1^{h_1} + \beta_0^{h_1} \right]
\end{aligned}
\tag{5.30}
$$

Note that the solution in Eqs. (5.23) – (5.30) is a sub-problem solution of Eq. (5.7), with decision variables, and constraints, pertaining only to stage *k*. Bellman [49] demonstrated that, by recursively obtaining the solution in Eqs. (5.23) – (5.30) for $i = N, \ldots, k, \ldots, 1$, the global optimal solution of Eq. (5.7) is obtained.

5.2.2 Algorithm

The steps in the dynamic programming algorithm of mixed-integer linear problems by multi-parametric programming are summarized in the following table.

Table 5.1 Algorithm Using Multi-Parametric Programming

Step	Process
1	Parameterize the original problem into Eq. (5.7).
2	Formulate the dynamic programming recursion in Eq. (5.8) as a multi-parametric mixed-integer linear problem in the form of Eq. (5.13).
3	Solve stage N of the problem to Eq. (5.13) and obtain the solution in Eq. (5.10).
4	for i=(N-1):1
5	Solve stage i of the problem in Eq. (5.13) and obtain the solution in Eq. (5.15):
6	a. Calculate the new SOC range (SOC region critical points) from previous cost-to-go and current control
7	b. Calculate the cost of each SOC region critical point
8	c. Minimize the cost at each point

9		d. Find and add crossing-points not included in the SOC region critical points
10		Obtain the boundaries of feasible regions for the cost-to-go and optimal controls.
11	end	
12	return	
	List of stage solutions and corresponding maps of critical regions	

It should be noted that the MPP algorithm obtains an analytical solution of Eq. (5.7), whereas the DP computes the numerical solution to the problem.

5.3 Use of MPP to Solve Relaxed Optimization for Hybrid Vehicles

5.3.1 Linearization of Relaxed Optimization

The relaxed optimization of the parametrized parallel HEV problem is shown in Eq. (5.31), where vehicle speed v_t and vehicle range s_t are added to the optimization problem. The vehicle resistance torque is a quadratic function of the vehicle speed.

$$
\begin{aligned}
&\min \quad \sum_{t=1}^{N} f(t) \\
&f(t) = \left(\alpha_0^{h_1,h_2} + \alpha_1^{h_1,h_2} \cdot \omega_e(t) + \alpha_2^{h_1,h_2} \cdot T_e(t)\right) \\
&\omega_e(t) = \omega_m(t) = \omega_e\,|_{h_1,h_2} \\
&\omega_e\,|_{h_1,h_2} = \omega_v(t) \cdot gr_c \in \left\{\omega_e\,|_{h_1,h_2}\right\} \\
&T_m(t) = \frac{T_v(t)}{gr_c} - T_e(t) \\
&P_m(t) = \omega_m(t) \cdot T_m(t) \\
&\Delta SOC(t) = \frac{1}{E_{total}} \cdot \left(\beta_1^{h_1} \cdot P_m(t) + \beta_0^{h_1}\right) \\
&h_1 = \min\left|\bar{\omega}_{e,h_1} - \omega_v(t) \cdot gr_c\right|, h_1 \in \{1,2,...,20\} : \text{engine speed segment} \\
&h_2 = \min\left|\bar{T}_{e,h_2} - T_e\right| = \min\left|\bar{T}_{e,h_2} - \frac{T_v}{gr_c}\right|, h_2 \in \{1,2,3\} : \text{torque segment} \\
&v_t = \omega_v(t) \cdot \frac{R_{tire}}{FD} \\
&s_t = \sum_{i=1}^{t} v_t \\
&T_v(t) = \left(mg\mu \cdot \cos\theta + mg \cdot \sin\theta + \frac{1}{2}\rho A C_d \cdot v_t^2 + m \cdot a_t\right) \cdot \frac{R_{tire}}{FD} \\
&a_t = \frac{v_{t+1} - v_t}{\Delta t} \\
&\underline{v}_t \le v_t \le \bar{v}_t, \forall t \\
&\underline{s}_t \le s_t \le \bar{s}_t, \forall t \\
&\underline{x} \le x_t \le \bar{x}, \forall t \\
&\underline{u} \le u_t \le \bar{u}, \forall t
\end{aligned}
\tag{5.31}
$$

The parametric programming problem in Eq. (5.31) is simplified and converted to a piece-wise mixed-integer linear problems by linearizing T_v in the proximity of the original speed $v_{t,original}$ at each stage as a linear function of Δv by neglecting the 2nd order term of Δv, as shown in Eq. (5.32). The adjusted vehicle torque T'_v can then be expressed in Eq. (5.33) in terms of speed difference Δv_t. The parametrized relaxed optimization with linearization is shown in Eq. (5.34).

$$
T_v'(t) = T_v(t) + \frac{\rho A C_d \cdot R_{tire} \cdot v_{t,original}}{FD} \cdot \Delta v_t + mR_{tire} \cdot \frac{\Delta v_t + \Delta v_{t+1}}{FD \cdot \Delta t} \tag{5.32}
$$

$$T_v^{'}(t) = T_v(t) + \left(\frac{\rho A C_d \cdot R_{tire} \cdot v_{t,original}}{FD} + \frac{m R_{tire}}{FD \cdot \Delta t} \right) \cdot \Delta v_t + \frac{m R_{tire}}{FD \cdot \Delta t} \cdot \Delta v_{t+1} \tag{5.33}$$

$$\begin{aligned}
&\min \quad \sum_{t=1}^{N} f(t) \\
&f(t) = \left(\alpha_0^{h_1,h_2} + \alpha_1^{h_1,h_2} \cdot \omega_e(t) + \alpha_2^{h_1,h_2} \cdot T_e(t) \right) \\
&\omega_e(t) = \omega_m(t) = \omega_e|_{h_1,h_2} \\
&\omega_e|_{h_1,h_2} = \omega_v(t) \cdot gr_c \in \left\{ \omega_e|_{h_1,h_2} \right\} \\
&T_m(t) = \frac{T_v^{'}(t)}{gr} - T_e(t) \\
&P_m(t) = \omega_m(t) \cdot T_m(t) \\
&\Delta SOC(t) = \frac{1}{E_{total}} \cdot \left(\beta_1^{h_1} \cdot P_m(t) + \beta_0^{h_1} \right) \\
&h_1 = \min \left| \bar{\omega}_{e,h_1} - \left(\omega_{v_k} + \frac{\Delta v_k}{R_{tire}} \cdot FD \right) \cdot gr_c \right|, h_1 \in \{1,2,...,20\} : \text{engine speed segment} \\
&h_2 = \min \left| \bar{T}_{e,h_2} - \frac{T_v + \Delta T_v}{gr_c} \right|, h_2 \in \{1,2,3\} : \text{torque segment} \\
&v_t = \omega_v(t) \cdot \frac{R_{tire}}{FD} \\
&s_t = \sum_{i=1}^{t} v_i \\
&T_v^{'}(t) = T_v(t) + \left(\frac{\rho A C_d \cdot R_{tire}}{FD} \cdot v_t + \frac{m R_{tire}}{FD \cdot \Delta t} \right) \cdot \Delta v_t + \frac{m R_{tire}}{FD \cdot \Delta t} \cdot \Delta v_{t+1} \\
&\underline{v}_t \le v_t \le \bar{v}_t, \forall t \\
&\underline{s}_t \le s_t \le \bar{s}_t, \forall t \\
&\underline{x} \le x_t \le \bar{x}, \forall t \\
&\underline{u} \le u_t \le \bar{u}, \forall t
\end{aligned} \tag{5.34}$$

5.3.2 Solving the Relaxed Optimization

With the additional control and state, the cost-to-go function solved by the MPP becomes a two-dimensional function (assuming just using 1 fixed transmission gear for simplification). Following the same approach as that found in Section 5.2, the sub-problem to be solved through the MPP is shown in Eq. (5.35), where the decision vector X_k=[u^1_k, u^2_k, u^3_k, x^1_k, x^2_k, x^3_k] includes both the control and state vector, u^3_k is the control of vehicle

speed and x^3_k is the vehicle speed. In this case of HEV relaxed optimization, the decision vector includes MG2 torque command T_{mg2}, gear ratio command gr (for next time-step), demanded change of vehicle speed Δv (for next time-step), current SOC state soc, current gear ratio state gr, and current change of vehicle speed Δv. Assuming the time for gear-shifting is neglected, the states remained in the cost-to-go are vehicle speed and battery SOC. The cost-to-go and the optimal control in each time step k are expressed in Eqs. (5.36) – (5.38).

$$
\begin{aligned}
&V_k = \min \quad f_k\left(u_k^1, u_k^2, u_k^3, x_k^1, x_k^2, x_k^3, \theta_k\right) + V_{k+1,j}\left(\theta_{k+1}\right)\big|_{x_k^1, x_k^3} \\
&f_k\left(\omega_{e_k}, T_{e_k}\right) = \left(\alpha_0^{h_{1,k},h_{2,k}} + \alpha_1^{h_{1,k},h_{2,k}} \cdot \omega_{e_k} + \alpha_2^{h_{1,k},h_{2,k}} \cdot T_{e_k}\right) \\
&V_{k+1,i}\left(\theta\right) = \begin{bmatrix} 0 & 0 & 0 & a_{k+1,i}^4 & 0 & a_{k+1,i}^6 \end{bmatrix} \begin{bmatrix} T_{m_{k+1}} \\ gr_{c,k+1} \\ \Delta v_{k+2} \\ SOC_{k+1} \\ gr_{s,k+1} \\ \Delta v_{k+1} \end{bmatrix} \\
&\qquad\qquad + B_{k+1,i}{}' \\
&\omega_{e_k} = \omega_{m_k} = \bar{\omega}_{e_k,h_{1,k}} \\
&\Delta T_{v_k} = \left(\frac{\rho A C_d \cdot R_{tire} \cdot v_{t,original}}{FD} + \frac{mR_{tire}}{FD \cdot \Delta t}\right) \cdot \Delta v_t + \frac{mR_{tire}}{FD \cdot \Delta t} \cdot \Delta v_{t+1} \\
&T_{m_k} = \frac{T_{v_k} + \Delta T_{v_k}}{gr_k} - T_{e_k} \\
&P_{m_k} = \omega_{m_k} \cdot T_{m_k} \\
&\Delta SOC_k = \frac{1}{E_{total}} \cdot \left(\beta_1^{h_{1,k}} \cdot P_{m_k} + \beta_0^{h_{1,k}}\right) \\
&\Delta SOC_k = \left(SOC_k - SOC_{k+1}\right) / \Delta t \\
&i \in SOC_{k+1,range} : \text{battery SOC region} \\
&h_{1,k} = \min \left| \bar{\omega}_{e_k,h_{1,k}} - \left(\omega_{v_k} + \frac{\Delta v_k}{R_{tire}} \cdot FD\right) \cdot gr_{c,k} \right| \\
&h_{1,k} \in \{1, ..., 20\} : \text{engine segment} \\
&h_{2,k} = \min \left| \bar{T}_{e_k,h_{2,k}} - \frac{T_{v_k} + \Delta T_{v_k}}{gr_{c,k}} \right| \\
&h_{2,k} \in \{1, 2, 3\} : \text{torque segment}
\end{aligned}
\tag{5.35}
$$

$$
\begin{aligned}
&V_{k,i}\left(\theta\right) = A_{k,i}\cdot\theta + B_{k,i}\\
&u_{k,i} = C_{k,i}\cdot\theta + D_{k,i}\\
&\theta = \begin{bmatrix} T_{m_k} & gr_{c,k} & \Delta v_{k+1} & SOC_k & gr_{s,k} & \Delta v_k \end{bmatrix}'\\
&u_{k,i} = \begin{bmatrix} u_{k,i}^{1\,'} \\ u_{k,i}^{2\,'} \\ u_{k,i}^{3\,'} \end{bmatrix} = \begin{bmatrix} T_{m_k} \\ gr_{c,k} \\ \Delta v_{k+1} \end{bmatrix}\\
&i = \min\left| soc - \frac{SOC_{k,i} + SOC_{k,i+1}}{2} \right|\\
&i \in \left\{1,2,...,M\right\} : \text{SOC region point}\\
&h_{1,k} = \min\left| \bar{\omega}_{e_k,h_{1,k}} - \left(\omega_{v_k} + \frac{\Delta v_k}{R_{tire}}\cdot FD \right)\cdot gr_{c,k} \right|\\
&h_{1,k} \in \left\{1,...,20\right\} : \text{engine segment}\\
&h_{2,k} = \min\left| \bar{T}_{e_k,h_{2,k}} - \frac{T_{v_k} + \Delta T_{v_k}}{gr_{c,k}} \right|\\
&h_{2,k} \in \left\{1,2,3\right\} : \text{torque segment}\\
&M : \text{number of } SOC_{k,range}
\end{aligned}
\tag{5.36}
$$

$$
\begin{aligned}
&A_{k,i}' = \begin{bmatrix} a_{k,i}^1 & a_{k,i}^2 & a_{k,i}^3 & a_{k,i}^4 & a_{k,i}^5 & a_{k,i}^6 \end{bmatrix}\\
&a_{k,i}^1 = 0\\
&a_{k,i}^2 = 0\\
&a_{k,i}^3 = 0\\
&a_{k,i}^4 = \frac{V_{k,i}\left|_{SOC_{k,i};\Delta v_k=0}\right. - V_{k,i+1}\left|_{SOC_{k,i+1};\Delta v_k=0}\right.}{SOC_{k,i} - SOC_{k,i+1}}\\
&a_{k,i}^5 = 0\\
&a_{k,i}^6 = \frac{W_k}{\min\left(\Delta v_k\right) - \max\left(\Delta v_k\right)}
\end{aligned}
\tag{5.37}
$$

$$B_{k,i}{}' = -\frac{V_{k,i}\left|_{SOC_{k,i};\Delta v_t=0}\right. - V_{k,i+1}\left|_{SOC_{k,i+1};\Delta v_t=0}\right.}{SOC_{k,i} - SOC_{k,i+1}} \cdot SOC_{k,i} - \frac{W_k}{\min(\Delta v_k) - \max(\Delta v_k)} \cdot \min(\Delta v_k) + V_{k,i} \tag{5.38}$$

$$C_{k,i}{}' = \begin{bmatrix} c_{k,i}^1 & c_{k,i}^2 & c_{k,i}^3 & c_{k,i}^4 & c_{k,i}^5 & c_{k,i}^6 \\ c_{k,i}^7 & c_{k,i}^8 & c_{k,i}^9 & c_{k,i}^{10} & c_{k,i}^{11} & c_{k,i}^{12} \\ c_{k,i}^{13} & c_{k,i}^{14} & c_{k,i}^{15} & c_{k,i}^{16} & c_{k,i}^{17} & c_{k,i}^{18} \end{bmatrix}$$

$$c_{k,i}^1 = 0, \quad c_{k,i}^2 = 0,$$

$$c_{k,i}^3 = \frac{mR_{tire}}{gr_{opt} \cdot FD \cdot \Delta t}$$

$$c_{k,i}^4 = \left(1 + \frac{SOC_{k,i+1+J_{i+1}} - SOC_{k,i+J_i}}{SOC_{k,i} - SOC_{k,i+1}}\right) \frac{E_{total}}{\beta_1^{h_{1,k}} \cdot \bar{\omega}_{e_k,h_{1,k}} \cdot \Delta t}$$

$$c_{k,i}^5 = 0$$

$$c_{k,i}^6 = \left(\frac{\rho AC_d \cdot R_{tire} \cdot v_{t,original}}{gr_{opt} \cdot FD} + \frac{mR_{tire}}{gr_{opt} \cdot FD \cdot \Delta t}\right) \tag{5.39}$$

$$c_{k,i}^7 = 0, \quad c_{k,i}^8 = 0, \quad c_{k,i}^9 = 0$$

$$c_{k,i}^{10} = 0, \quad c_{k,i}^{11} = 0, \quad c_{k,i}^{12} = 0$$

$$c_{k,i}^{13} = 0, \quad c_{k,i}^{14} = 0, \quad c_{k,i}^{15} = 0$$

$$c_{k,i}^{16} = 0, \quad c_{k,i}^{17} = 0,$$

$$c_{k,i}^{18} = 1 + \frac{\Delta v_{k,i+1+J_{i+1}} - \Delta v_{k,i+J_i}}{\Delta v_{k,i} - \Delta v_{k,i+1}}$$

$$\left\{\bar{\omega}_{e_k,h_{1,k}} = \frac{v_{t,original} + \Delta v_t}{R_{tire}} \cdot FD \cdot gr_{opt}\right\}$$

$$D_{k,i}{}' = \begin{bmatrix} d_{k,i}^1 \\ d_{k,i}^2 \\ d_{k,i}^3 \end{bmatrix}$$

$$\begin{aligned} d_{k,i}^1 &= -\left(1+\frac{SOC_{k,i+1+J_{i+1}} - SOC_{k,i+J_i}}{SOC_{k,i} - SOC_{k,i+1}}\right)\frac{E_{total}\cdot SOC_{k,i}}{\beta_1^{h_{1,k}}\cdot\bar{\omega}_{e_k,h_{1,k}}\cdot\Delta t} \\ &\quad + \frac{\left(SOC_{k,i} - SOC_{k,i+J_i}\right)\cdot E_{total} - \beta_0^{h_{1,k}}\cdot\Delta t}{\beta_1^{h_{1,k}}\cdot\bar{\omega}_{e_k,h_{1,k}}\cdot\Delta t} \end{aligned} \tag{5.40}$$

$$d_{k,i}^2 = gr_{opt}, \left\{ f_{k-1}\left(\omega_{v_k}, T_{v_k}, gr_{opt}\right)|_{\omega_{v_k},T_{v_k},\Delta soc} \Rightarrow \text{minimum} \right\}$$

$$d_{k,i}^3 = \sup\left(\underline{v}, \inf\left(\left(-\left(1+\frac{\Delta v_{k,i+1+J_{i+1}} - \Delta v_{k,i+J_i}}{\Delta v_{k,i} - \Delta v_{k,i+1}}\right)\Delta v_{k,i} + \Delta v_{k,i} - \Delta v_{k,i+J_i}\right), \bar{v}\right)\right)$$

$$V_{k,i} = \min\left[v_i, ..., v_{i+M}\right]$$

$$\begin{aligned} v_j &= V_{k+1,I}\left(soc_i\right)|_{\Delta v_k=0} + \alpha_0^{h_{1,k},h_{2,k}} + \alpha_1^{h_{1,k},h_{2,k}}\cdot\bar{\omega}_{e_k,h_{1,k}} \\ &\quad + \alpha_2^{h_{1,k},h_{2,k}}\cdot\left(\frac{T_{v_k}}{gr_{c,k}} + \frac{\beta_0^{h_{1,k}}}{\beta_1^{h_{1,k}}\cdot\bar{\omega}_{e_k,h_{1,k}}}\right) - \alpha_2^{h_{1,k},h_{2,k}}\cdot\frac{E_{total}}{\beta_1^{h_{1,k}}\cdot\bar{\omega}_{e_k,h_{1,k}}}\cdot\left(soc_i - soc_j\right) \end{aligned}$$

$$\begin{aligned} &soc_{i+M} = soc_i + \Delta SOC_{k,4} \\ &j \in \left\{i, ..., i+M\right\} \\ &soc_j \in \left\{soc_i, ..., soc_{i+M}\right\} \\ &soc_i \in SOC_{k,range} \end{aligned} \tag{5.41}$$

J_i : index of $V_{k,i}$ for the minimum

$$I = \min\left|soc_i - \frac{SOC_{k+1,I} + SOC_{k+1,I+1}}{2}\right|$$

$$W_k = f_k\left(\bar{\omega}_{e_k,h_{1,k}}, \frac{T_{v_k}}{gr_{c,k}}\right) - f_k\left(\bar{\omega}_{e_k,h_{1,k}}, \frac{T_{v_k}+\Delta T_{v_k}}{gr_{c,k}}\right)$$

$$\begin{aligned} SOC_{k,range} &= \left\{SOC_{k+1,range} + \Delta SOC_{k,1}\right\} \cup \left\{SOC_{k+1,range} + \Delta SOC_{k,2}\right\} \\ &\quad \cup \left\{SOC_{k+1,range} + \Delta SOC_{k,3}\right\} \cup \left\{SOC_{k+1,range} + \Delta SOC_{k,4}\right\} \end{aligned} \tag{5.42}$$

$$
\begin{aligned}
\Delta SOC_{k,1} &= \frac{\Delta t}{E_{total}} \cdot \left[\left(\frac{T_{v_k}}{gr_{c,k}} - T_{e,4} \right) \cdot \bar{\omega}_{e_k,h_{1,k}} \cdot \beta_1^{h_{1,k}} + \beta_0^{h_{1,k}} \right] \\
\Delta SOC_{k,2} &= \frac{\Delta t}{E_{total}} \cdot \left[\left(\frac{T_{v_k}}{gr_{c,k}} - T_{e,3} \right) \cdot \bar{\omega}_{e_k,h_{1,k}} \cdot \beta_1^{h_{1,k}} + \beta_0^{h_{1,k}} \right] \\
\Delta SOC_{k,3} &= \frac{\Delta t}{E_{total}} \cdot \left[\left(\frac{T_{v_k}}{gr_{c,k}} - T_{e,2} \right) \cdot \bar{\omega}_{e_k,h_{1,k}} \cdot \beta_1^{h_{1,k}} + \beta_0^{h_{1,k}} \right] \\
\Delta SOC_{k,4} &= \frac{\Delta t}{E_{total}} \cdot \left[\left(\frac{T_{v_k}}{gr_{c,k}} - T_{e,1} \right) \cdot \bar{\omega}_{e_k,h_{1,k}} \cdot \beta_1^{h_{1,k}} + \beta_0^{h_{1,k}} \right]
\end{aligned}
\tag{5.43}
$$

5.4 Simulation and Analysis of Non-Relaxed Optimization

5.4.1 Comparison between DP and MPP

The DP and MPP are used to solve the non-relaxed problem of the parallel hybrid vehicle in Eq. (5.7). Because the DP has been commonly used to solve similar HEV optimization problems, its result is used for comparison with that of the MPP. The optimized fuel consumption results calculated from both methods are summarized in Table 5.2.

Table 5.2 Fuel Consumption Result Comparison

Solving Method	Fuel Consumption (g)
MPP	12.61
DP	12.59

The results listed in Table 5.2 indicate that the fuel consumption calculated by the two methods are practically the same (0.16% difference). This verifies that the analytical solution by the MPP and the numerical results by the DP converge. In fact, the results from MPP should be the accurate result, whereas that of DP is the approximated numerical result.

To further verify the results of the two methods, two cost-to-go functions obtained from each method are compared. Firstly, the cost-to-go values calculated by $t = N - 2$ to $t = N$ are shown in Figure 5.13. The results show that the two cost-to-go functions overlap

and are considered to be the same. Figure 5.14 is the comparison of results of the 8s cruising short cycle between MPP and DP; it confirms that both cost-to-go results are numerically the same.

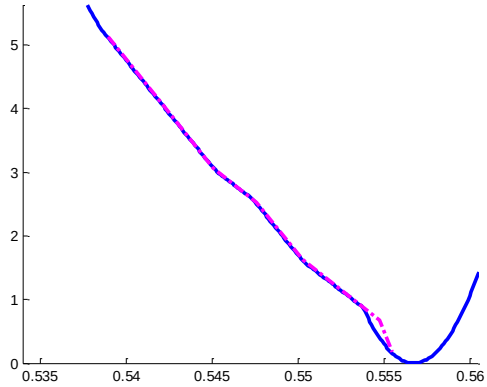

Figure 5.13 Cost-to-go from *t*=*N*-2 to *t*=*N* calculated by DP (in blue) and MPP (in purple)

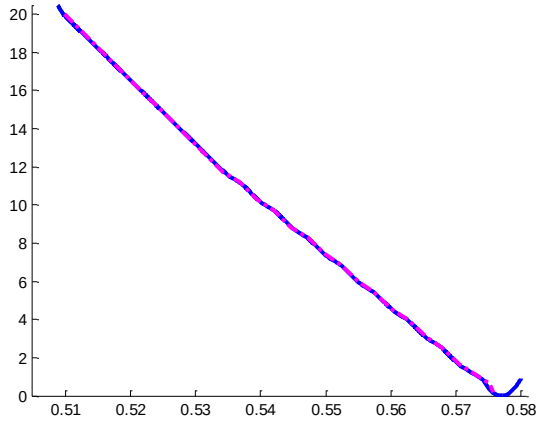

Figure 5.14 Cost-to-go calculated by DP (in blue) and MPP (in purple) for the 8-second cruising cycle

The constant offset between the cost-to-go function obtained with the MPP and calculated by the DP comes from the approximation of DP. In the DP method, a quadratic penalty function on the SOC state is used to constrain the desired state at the end of the cycle. The constant error is then generated because the quadratic function has a smaller value than the linear function in a small region. Therefore, considering this offset, the cost-to-go function obtained using the MPP has the same value calculated by the DP.

5.4.2 Efficiency and Analysis of DP and MPP

The computational costs between the DP and MPP are also compared in terms of computational time in a PC (with an Intel(R) Core(TM) i7-2600 CPU at 3.40GHz), to understand the benefit of the MPP method. The stage computational time, backward optimization computational time, and total computational time are summarized in Table 5.3.

Table 5.3 Computational Time Cost of 8-Second Cruise Cycle Solved by DP and MPP

		DP	MPP
Step 1	Stage cost, transitional cost transitional cost (horizon)	0.92 s 9.2 s	
Step 2	Stage cost, backward optimization optimization (horizon)	1.2 s 12 s	0.0274 s 0.27 s
All Steps	Total cost	21.2 s	0.27 s

The DP method has to calculate the transitional cost of each control and state grid point at each stage. Each stage computational time is determined by the number of discretization grids and number of states and controls. The computational time for the 1st step is then determined by the stage time and the length of the problem horizon. It is not necessary for the MPP to compute the transitional cost nor state/control discretization; hence, it does not have any cost in the 1st step.

In the 2nd step, the DP method solves the sub-optimization problem backward from the end of the problem horizon to the initial state of each gridded state at every stage. The computational time for the 2nd step is determined by the number of discretization grids, number of states, and the length of problem horizon. The MPP analytically solves the parametric sub-problem Eq. (5.13) at each stage. Continuous states are formulated within the analytical solutions; thus, there is no discretization in continuous states. Therefore, the computational complexity only depends on the number of discrete states and the problem horizon length.

The results show that the DP requires significant computational resources because of the curse of dimensionality. The MPP method can solve the problem efficiently because it directly solves a mixed-integer linear optimization problem directly in all continuous

states and controls. The MPP method does not require additional resources to repeat computation because of the continuous-state discretization; thus, the curse of dimensionality of continuous states and controls is avoided.

As a summary of these two methods, DP is a numerical method that can solve many different problems including highly non-linear problems and non-convex problems. However, to better approximate to the correct optimal solution, the discretization of states/controls causes heavy computational load. MPP is an analytical method that can solve problems efficiently and also guarantee the global optimality. To implement this method, it requires the original problem can be approximated well by a piece-wise mixed-integer convex optimization problem. It may not be the best method to solve all the non-linear problems, non-convex problems, or problems with high order dynamics. In this case as shown in this chapter, the HEV optimization problem can be approximated well as a piece-wise mixed-integer linear optimization, thus can be solved using MPP method.

5.5 Simulation Results and Comparison of Relaxed Optimization

The simulation results of the HEV relaxed optimization solved by the MPP and compared to DP results are summarized in Table 5.4. The relaxed optimization of HEV reduces fuel consumption by 4 – 6 % in addition to the optimization of HEV without vehicle speed relaxation, for selected drive cycles within the EPA defined ±2 mph speed bound.

Table 5.4 Simulation Result Comparison of HEV Relaxed Optimization Solved by DP and MPP

	Driving Scenarios	NYCC	UDDS	FTP-75	HWFET
Fuel (g)	DP	56.6	572.3	913.5	1281.1
	MPP	58	586	932	1289
Fuel Consumption Reduction Compared to Non-Relaxed HEV	DP	6.1%	5.7%	5.2%	4.7%
	MPP	3.8%	3.5%	3.2%	4.1%

Result Difference		2.5%	2.4%	2.0%	0.6%

The summary in Table 5.4 shows that the differences are 0.6 – 6%. The differences are caused by the numerical precision of DP and the precision resulting from the simplification of MPP models. The distribution of the powertrain component operating points over the FTP-75 is shown in Figure 5.15. The operating points used by the two methods were found to be comparable.

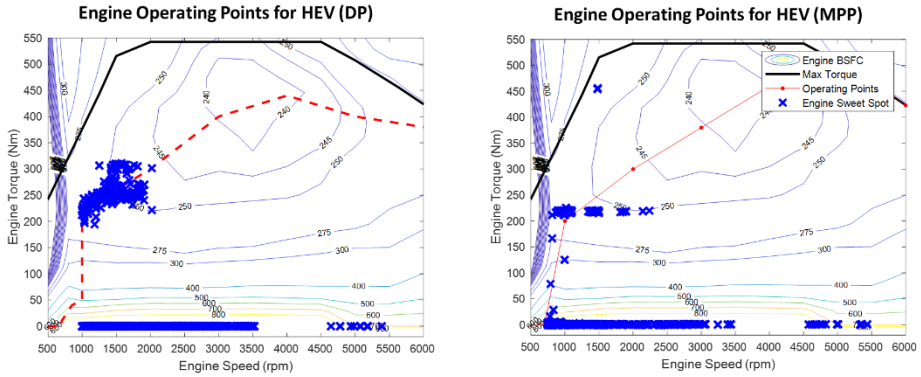

Figure 5.15 Distribution of engine operating points: numerical results (DP) vs analytical results (MPP)

The computation efficiency of the two methods are summarized and compared in Table 5.5. The processing speed of the MPP method is over 100 times faster than that of the DP. This shows the advantage of the MPP method in solving a high-order optimization problem.

Table 5.5 Simulation Computational Cost Comparison between DP and MPP

	Driving Scenarios	NYCC	UDDS	FTP-75	HWFET
Simulation Time	DP	8.2 days	17.8 days	25.2 days	9.5 days
	MPP	2.1 hrs	5.3 hrs	8.5 hrs	3.5 hrs

5.6 Relaxed Optimization of AWD

5.6.1 Deriving Solutions in MPP Formulation

The same methodology outlined earlier in the chapter can be applied to the AWD multi-mode powertrain hybrid powertrain. As stated in Chapter 3, the AWD multi-mode hybrid powertrain has two controls (operating mode and wheel torque split ratio / engine torque) and three states (operating mode, engine speed, and battery SOC). Compared to the HEV parallel dynamics, the foregoing involves one more variable. In addition, one more control (EM1 torque) and one more state (vehicle speed) are involved for the relaxed optimization, respectively. Both of additional control and state are part of the linear HEV system dynamics. Therefore, the MPP method can be applied to solve this system using the same model simplification framework. The simplified dynamics for the relaxed optimization of the AWD multi-mode power-split powertrain hybrid powertrain are shown in Eqs. (5.44) – (5.46).

$$\min \quad \sum_{t=1}^{N} f(t)$$

$$f(t) = \left(\alpha_0^{h_1,h_2} + \alpha_1^{h_1,h_2} \cdot \omega_e(t) + \alpha_2^{h_1,h_2} \cdot T_e(t)\right)$$

$$\dot{\Omega} = A^{-1} \cdot T$$

$$\omega_e|_{h_1,h_2} = \omega_e \in \left\{\omega_e|_{h_1,h_2}\right\}$$

$$P_{bat} = \omega_{em1} \cdot T_{em1} \cdot \eta_{em1}^{k\_em1} + \omega_{em2} \cdot T_{em2} \cdot \eta_{em2}^{k\_em2}$$

$$\Delta SOC(t) = \frac{1}{E_{total}} \cdot \left(\beta_1^{h_1} \cdot P_m(t) + \beta_0^{h_1}\right)$$

$$k\_em1 = \begin{cases} -1 & \omega_{em1} \cdot T_{em1} \geq 0 \\ 1 & \omega_{em1} \cdot T_{em1} < 0 \end{cases}$$

$$k\_em2 = \begin{cases} -1 & \omega_{em2} \cdot T_{em2} \geq 0 \\ 1 & \omega_{em2} \cdot T_{em2} < 0 \end{cases} \qquad (5.44)$$

$$v_t = \omega_v(t) \cdot FD$$

$$s_t = \sum_{i=1}^{t} v_i$$

$$T_v^{'}(t) = T_v(t) + \left(\frac{\rho A C_d \cdot R_{tire} \cdot v_t}{FD} + \frac{mR_{tire}}{FD \cdot \Delta t}\right) \cdot \Delta v_t + \frac{mR_{tire}}{FD \cdot \Delta t} \cdot \Delta v_{t+1}$$

$$a_t = \frac{v_{t+1} - v_t}{\Delta t} = \frac{\left(T_F + T_R - T_v - \Delta T_v\right) \cdot FD}{mR_{tire}}$$

$$\underline{v}_t \leq v_t \leq \overline{v}_t, \forall t$$

$$\underline{s}_t \leq s_t \leq \overline{s}_t, \forall t$$

$$\underline{x} \leq x_t \leq \overline{x}, \forall t$$

$$\underline{u} \leq u_t \leq \overline{u}, \forall t$$

$$A = \begin{bmatrix} I_e + I_{c1} & 0 & 0 & 0 & 0 & 0 & R_1 + S_1 & 0 & 0 \\ 0 & I_F + I_{c2} & 0 & 0 & 0 & 0 & 0 & R_2 + S_2 & 0 \\ 0 & 0 & I_R + I_{mg2} + I_{s2} & 0 & 0 & 0 & 0 & -S_2 & 0 \\ 0 & 0 & 0 & I_{mg1} + I_{s1} & 0 & 0 & -S_1 & 0 & 0 \\ 0 & 0 & 0 & 0 & I_{r1} & 0 & -R_1 & 0 & 1 \\ 0 & 0 & 0 & 0 & 0 & I_{r2} & 0 & -R_2 & -1 \\ R_1 + S_1 & 0 & 0 & -S_1 & -R_1 & 0 & 0 & 0 & 0 \\ 0 & R_2 + S_2 & -S_2 & 0 & 0 & -R_2 & 0 & 0 & 0 \\ 0 & 0 & 0 & 0 & 1 & -1 & 0 & 0 & 0 \end{bmatrix} \qquad (5.45)$$

$$T = \begin{bmatrix} T_e & (-T_F) & (-T_R) + T_{mg2} & T_{mg1} & 0 & 0 & 0 & 0 & 0 \end{bmatrix}^T$$

$$\dot{\Omega} = \begin{bmatrix} \dot{\omega}_e & \dot{\omega}_F & \dot{\omega}_R & \dot{\omega}_{mg1} & \dot{\omega}_{r1} & \dot{\omega}_{r2} & F_1 & F_2 & T_{cl1} \end{bmatrix}^T$$

$$D = \begin{bmatrix} R_1 + S_1 & 0 & 0 \\ 0 & R_2 + S_2 & 0 \\ 0 & -S_2 & 0 \\ -S_1 & 0 & 0 \\ -R_1 & 0 & 1 \\ 0 & -R_2 & -1 \end{bmatrix} \tag{5.46}$$

The optimal solution of the relaxed optimization for AWD multi-mode power-split hybrid powertrain in the recursive form are shown in Eqs. (5.47) – (5.55).

$$V_k = \min \quad f_k\left(u_k^1, u_k^2, u_k^3, x_k^1, x_k^2, x_k^3, x_k^4, \theta_k\right) + V_{k+1,j}\left(\theta_{k+1}\right)\big|_{x_k^1, x_k^3, x_k^4}$$

$$f_k = \left(\alpha_0^{h_{1,k},h_{2,k}} + \alpha_1^{h_{1,k},h_{2,k}} \cdot \bar{\omega}_{e_k,h_{1,k}} + \alpha_2^{h_{1,k},h_{2,k}} \cdot T_{e_k}\right)$$

$$V_{k+1,i}\left(\theta\right) = \begin{bmatrix} 0 & 0 & 0 & a_{k+1,i}^4 & 0 & 0 & a_{k+1,i}^3 \end{bmatrix} \begin{bmatrix} T_{m_{2,k+1}} \\ mode_{c,k+1} \\ \Delta v_{k+2} \\ SOC_{k+1} \\ \omega_{e,k+1} \\ mode_{s,k+1} \\ \Delta v_{k+1} \end{bmatrix}$$

$$+ B_{k+1,i}{}'$$

$$\omega_{m_{1,k}} = \bar{\omega}_{m_{1,k},h_{m_{1,k}}}$$

$$\omega_{m_{2,k}} = \bar{\omega}_{m_{2,k},h_{m_{2,k}}}$$

$$T_{e_k} = \left(T_{v_k} + \Delta T_{v_k} - T_{m_{2,k+1}}\right) \cdot \frac{R_1}{R_1 + S_1}, T_{m_{1,k}} = \left(T_{v_k} + \Delta T_{v_k} - T_{m_{2,k+1}}\right) \cdot \frac{S_1}{R_1 + S_1}$$

$$\Delta T_{v_k} = \left(\frac{\rho A C_d \cdot R_{tire} \cdot v_t}{FD} + \frac{mR_{tire}}{FD \cdot \Delta t}\right) \cdot \Delta v_k + \frac{mR_{tire}}{FD \cdot \Delta t} \cdot \Delta v_{k+1}$$

$$P_{m_{1,k}} = \omega_{m_{1,k}} \cdot T_{m_{1,k}} \tag{5.47}$$

$$P_{m_{2,k}} = \omega_{m_{2,k}} \cdot T_{m_{2,k}}$$

$$\Delta SOC_k = \frac{1}{E_{total}} \cdot \left(\beta_1^{h_{1,k}} \cdot \left(P_{m_{1,k}} + P_{m_{2,k}}\right) + \beta_0^{h_{1,k}}\right)$$

$$\Delta SOC_k = \left(SOC_k - SOC_{k+1}\right) / \Delta t$$

$i \in SOC_{k+1,range}$: battery SOC region

$h_{e_{1,k}} = \min\left|\bar{\omega}_{e_k,h_{1,k}} - \omega_{e_k}\right|, h_{e_{1,k}} \in \{1,...,20\}$: engine speed segment

$h_{e_{2,k}} = \min\left|\bar{T}_{e_k,h_{2,k}} - T_{e_k}\right|, h_{e_{2,k}} \in \{1,2,3\}$: torque segment

$$h_{m1_{1,k}} = \min\left|\bar{\omega}_{m_{1,k},h_{m_{1,k}}} - \frac{\left(\omega_{v_{f,k}} \cdot R_2 + \omega_{v_{r,k}} \cdot S_2\right) \cdot \frac{R_1 + S_1}{R_2 + S_2} - \omega_{e_k} \cdot R_1}{S_1}\right|$$

$h_{m1_{1,k}} \in \{1,...,20\}$: motor segment

$h_{m1_{2,k}} = \min\left|\bar{T}_{m_{1,k},h_{2,k}} - T_{m_{1,k}}\right|, h_{m1_{2,k}} \in \{1,2,3\}$: torque segment

$h_{m2_{1,k}} = \min\left|\bar{\omega}_{m_{2,k},h_{m_{1,k}}} - \omega_{v_{r,k}}\right|, h_{m2_{1,k}} \in \{1,...,20\}$: motor speed segment

$h_{m2_{2,k}} = \min\left|\bar{T}_{m_{2,k},h_{2,k}} - T_{m_{2,k}}\right|, h_{m2_{2,k}} \in \{1,2,3\}$: torque segment

$$
\begin{aligned}
&V_{k,i}\left(\theta\right) = A_{k,i}\cdot\theta + B_{k,i}\\
&u_{k,i} = C_{k,i}\cdot\theta + D_{k,i}\\
&\theta = \left[\begin{array}{ccccccc} T_{m_{2,k}} & mode_{c,k} & \Delta v_{k+1} & SOC_k & \omega_{e,k} & mode_{s,k} & \Delta v_k \end{array}\right]'\\
&u_{k,i} = \left[\begin{array}{c} u_{k,i}^{1\ '} \\ u_{k,i}^{2\ '} \\ u_{k,i}^{3\ '} \end{array}\right] = \left[\begin{array}{c} T_{m_{2,k}} \\ mode_{c,k} \\ \Delta v_{k+1} \end{array}\right]\\
&i = \min\left|soc - \frac{SOC_{k,i} + SOC_{k,i+1}}{2}\right|\\
&i \in \left\{1,2,...,M\right\}: \text{SOC region point}\\
&h_{e_{1,k}} = \min\left|\bar{\omega}_{e_k,h_{1,k}} - \omega_{e_k}\right|, h_{e_{1,k}} \in \left\{1,...,20\right\}: \text{engine segment}\\
&h_{e_{2,k}} = \min\left|\bar{T}_{e_k,h_{2,k}} - T_{e_k}\right|, h_{e_{2,k}} \in \left\{1,2,3\right\}: \text{torque segment}\\
&h_{m1_{1,k}} = \min\left|\bar{\omega}_{m_{1,k},h_{m1,k}} - \frac{\left(\omega_{v_{f,k}}\cdot R_2 + \omega_{v_{r,k}}\cdot S_2\right)\cdot\frac{R_1+S_1}{R_2+S_2} - \omega_{e_k}\cdot R_1}{S_1}\right|\\
&h_{m1_{1,k}} \in \left\{1,...,20\right\}: \text{motor segment}\\
&h_{m1_{2,k}} = \min\left|\bar{T}_{m_{1,k},h_{2,k}} - T_{m_{1,k}}\right|, h_{m1_{2,k}} \in \left\{1,2,3\right\}: \text{torque segment}\\
&h_{m2_{1,k}} = \min\left|\bar{\omega}_{m_{2,k},h_{m_{1,k}}} - \omega_{v_{r,k}}\right|, h_{m2_{1,k}} \in \left\{1,...,20\right\}: \text{motor segment}\\
&h_{m2_{2,k}} = \min\left|\bar{T}_{m_{2,k},h_{2,k}} - T_{m_{2,k}}\right|, h_{m2_{2,k}} \in \left\{1,2,3\right\}: \text{torque segment}\\
&M: \text{number of } SOC_{k,range}
\end{aligned}
\tag{5.48}
$$

$$A_{k,i}{}' = \begin{bmatrix} a_{k,i}^1 & a_{k,i}^2 & a_{k,i}^3 & a_{k,i}^4 & a_{k,i}^5 & a_{k,i}^6 & a_{k,i}^7 \end{bmatrix}$$

$$a_{k,i}^1 = 0$$

$$a_{k,i}^2 = 0$$

$$a_{k,i}^3 = 0$$

$$a_{k,i}^4 = \frac{V_{k,i}\,|_{SOC_{k,i};\Delta v_k=0} - V_{k,i+1}\,|_{SOC_{k,i+1};\Delta v_k=0}}{SOC_{k,i} - SOC_{k,i+1}} \tag{5.49}$$

$$a_{k,i}^5 = 0$$

$$a_{k,i}^6 = 0$$

$$a_{k,i}^7 = \frac{W_k}{\min(\Delta v_k) - \max(\Delta v_k)}$$

$$\begin{aligned} B_{k,i}{}' = & -\frac{V_{k,i}\,|_{SOC_{k,i};\Delta v_t=0} - V_{k,i+1}\,|_{SOC_{k,i+1};\Delta v_t=0}}{SOC_{k,i} - SOC_{k,i+1}} \cdot SOC_{k,i} \\ & - \frac{W_k}{\min(\Delta v_k) - \max(\Delta v_k)} \cdot \min(\Delta v_k) \\ & + V_{k,i} \end{aligned} \tag{5.50}$$

$$
\begin{aligned}
C_{k,i}{}' &= \begin{bmatrix} c_{k,i}^1 & c_{k,i}^2 & c_{k,i}^3 & c_{k,i}^4 & c_{k,i}^5 & c_{k,i}^6 & c_{k,i}^7 \\ c_{k,i}^8 & c_{k,i}^9 & c_{k,i}^{10} & c_{k,i}^{11} & c_{k,i}^{12} & c_{k,i}^{13} & c_{k,i}^{14} \\ c_{k,i}^{15} & c_{k,i}^{16} & c_{k,i}^{17} & c_{k,i}^{18} & c_{k,i}^{19} & c_{k,i}^{20} & c_{k,i}^{21} \end{bmatrix} \\
c_{k,i}^1 &= 0, \quad c_{k,i}^2 = 0, \\
c_{k,i}^3 &= \frac{mR_{tire}}{FD \cdot \Delta t} \\
c_{k,i}^4 &= \left(1 + \frac{SOC_{k,i+1+J_{i+1}} - SOC_{k,i+J_i}}{SOC_{k,i} - SOC_{k,i+1}}\right) \frac{E_{total}}{\beta_1^{h_{1,k}} \cdot \bar{\omega}_{e_k,h_{1,k}} \cdot \Delta t} \\
c_{k,i}^5 &= 0, \quad c_{k,i}^6 = 0 \\
c_{k,i}^7 &= \left(\frac{\rho A C_d \cdot R_{tire} \cdot v_{t,original}}{FD} + \frac{mR_{tire}}{FD \cdot \Delta t}\right) \\
c_{k,i}^8 &= 0, \quad c_{k,i}^9 = 0 \\
c_{k,i}^{10} &= 0, \quad c_{k,i}^{11} = 0, \quad c_{k,i}^{12} = 0 \\
c_{k,i}^{13} &= 0, \quad c_{k,i}^{14} = 0, \quad c_{k,i}^{15} = 0 \\
c_{k,i}^{16} &= 0, \quad c_{k,i}^{17} = 0, \quad c_{k,i}^{18} = 0 \\
c_{k,i}^{19} &= 0, \quad c_{k,i}^{20} = 0, \\
c_{k,i}^{21} &= 1 + \frac{\Delta v_{k,i+1+J_{i+1}} - \Delta v_{k,i+J_i}}{\Delta v_{k,i} - \Delta v_{k,i+1}}
\end{aligned}
\tag{5.51}
$$

$$
D_{k,i}{}' = \begin{bmatrix} d_{k,i}^1 \\ d_{k,i}^2 \\ d_{k,i}^3 \end{bmatrix}
$$

$$
\begin{aligned}
d_{k,i}^1 &= -\left(1 + \frac{SOC_{k,i+1+J_{i+1}} - SOC_{k,i+J_i}}{SOC_{k,i} - SOC_{k,i+1}}\right) \frac{E_{total} \cdot SOC_{k,i}}{\beta_1^{h_{1,k}} \cdot \bar{\omega}_{e_k,h_{1,k}} \cdot \Delta t} \\
&\quad + \frac{\left(SOC_{k,i} - SOC_{k,i+J_i}\right) \cdot E_{total} - \beta_0^{h_{1,k}} \cdot \Delta t}{\beta_1^{h_{1,k}} \cdot \bar{\omega}_{e_k,h_{1,k}} \cdot \Delta t}
\end{aligned}
\tag{5.52}
$$

$$
d_{k,i}^2 = mode_{opt}, \left\{ f_{k-1}\left(\omega_{v_k}, T_{v_k}, mode_{opt}\right)|_{\omega_{v_k}, T_{v_k}, \Delta soc} \Rightarrow \text{minimum} \right\}
$$

$$
d_{k,i}^3 = \sup\left(\underline{v}, \inf\left(\left(-\left(1 + \frac{\Delta v_{k,i+1+J_{i+1}} - \Delta v_{k,i+J_i}}{\Delta v_{k,i} - \Delta v_{k,i+1}}\right)\Delta v_{k,i} + \Delta v_{k,i} - \Delta v_{k,i+J_i}\right), \bar{v}\right)\right)
$$

$$
\begin{aligned}
&V_{k,i} = \min\left[v_i,...,v_{i+M}\right] \\
&v_j = V_{k+1,I}\left(soc_i\right)\big|_{\Delta v_k=0} + \alpha_0^{h_{1,k},h_{2,k}} + \alpha_1^{h_{1,k},h_{2,k}} \cdot \bar{\omega}_{e_k,h_{1,k}} \\
&\qquad + \alpha_2^{h_{1,k},h_{2,k}} \cdot \left(T_{v_k} + \frac{\beta_0^{h_{1,k}}}{\beta_1^{h_{1,k}} \cdot \bar{\omega}_{e_k,h_{1,k}}} \right) - \alpha_2^{h_{1,k},h_{2,k}} \cdot \frac{E_{total}}{\beta_1^{h_{1,k}} \cdot \bar{\omega}_{e_k,h_{1,k}}} \cdot \left(soc_i - soc_j \right) \\
&soc_{i+M} = soc_i + \Delta SOC_{k,4} \\
&j \in \left\{ i,...,i+M \right\} \\
&soc_j \in \left\{ soc_i,...,soc_{i+M} \right\} \\
&soc_i \in SOC_{k,range} \\
&J_i : \text{index of } V_{k,i} \text{ for the minimum} \\
&I = \min \left| soc_i - \frac{SOC_{k+1,I} + SOC_{k+1,I+1}}{2} \right| \\
&W_k = f_k\left(\bar{\omega}_{e_k,h_{1,k}}, \frac{T_{v_k}}{gr_{c,k}} \right) - f_k\left(\bar{\omega}_{e_k,h_{1,k}}, \frac{T_{v_k} + \Delta T_{v_k}}{gr_{c,k}} \right)
\end{aligned}
\tag{5.53}
$$

$$
\begin{aligned}
SOC_{k,range} = &\left\{ SOC_{k+1,range} + \Delta SOC_{k,1} \right\} \cup \left\{ SOC_{k+1,range} + \Delta SOC_{k,2} \right\} \\
&\cup \left\{ SOC_{k+1,range} + \Delta SOC_{k,3} \right\} \cup \left\{ SOC_{k+1,range} + \Delta SOC_{k,4} \right\}
\end{aligned}
\tag{5.54}
$$

$$
\begin{aligned}
\Delta SOC_{k,1} &= \frac{\Delta t}{E_{total}} \cdot \left[\left(T_{v_k} - T_{e,4} \right) \cdot \bar{\omega}_{e_k,h_{1,k}} \cdot \beta_1^{h_{1,k}} + \beta_0^{h_{1,k}} \right] \\
\Delta SOC_{k,2} &= \frac{\Delta t}{E_{total}} \cdot \left[\left(T_{v_k} - T_{e,3} \right) \cdot \bar{\omega}_{e_k,h_{1,k}} \cdot \beta_1^{h_{1,k}} + \beta_0^{h_{1,k}} \right] \\
\Delta SOC_{k,3} &= \frac{\Delta t}{E_{total}} \cdot \left[\left(T_{v_k} - T_{e,2} \right) \cdot \bar{\omega}_{e_k,h_{1,k}} \cdot \beta_1^{h_{1,k}} + \beta_0^{h_{1,k}} \right] \\
\Delta SOC_{k,4} &= \frac{\Delta t}{E_{total}} \cdot \left[\left(T_{v_k} - T_{e,1} \right) \cdot \bar{\omega}_{e_k,h_{1,k}} \cdot \beta_1^{h_{1,k}} + \beta_0^{h_{1,k}} \right]
\end{aligned}
\tag{5.55}
$$

5.6.2 Optimization Results

The relaxed optimization of the winning AWD power-split Design *A* identified in Chapter 3 is performed in the UDDS and HWFET drive cycles, and compared to results obtained by DP with PEARS in Chapter 3. Fuel consumption results are summarized in

Table 5.6. Results verify that the relaxed optimization concept results in additional fuel consumption reduction of 10% compared to results without relaxing the vehicle speed.

Table 5.6 Fuel Consumption of the Identified AWD Power-split Design *A*

Solving Method	Relaxation	Fuel Consumption (g)	
		UDDS	HWFET
DP+PEARS	Battery SOC	353.5	938.9
MPP	Battery SOC	348.6	935.2
MPP	Battery SOC + Vehicle Speed	312.2	918.5

CHAPTER 6

Near-Optimal Real-Time Control Strategy: Battery State-of-Charge Pulse-and-Glide Strategy

In Chapter 4 and Chapter 5, the relaxed optimization control problem of the HEV is formulated and solved offline. These benchmarking results from this off-line optimization usually are not implementable as the real-time control strategy because of the necessity of prior driving knowledge and the limitation of online computational resources. However, these results can provide an insightful analysis of system operation. In the aforementioned chapters, both the numerical and analytical results of the optimization are obtained. Pulse-and-glide behavior is observed for the vehicle speed and/or SOC trajectory "wandering" around the desired values. The zero power, the optimal point of the powertrain control, and the engine sweet-spot are identified as the hybrid system optimal controls. Then, the solutions of the powertrain control optimization problem can be approximated by re-constructing controls from the set of optimal controls. This analysis then becomes the knowledge of control strategy framework development.

In this chapter, the analysis and optimization of the powertrain system control are developed; accordingly, an optimized control set can be then generated. A framework for constructing the real-time control strategy based on the pre-optimized system optimal control is developed and evaluated over different models and scenarios. Results of this strategy's performance is compared with other methods and justified within conditions of using common drive cycles including HWFET, FTP-75, UDDS, and NYCC.

The analysis and control development framework were established based on assumptions that the responses of the powertrain mechanical dynamics (e.g., rotational speeds of all components) are significantly faster than the electrical dynamics (e.g., the battery SOC); all possible states of the rotational components can be achieved while the

state-of-charge of the battery system takes time to reach each possible state. Therefore, problem simplification to highlight the low-speed response dynamic becomes reasonable.

6.1 Battery SOC Pulse-and-Glide based on HEV Model Simplification

Toyota Prius Gen I is used as a case study for concept development and simulation demonstration because it is a simpler example without additional states (e.g., operating mode) and it retains the power-split attribute. The developed framework is not limited to this example and can be generalized for all hybrid powertrain systems. The powertrain of the Toyota Prius Gen I (Figure 6.1) is transformed into the lever diagram analogy shown in Figure 6.2. The complete dynamics of the system are given by Eq. (6.1), and different rotational relationships are specified in Eq. (6.2). In the equations, $\dot{\omega}$ denotes the acceleration vector of all rotating components, A is the transfer matrix that transfers the torque vector T into acceleration, f_e denotes the engine fuel rate $\dot{m}_f$ as a function of engine speed ω_e and engine torque T_e, f_{bat} denotes the battery SOC change rate as a function of battery power P_{batt} is calculated by motor speeds (ω_{em1} and ω_{em2}), motor torques (T_{em1} and T_{em2}) and motor efficiencies (η_{em1} and η_{em2}). The open-circuit voltage is V_{oc}; the battery internal resistance is R_{bat}; $I_{(\cdot)}$ denotes the corresponding inertia, and $T_{(\cdot)}$ denotes the corresponding components' torques. R and S refer to the radii of the ring gear and sun gear of the planetary gear respectively.

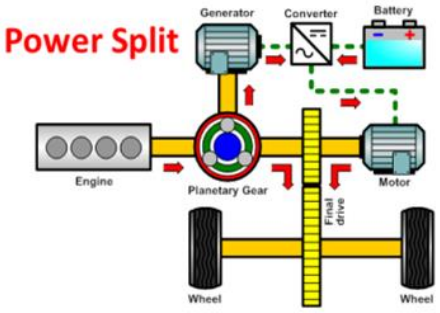

Figure 6.1 Toyota Prius Gen I vehicle and its powertrain design

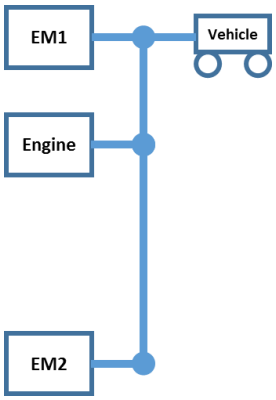

Figure 6.2 Lever diagram of Prius powertrain

$$
\begin{aligned}
&\dot{\Omega} = A^{-1} \cdot T \\
&\dot{m}_f = f_e\left(\omega_e, T_e\right) \\
&\dot{SOC} = f_{bat}\left(P_{bat}\right) \\
&\dot{SOC} = -\frac{V_{oc} - \sqrt{V_{oc}^{\ 2} - 4R_{bat}P_{batt}}}{2 \cdot R_{bat}} \\
&P_{bat} = \omega_{em1} \cdot T_{em1} \cdot \eta_{em1}^{k\_em1} + \omega_{em2} \cdot T_{em2} \cdot \eta_{em2}^{k\_em2} \\
&SOC_{\min} \le SOC \le SOC_{\max} \\
&k\_em1 = \begin{cases} -1 & \omega_{em1} \cdot T_{em1} \ge 0 \\ 1 & \omega_{em1} \cdot T_{em1} < 0 \end{cases} \\
&k\_em2 = \begin{cases} -1 & \omega_{em2} \cdot T_{em2} \ge 0 \\ 1 & \omega_{em2} \cdot T_{em2} < 0 \end{cases}
\end{aligned}
\tag{6.1}
$$

$$\dot{\Omega} = \begin{bmatrix} \dot{\omega}_e \\ \dot{\omega}_v \\ \dot{\omega}_{em2} \\ 0 \end{bmatrix},$$

$$A^{-1} = \begin{bmatrix} I_e & 0 & 0 & R+S \\ 0 & I_v + I_{em1} & 0 & -R \\ 0 & 0 & I_{em2} & -S \\ R+S & -R & -S & 0 \end{bmatrix}, \tag{6.2}$$

$$T = \begin{bmatrix} T_e \\ -T_v + T_{em1} \\ T_{em2} \\ F_{PG} \end{bmatrix}$$

The Prius powertrain dynamics have two controls (engine torque, and EM1 torque) and two states (engine speed and battery SOC). Because the engine dynamics are much faster than the battery dynamics, and the engine speed can be controlled to any target values in less than one second, the battery SOC dynamics, which is significantly slower, are highlighted for the HEV control.

Different from the pulse-and-glide strategy for conventional that analyzes the system using the relationship between fuel rate and engine power, as shown in Figure 6.3, the SOC pulse-and-glide strategy for HEV analyzes the system based on the relationship between fuel rate and battery SOC change (referred to as $S\dot{O}C$). This analysis for the HEV considers all losses, including motor losses and battery losses, along the electrical path.

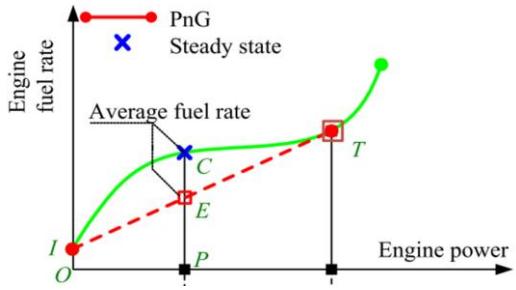

Figure 6.3 Engine power pulse-and-glide analysis [29]

Based on this concept, given any demand of vehicle torque and vehicle speed, the original optimization problem in Eqs. (6.1) – (6.2) is simplified to be the relationship of fuel rate versus battery SOC change in Eq. (6.3), shown below.

$$\dot{m}_f = f_{SOC}\left(S\dot{O}C\right)|_{v,T_v} \tag{6.3}$$

The mapping in Eq. (6.3) can be calculated numerically given the driver demand with vehicle torque and vehicle speed, with all different engine state. The minimum fuel rate across different SOC change can be obtained together with optimal system controls. For example, given the vehicle torque T_v=*50*Nm and vehicle speed v=*15*mph, the curve of minimum fuel rate v.s. the battery SOC change can be obtained and shown in Figure 6.4. By analyzing the non-convexity of this curve (highlighted in light blue), this hybrid system can achieve minimum fuel consumption if it chooses to operate alternately between the zero-engine-output point and the point at which the slope increases in the region of positive $S\dot{O}C$ (the two circle dots). This way, the average fuel consumption, highlighted by the red dash-line connecting the above two control points, is always lower than any other points on the original minimum fuel-rate curve. The average optimum is highlighted in the red asterisk dot, which refers to the optimal fuel consumption at charge-sustaining condition Therefore, minimum fuel consumption is guaranteed. The two control points under the given vehicle state are optimal system controls. Combining all these optimal hybrid system controls constructs the optimal control set.

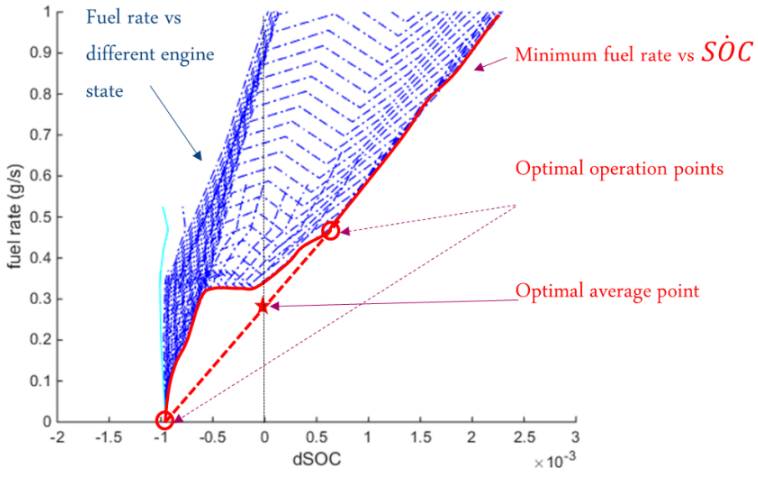

Figure 6.4 Battery SOC pulse-and-glide analysis

By applying the aforementioned analysis to all different vehicle demands (vehicle speed and torque), the set of all optimal operating points are obtained for the Prius engine, as shown in Figure 6.5. This set of optimal operating points can be characterized as two categories: optimal engine-on control and engine-off control.

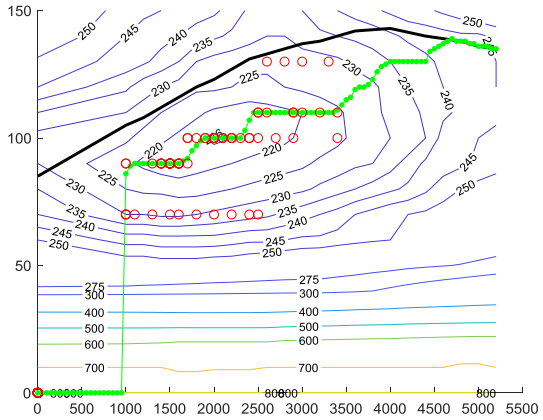

Figure 6.5 Set of all optimal operating points of Prius powertrain

By utilizing this SOC pulse-and-glide strategy, the resulting battery SOC exhibits a pulse-and-glide behavior because of the control switch between charging and discharging. The battery SOC fluctuates in the proximity of the desired SOC and shows the pulse-and-glide behavior as a consequence of the proposed switching control strategy.

6.2 Control Design: Battery State-of-Charge Pulse-and-Glide Strategy

After obtaining all the optimal system controls under all driver demand, an optimization problem is formulated to decide where and when to apply the switch.

Given the representative drive cycles, an average equivalent fuel consumption $\bar{f}_{EFC}$ is defined, and the optimization problem for minimum cost is formulated, as given in Eq. (6.4).

$$\begin{aligned} &\min \quad f = \bar{f}_{EFC} = \sum \eta_{cycle}(v,T)|_{engine-on} \cdot f_{SOC}(\Delta SOC, v, T) \\ &\Delta SOC = f(v,T_v)|_{\dot{m}_f^*(k)} \\ &\sum \left[\eta_{cycle}(v,T)|_{engine-on} + \eta_{cycle}(v,T)|_{EV} \right] = 1 \\ &\sum \Delta SOC = 0 \end{aligned} \tag{6.4}$$

This optimization problem can be solved through a linear programming algorithm in a computationally efficient manner. The computational cost is low, because there is only one control (optimal system control) and one state (battery SOC).

Once the optimization problem in Eq. (6.4) is solved, a control map for switching between engine-on and engine-off is generated, as shown in Figure 6.6, where the yellow region refers to engine-on operations and the blue region refers to the engine-off operations.

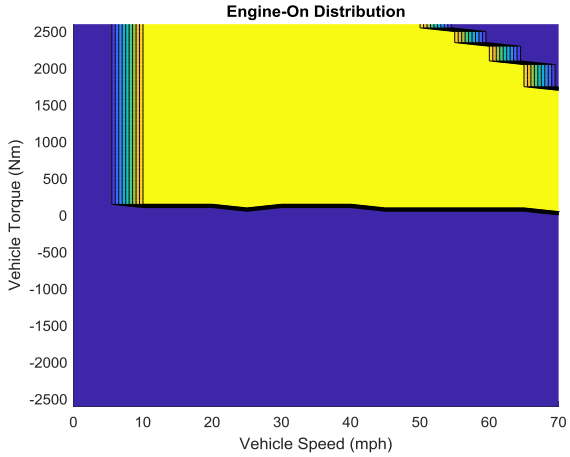

Figure 6.6 Engine-on and engine-off switch map

With the generated control map and optimal-control set, the control structure for the SOC pulse-and-glide strategy is presented in Figure 6.7. This control map ensures that the Prius operates at its system-optimal points. The engine-on map ensures that the final battery SOC will be in the proximity of the desired state.

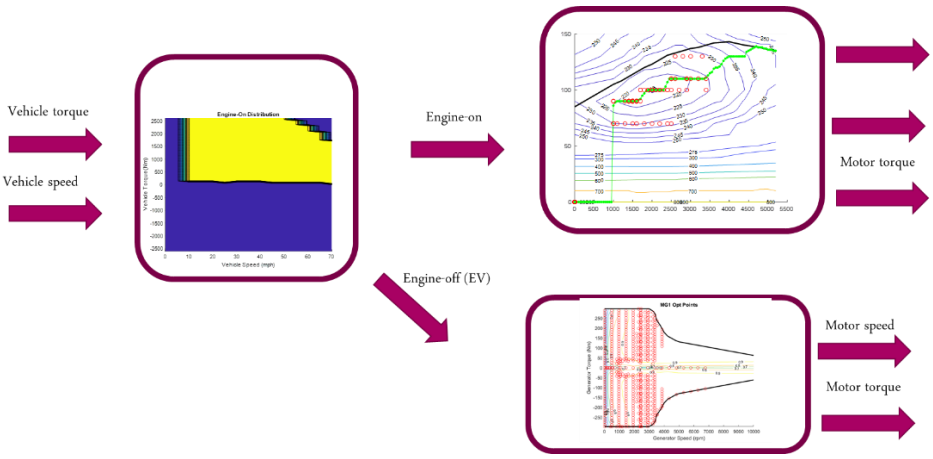

Figure 6.7 Energy management strategy layout

6.3 Simulation Results: Battery State-of-Charge Pulse-and-Glide Strategy

The simulations are performed under different drive cycles for the proposed battery SOC Pulse-and-Glide strategy, and compared to results obtained by the DP. As summarized in Table 6.1, the simulation results using the battery SOC pulse-and-glide strategy are 5–6% different from the results from the DP over different driving scenarios.

Table 6.1 Simulation Result Summary Using Battery SOC Pulse-and-Glide Strategy

	Driving Scenarios	NYCC	UDDS	FTP-75	HWFET
Fuel (g)	DP	19.8	249.7	378.5	278.4
	Battery SOC PnG	21.1	264.2	403.1	294.6
Result Difference		6.4%	5.8%	6.5%	5.5%

The achieved results of 5-6% difference comparing to the global optimal result are considerably great performance, for a real-time control strategy without knowledge of the precise drive cycles nor without intensive neural network training beforehand. From reviewed literatures of existing methods and applications, rule-based control algorithms in general achieve results of 16-20% different from the optimal result [50]. Other instantaneous optimization method such as ECMS and model predictive control (MPC) usually achieve results around 12-30% different from the optimal if not knowing the exact drive cycle beforehand [51]; the ECMS with adaptation achieves results of 7-12% differences from the optimal result [50]. The online optimization, if with knowledge of driving cycles, calibration on the control factor, intensive training computation, or pattern recognition, can achieve close to optimal results [42, 52, 53]. Other control methods such as pattern recognition and neural network demonstrate results of 3 – 8% differences from the optimal result [54]. The performance of the aforementioned methods are summarized in Figure 6.8. Overall, the proposed control strategy framework, which utilizes battery SOC pulse-and-glide strategy, shows great performance, without knowledge of speed profile

ahead nor intensive computation of pre-training. Moreover, this framework can be systematically and automated implemented on different HEV powertrains.

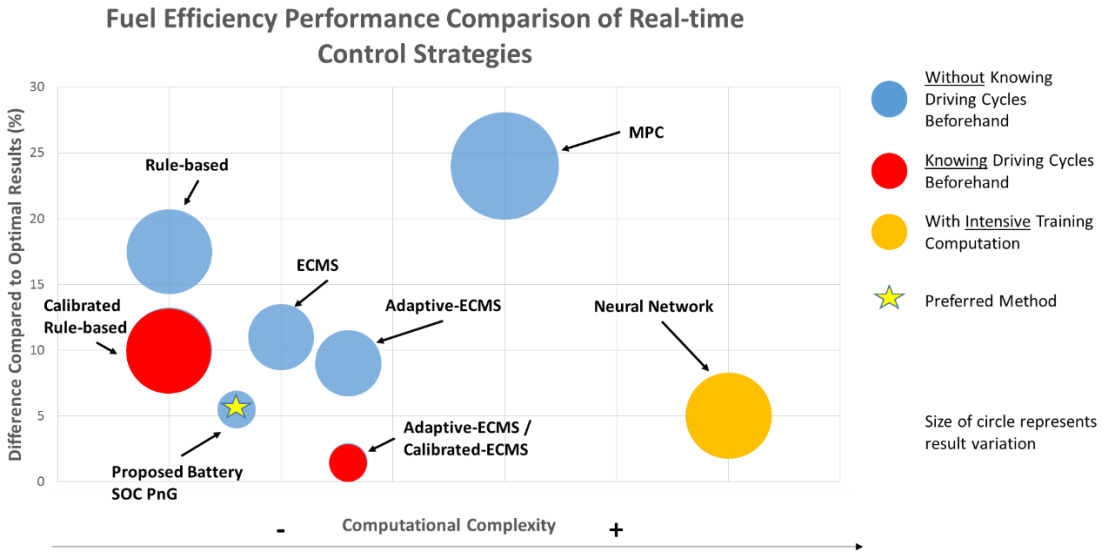

Figure 6.8 Fuel efficiency performance comparison of real-time control strategies

The battery SOC trajectory, components' torques, and components' speeds over the UDDS drive cycle are presented in Figure 6.9 as illustration. Both results indicate the switching behavior between engine-on and engine-off; this behavior results in battery SOC "pulse and glide". The resulted battery SOC trajectories are different but the resulted fuel consumption values are closed. This indicates that likely there are multiple optimal / near-optimal solutions in the HEV optimization problem because of the non-convexity of the problem.

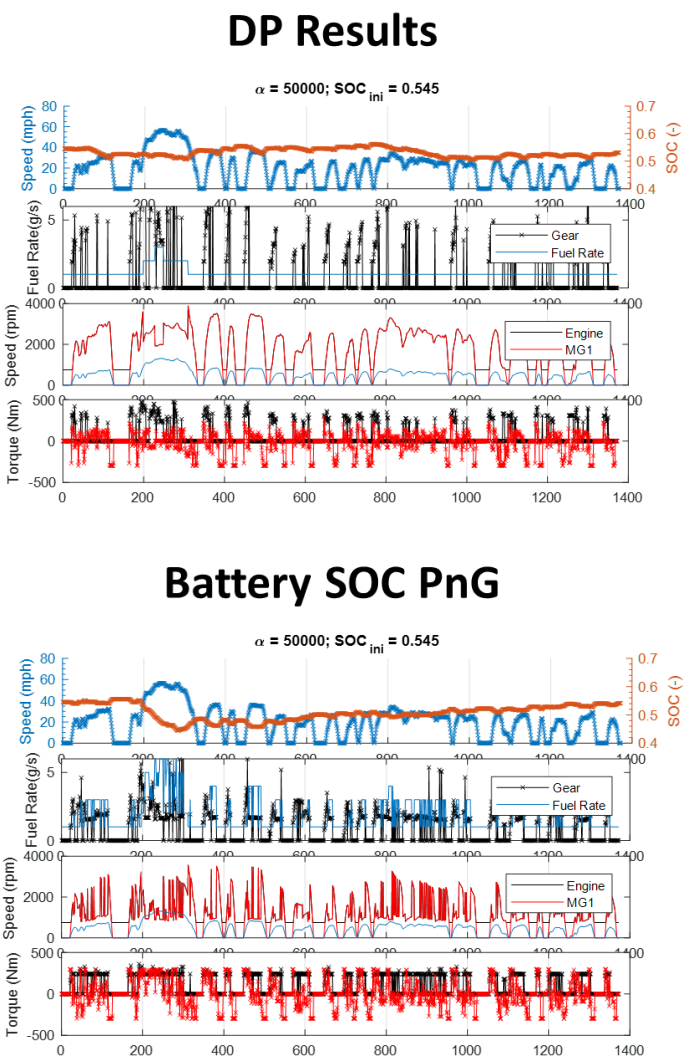

Figure 6.9 Result comparison between DP and battery SOC PnG over UDDS drive cycle

This real-time control strategy development framework was also implemented on a 2012 Chevrolet Volt, as another case study to verify performance of the developed strategy. Although the framework was not yet completed when utilized for the 2018 IEEE VTS Challenge. The concept of battery SOC Pulse-and-Glide showed promising performance and achieved No.5 globally among the 52 competitors in this competition. More details of this implementation case study can be found in Appendix C. If the framework had been completed earlier, the final results for this competition were expected to be better.

6.4 Battery SOC Pulse-and-Glide Development for AWD

6.4.1 Battery SOC Pulse-and-Glide Control Development

The system dynamics of the AWD multi-mode power-split hybrid powertrain winning design, Design *A* investigated in Chapter 3, are further analyzed for battery SOC pulse-and-glide control strategy development as a case study for the AWD hybrid powertrain. The dynamics of Design *A* has two-DOF with operating mode, engine speed, and battery SOC, as states; corresponding operating mode and MG2 torque as controls. The fuel cost depends on all the aforementioned states and controls, as indicated in Eq. (6.5).

$$\dot{m}_f = f_{AWD-PowerSplit}\left(mode_{sta}, \omega_e, SOC, mode_{ctr}, T_{MG2}\right)\big|_{v,T_v} \tag{6.5}$$

This optimization problem is solved following the same process described in below. The simplified dynamics is shown in Eq. (6.6), where $\dot{SOC}$ is the control and SOC is the state.

$$\dot{m}_f = f_{SOC}\left(\dot{SOC}\right)\big|_{v,T_v} \tag{6.6}$$

The analyzed optimized controls of the AWD power-split winning Design *A* under different vehicle commands (vehicle torque and vehicle speed) are shown in Figure 6.10. The control strategy structure is shown in Figure 6.11.

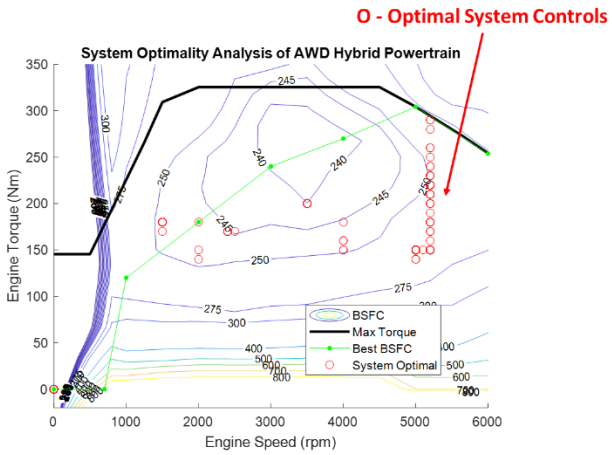

Figure 6.10 Engine operating points in proposed battery SOC pulse-and-glide strategy for AWD winning Design *A* in Chapter 3

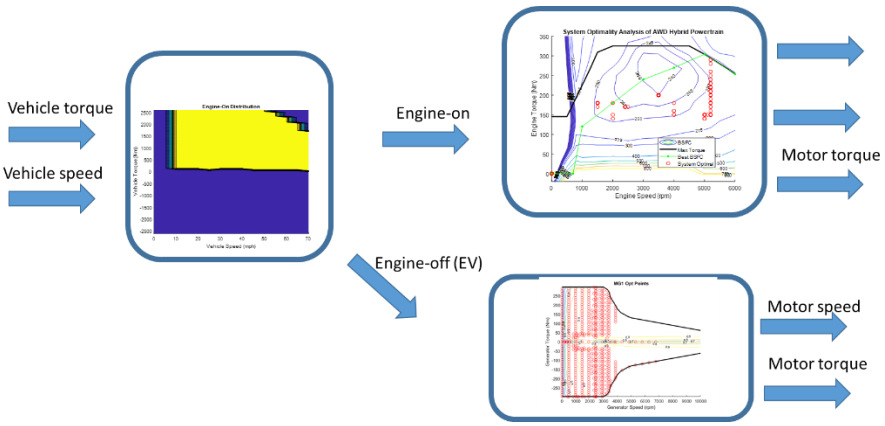

Figure 6.11 Battery SOC pulse-and-glide strategy structure for AWD winning Design *A* in Chapter 3

6.4.2 Simulation Results and Analysis

Analysis, which employs the battery SOC pulse-and-glide for the AWD power-split design, is presented in Figure 6.12, under the condition of vehicle torque T_v=*100*Nm and vehicle speed *v*=*35*mph. The non-convex characteristic of this hybrid powertrain system is verified. The plotted result also verifies there exist the two saddling points (zero engine torque and hybrid system optimal control) for the hybrid electric system. Operation at these two saddling points is more efficient than using the engine sweet spot, if the electrical energy buffer (battery system) is employed; whereas operation between the engine sweet spot and zero torque is more efficient, if the vehicle kinetic energy is utilized as the mechanical energy buffer. The real-time control strategy of battery SOC pulse-and-glide is reconstructed from the set of these three operation sets.

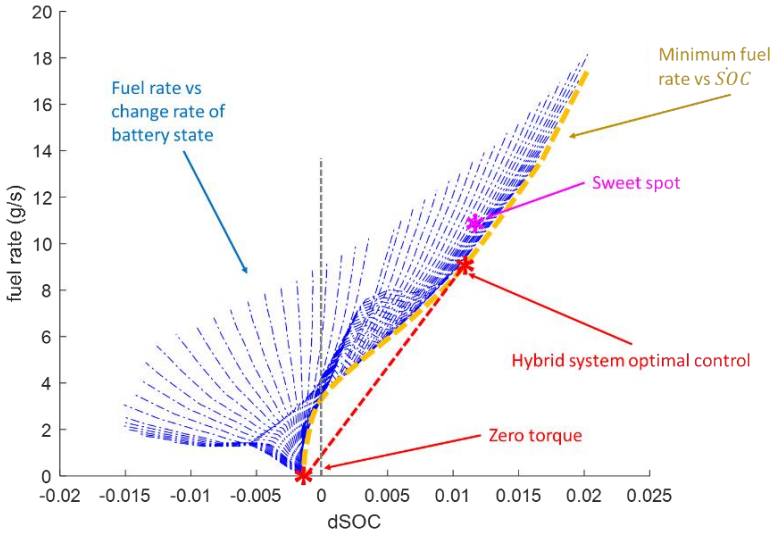

Figure 6.12 Battery SOC pulse-and-glide analysis of AWD power-split design

Simulations of the Design *A* investigated in Chapter 3 are performed under different drive cycles for the proposed battery SOC Pulse-and-Glide strategy and compared to results obtained by the DP with PEARS in Chapter 3. As shown in Table 6.2, for the case without speed relaxation, results of simulation using the battery SOC pulse-and-glide strategy are 2-3% different from results from DP with PEARS; for the case with vehicle speed relaxed, additional fuel consumption reduction of 12-13% is obtained.

Table 6.2 Fuel Consumption of Identified AWD Power-split Design A

Control Method	Speed Relaxation	Fuel Consumption (g)	
		UDDS	HWFET
DP+PEARS	N	353.5	938.9
Battery SOC PnG	N	360.2	956.7
Battery SOC PnG	Y	314.2	922.3

The engine operating points and trajectories of battery SOC and component torques in UDDS drive cycle are plotted in Figure 6.13 and Figure 6.14, respectively. Figure 6.13 exhibit the engine operating points distributed in the proximity of the best engine BSFC line (in red) rather than exactly on the best engine BSFC line. With the losses at the two electric motors considered, the optimal controls of the hybrid powertrain system deviate from the system with ICE only. The analysis of the hybrid system optimum is necessary. Figure 6.14 presents "pulse-and-glide" behavior of the battery SOC trajectory and vehicle speed trajectory as desired from the designed strategy. The powertrain system uses the

engine and “pulse” the SOC of the battery energy buffer system and vehicle speed at a low-speed acceleration; and use the electric machine(s) to “glide” the battery SOC at higher vehicle speed.

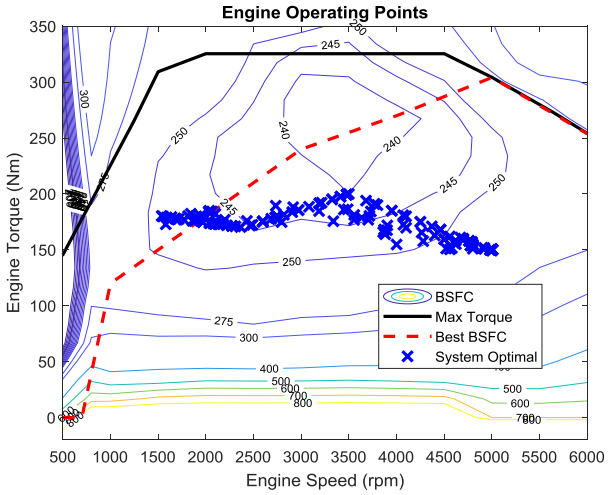

Figure 6.13 Engine operating points of AWD power-split design in UDDS drive cycle

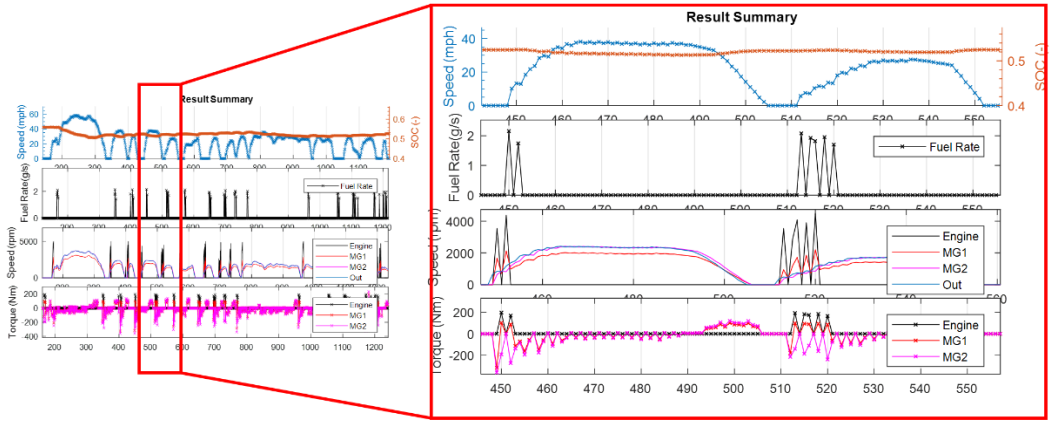

Figure 6.14 Trajectories of Battery SOC and component torques in UDDS drive cycle

The simulation results verify that the established real-time control development framework of battery SOC pulse-and-glide achieves near-optimal performance over fuel efficiency, and the near-optimality can be quantified within a range of 2-6%. This performance is better than most existing control strategies without knowledge of future drive cycle information nor intensively computation of training in neural network application. Moreover, this control strategy is able to be implemented in more complicated

powertrain control optimization problems with high DOFs, such as the AWD power-split hybrid powertrains relaxed optimization.

CHAPTER 7
Experimental Study

In Chapter 2 to Chapter 6, the theoretical development has covered power-split HEV design to optimization and control development, including the AWD and 2WD. The frameworks of the design process and control development are established and investigated. To validate the proposed design process, experimental studies are performed.

As a preparation step, a demonstration platform that enables exhibition of multi-mode power-split powertrain mechanism is firstly developed, as shown in Figure 7.1.With this demonstration platform, emulation of the powertrain operation through a down-scale level to test, validation of a realistic feasibility of a designed power-split hybrid powertrain, and exercise of speed control of this powertrain technology, become possible. More details of this platform can be found in Appendix D.

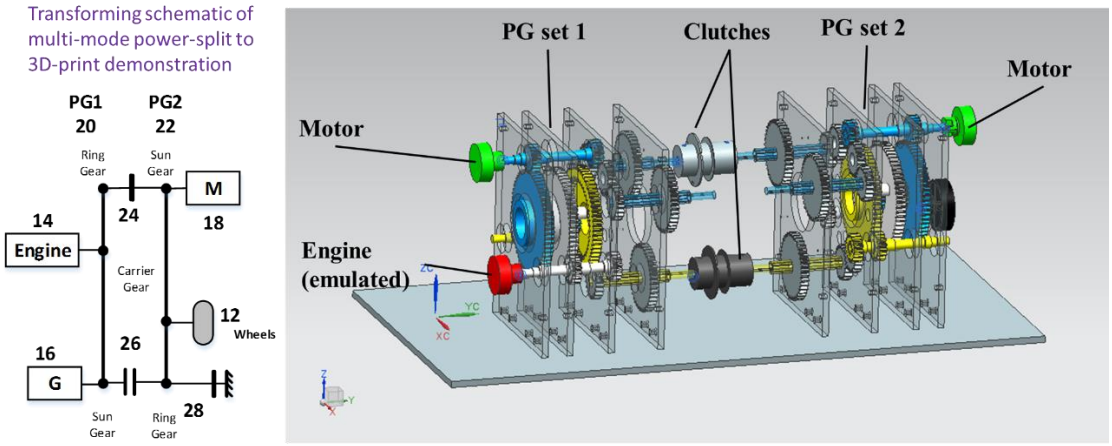

Figure 7.1 Demo platform of multi-mode power-split mechanism

To further validate the framework of design process and control development proposed in this dissertation, a prototype truck is developed, under the DOE funding: Medium-Duty Urban Range Extended Connected Powertrain (MURECP). The goal of this project is to develop and demonstrate a plug-in hybrid electric (PHEV) Class 4 delivery

truck, which reduces fuel consumption by at least 50% compared to a baseline truck, by using an innovative and low-cost hybrid electric powertrain.

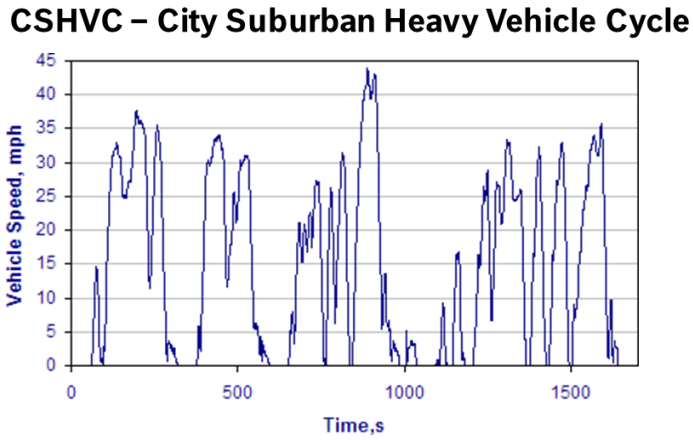

Figure 7.2 CSHVC speed profile

The drive cycle city suburban heavy vehicle cycle (CSHVC), shown in Figure 7.2, is defined as the target cycle for the fuel consumption assessment. This drive cycle is close to the average kinetic intensity versus average driving speed based on the actual field data from multiple delivery trucks, as shown in Figure 7.3 [55], where the kinetic intensity is defined in Eq. (7.1) [56] as a measure of " hybrid advantage", defined as ratio between characteristic acceleration to aerodynamic speed. This CSHVC profile is considered to be a representative for our prototype truck. More details of this drive cycle approach can be referred to work accomplished by the national renewable energy laboratory (NREL) [55].

$$\begin{aligned} HA &\cong 1-\frac{C_{aero}\cdot v_{aero}^2+C_{rolling}+\tilde{a}\cdot\left(1-\bar{\eta}_{regen}\right)}{C_{aero}\cdot v_{aero}^2+C_{rolling}+\tilde{a}} \\ &= \frac{\eta_{regen}}{C_{aero}\cdot\frac{v_{aero}^2}{\tilde{a}}+\frac{C_{rolling}}{\tilde{a}}+1} \end{aligned} \tag{7.1}$$

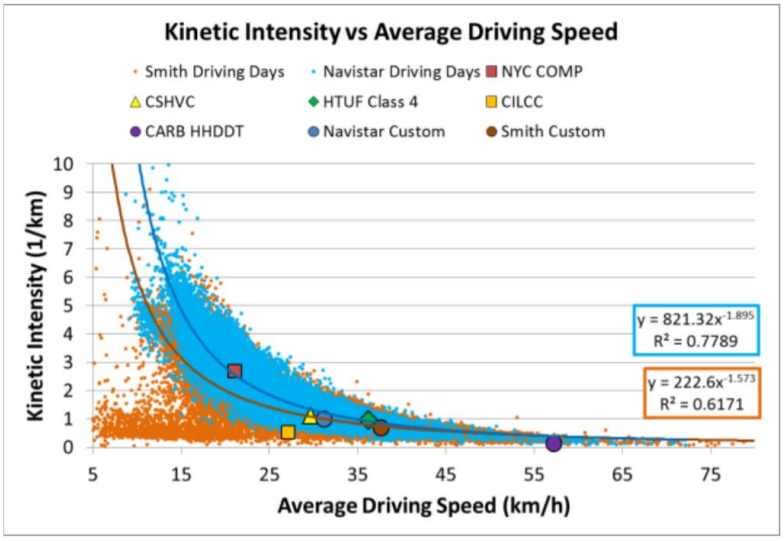

Figure 7.3 Kinetic intensity distribution of collected delivery truck data by NREL [55]

The project set the goal to design an RWD (single-output shaft) multi-mode power-split hybrid powertrain, as a more practical target because it is to be used in the urban environment. AWD will add unnecessary complexity and cost, and thus was not selected.

7.1 Project Overview

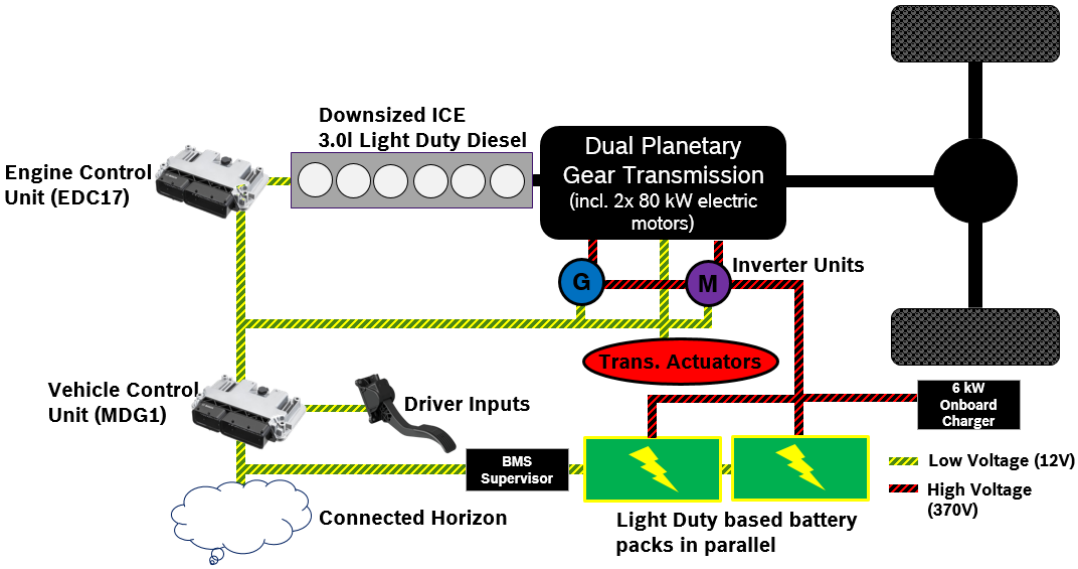

Figure 7.4 Design of a multi-mode power-split hybrid powertrain

To demonstrate the potential for expanding the multi-mode power-split hybrid technology to a boarder market, this project will validate the fuel efficiency improvement

and cost effectiveness of using a dual planetary-gear (2PG) power-split transmission, as shown in Figure 7.4 for a Class 4 PHEV delivery truck using commercialized light-duty vehicle electric drive components (for lower cost). With the power-split and multi-mode attribute, the targeted design is expected to achieve the aggressive target of fuel consumption reduction of 50% and to maintain competitive driving performance such as acceleration, towing capability, and gradeability.

As stated in this dissertation, designs with this set-up involves millions of design candidates. Therefore, it requires the systematic design methodology developed through this dissertation to identify the optimal design, with the capability of adopting all parameters (vehicle weight, etc.) from the target vehicle and components. A proper control strategy, which is developed from the control strategy development framework, will be tested.

By utilizing the entire process developed in this dissertation, this project practice will develop the most promising hybrid configuration for mass-market commercialization within the medium-duty (MD) segment and demonstrate a working prototype for data collection and testing. The project development process is summarized in Figure 7.5.

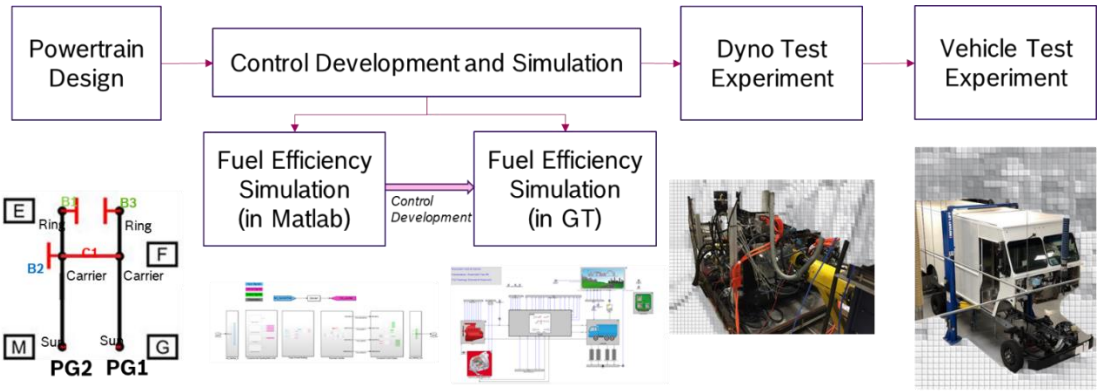

Figure 7.5 Vehicle design process

7.2 Powertrain Design and Development

7.2.1 Design Methodology

Design requirements are defined and used in the design process as shown in Figure 7.6. Besides the mechanical design requirements, such as driving backward with engine-

on, acceleration requirement, gradeability, and towing are required to be no worse than the conventional powertrain vehicle.

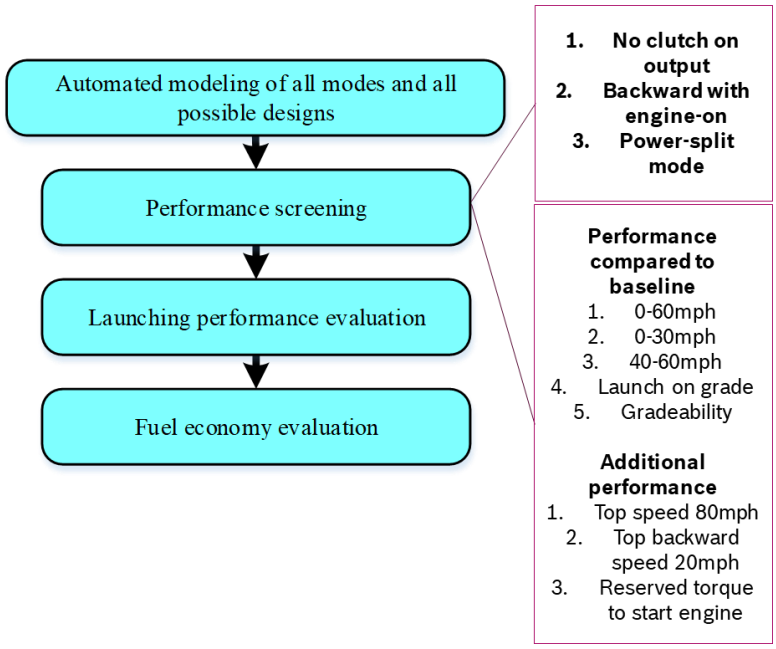

Figure 7.6 Design requirements applied in the four-step design methodology for the MURECP vehicle

The screening process starts from millions of variants and at the end of the screening process, we were able to identify 212 feasible design candidates, as shown in Figure 7.7. The obtained feasible design candidates will be evaluated for acceleration performance and fuel economy.

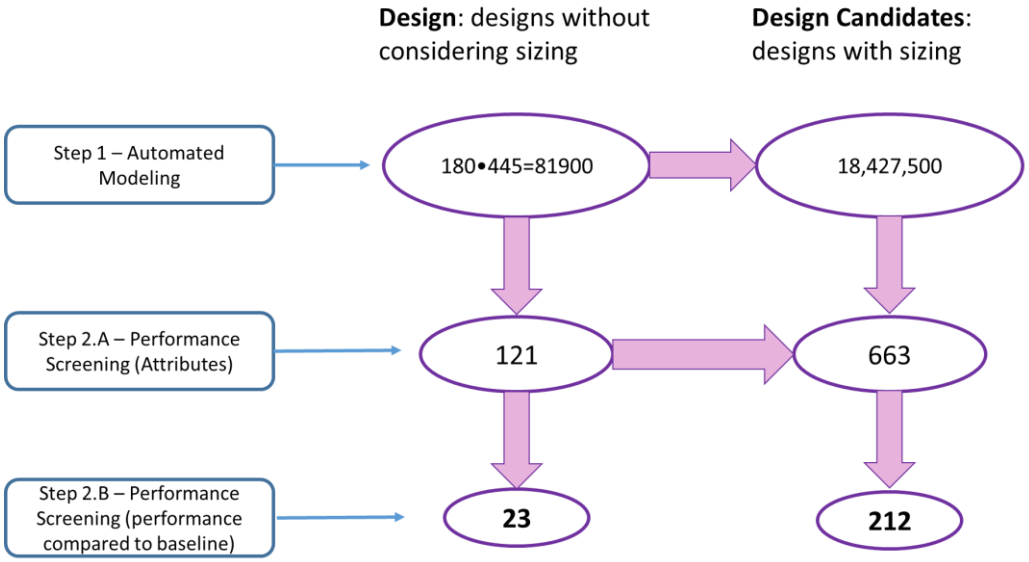

Figure 7.7 Design down-selection through the screening process

7.2.2 Design Identification

Given all the feasible design candidates, the acceleration performance and fuel consumption are evaluated for each, in order to find the optimized designs. The results of acceleration performance and fuel consumption of all feasible design variants are shown in Figure 7.8. The conventional truck and a parallel hybrid truck are also used as benchmarks to indicate fuel efficiency improvement in different technologies. Some designs have better acceleration performance while others show better fuel economy. As indicated in Figure 7.8, the "2PG Group2 designs" are selected for the prototype because they achieved the project target of a fuel consumption reduction of over 50% compared to the baseline ICE truck.

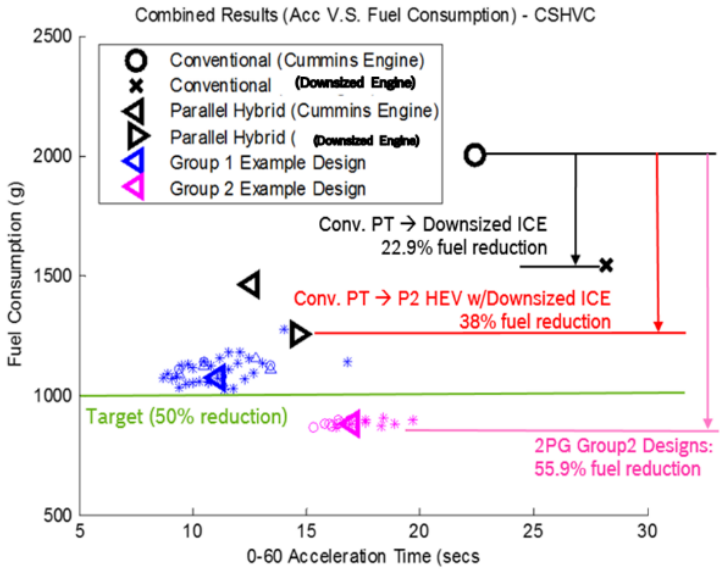

Figure 7.8 Combined results of fuel consumption and acceleration performance of feasible designs

Among the down-selected 212 feasible variants, the optimal design is identified based on the fuel efficiency and manufacturing feasibility. A grounding clutch C2 is added to the identified design, so that a powerful EV mode with two motors can be achieved. This 2-motor EV mode ensures the operation of the delivery truck a zero-emission mode under all power demands through the drive cycle. The winning multi-mode power-split powertrain design is shown in Figure 7.9, together with other identified designs filed in patent application No. 2115-007471-US-PS1.

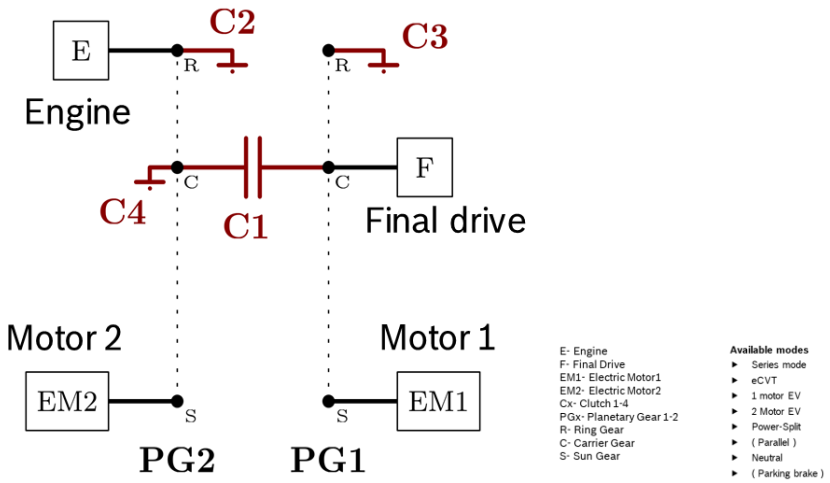

Figure 7.9 Design schematic of winning design

The fuel consumption of the final prototype truck simulated (solved by DP for baseline and PEARS), and the results are shown in Figure 7.10. A fuel consumption reduction of 56.8% is achieved over the CSHVC profile; the design target of over 50% consumption reduction is exceeded.

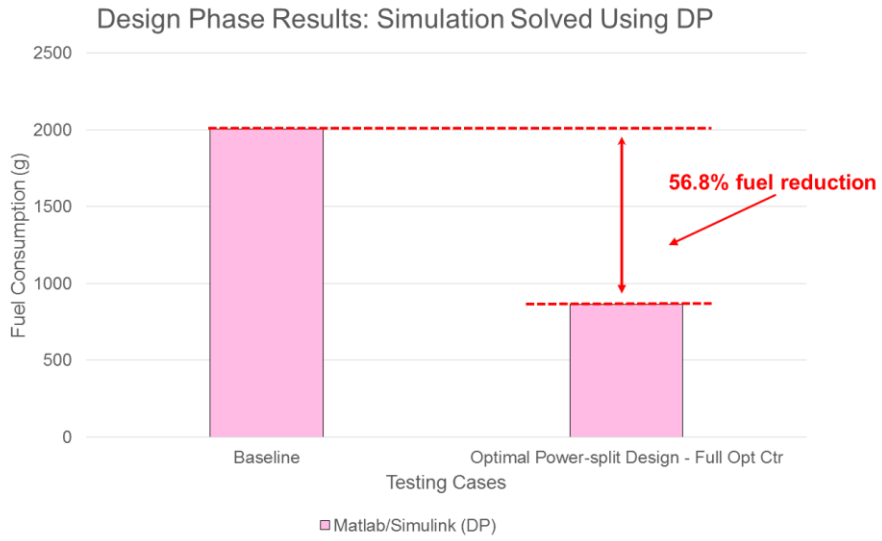

Figure 7.10 Evaluated fuel consumption reduction of identified optimal power-split hybrid design compared to baseline

Given the multi-mode power-split hybrid powertrain schematic in Figure 7.9, the mechanical design of a prototype is then developed and manufactured in Figure 7.11. Based on the schematic of the lever diagram of the winning power-split hybrid design, the 3D drawing of the mechanical design realization is developed. The mechanical prototype is then assembled from design component parts from the 3D drawing.

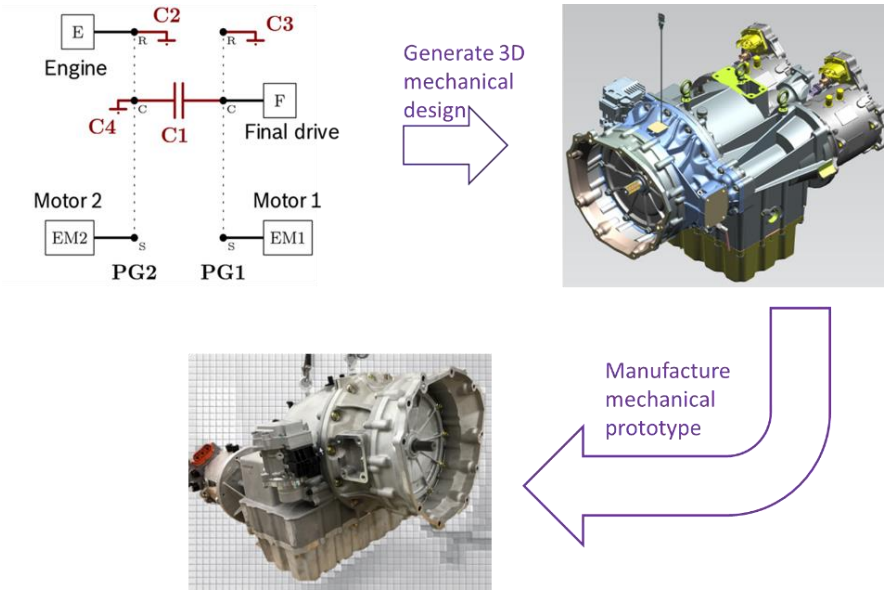

Figure 7.11 Mechanical design realization of winning design

7.3 Simulation and Testing Environment

7.3.1 Simulation Environment

The final simulation environment is developed in both MATLAB/Simulink and GT Suite. The two stage environment development is for two purposes: the MATLAB/Simulink environment captures the powertrain dynamics but with simplified component models. It is used for control development. The GT Suite environment includes more details of the components such as engine loss, transmission loss, e-motor loss, etc. It is used for final simulation verification. The detailed GT Suite model is able to closely align with experiment results if all component sub-models are calibrated against the real hardware. The simulation environment set-up for MATLAB/Simulink and GT Suite are shown in Figure 7.12 and Figure 7.13, respectively.

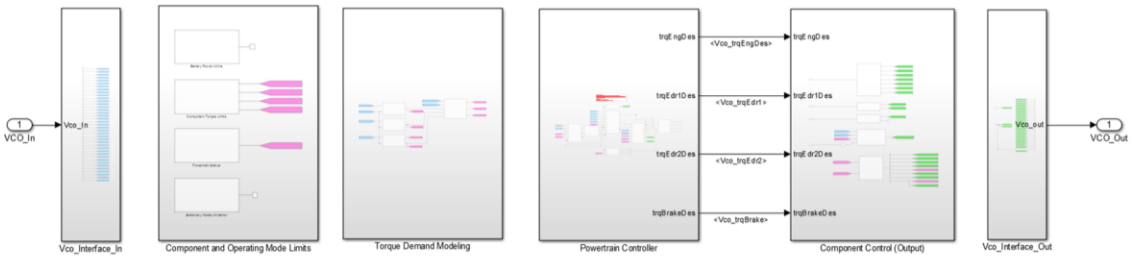

Figure 7.12 MATLAB/Simulink modeling environment

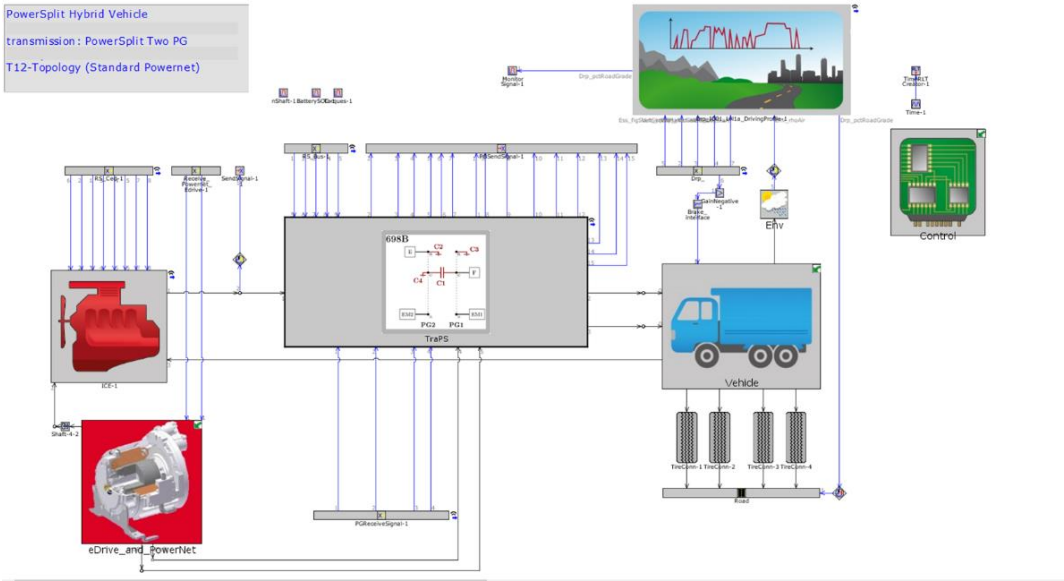

Figure 7.13 GT Suite modeling environment

7.3.2 Experiment Environment

The testing environment includes three phase of experiments: powertrain dyno testing, integrated vehicle chassis dyno testing, and vehicle on-road testing. The prototype transmission is set up in the dyno laboratory with the transmission output shaft attached to the dynamometer, as shown in Figure 7.14. Different functionalities are verified and calibrated including the EV mode (single mode) operation, power-split (single mode) operation, and power-split control calibration, etc. Fuel consumption experiments are conducted to verify and to be compared with simulation results. Due to time constraint, we do not have multi-mode test results yet.

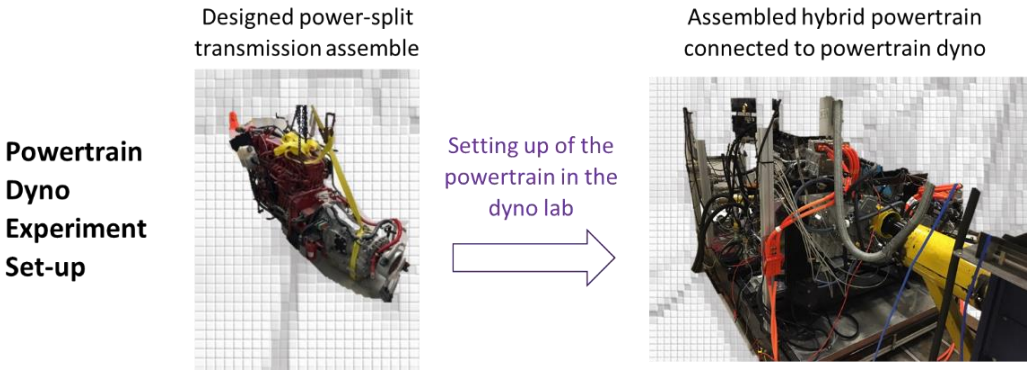

Figure 7.14 Installation of designed hybrid transmission for powertrain dyno testing

After the adequate verification of the transmission operation, the identified winning power-split design transmission is moved to the prototype vehicle chassis, as shown in Figure 7.15. We are able to get some simple tests done, but again due to time constraints, as of the time of writing this dissertation, we were not able to finish all the tests we planned. Further road test will follow to verify the performance and fuel efficiency of this prototype vehicle.

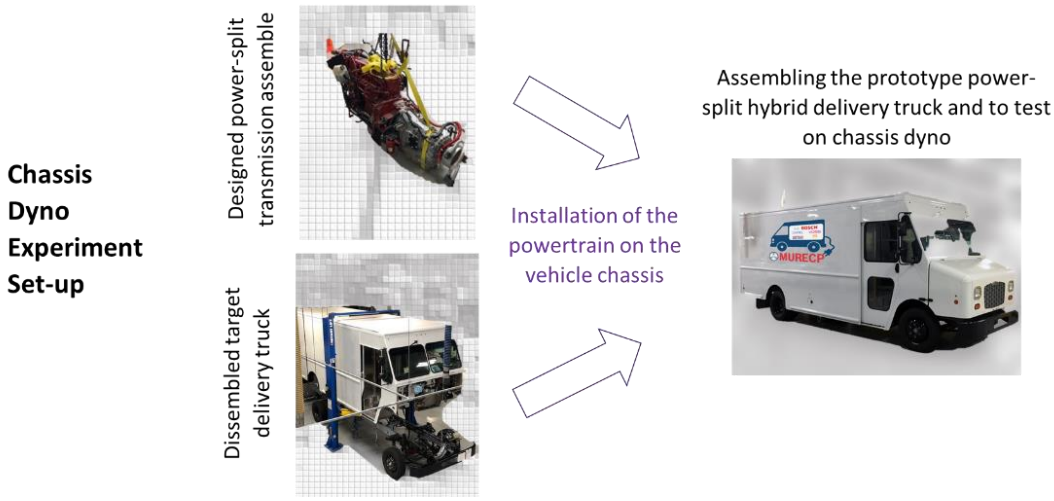

Figure 7.15 Installation of designed hybrid transmission for chassis dyno testing

7.4 HEV Control Design and Development

7.4.1 Control Structure Layout

The final architecture of the control system is shown in Figure 7.16, which is derived from the general hybrid powertrain control structure introduced in Figure *1.9* in Chapter 1. The supervisory control selects the mode and power distribution between the mechanical (engine power) and electrical (battery power) paths. The servo-loop control functions follow the commands of the supervisory control, coordinate components' torques for balancing the PG system, and ensure smooth mode transitions. The final commands for engine torque, motor torques, and clutch torques are sent from this control structure to the hardware components.

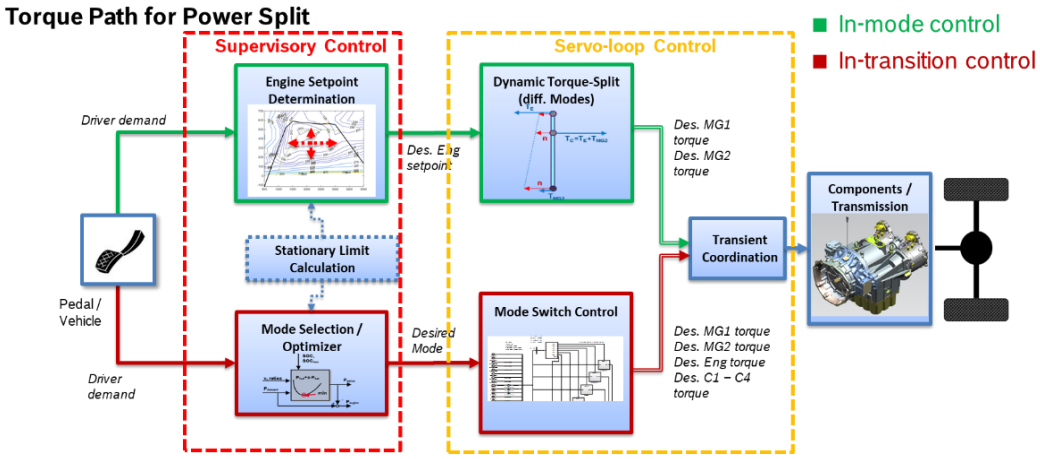

Figure 7.16 The final architecture of the control system

7.4.2 Supervisory Control Development

A rule-based control is first developed as an initial development for the supervisory control because:

1. This configuration enables opportunities to test and calibrate sub-functions such as power-split mode speed control and clutch control. For example, fixed engine power for power-split mode test become possible by just changing rule setting.
2. This control configuration allows changing testing assumption easily regarding to limitation of different testing environment. For example, the allowed

regenerative braking on the powertrain dyno is limited because of the lab hardware's limitation.

3. This control configuration enables opportunities to investigate fuel reduction benefits quantitatively. For example, benefits of power-split mode, regenerative braking, and multi-mode operation can be quantitatively analyzed.

As shown in Figure 7.17, the mode selection schedule is based on mode distribution of offline optimized simulation results on various drive cycles and conditions. The engine power is then determined, and the desired torque and speed are computed based on the powertrain system optimal operating points. These desired controls are sent to the servo-loop control, and then the motor controls further balance the PG system while satisfying the driving demand.

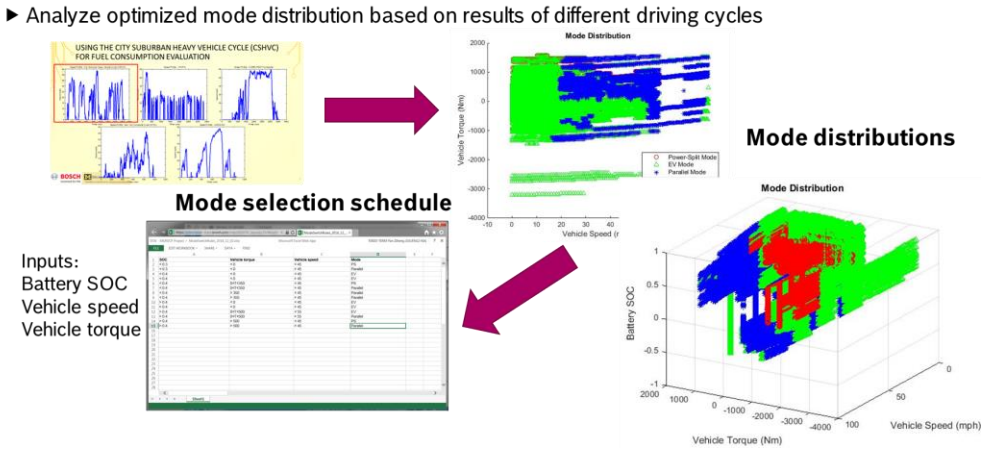

Figure 7.17 Development of the supervisory control strategy

7.5 Simulation and Testing

7.5.1 Simulation Results on Different Drive Cycles

Simulations are conducted in both MATLAB/Simulink and GT Suite environments. The GT Suite results are highlighted because they align with the experiment results more closely. The fuel consumption results discussed are corrected with the battery SOC difference between the initial and final value. The simulation results of GT Suite utilizing the developed control strategy are shown in Figure 7.18. Various battery SOC

conditions and drive cycles are investigated. The results indicate that under the charge sustaining conditions, the fuel consumption is reduced by 25 – 60%. The reduction benefit is higher when the average driving speed is lower. The results confirm that in simulations the identified optimal design is able to achieve fuel consumption reduction of over 50% in the defined CSHVC drive cycle. We also found that more fuel saving is possible when the vehicle operates in chare depletion mode. This is probably due to the fact in the charge depletion mode, the powertrain operation is more relaxed, compared with operation in the charge sustaining model.

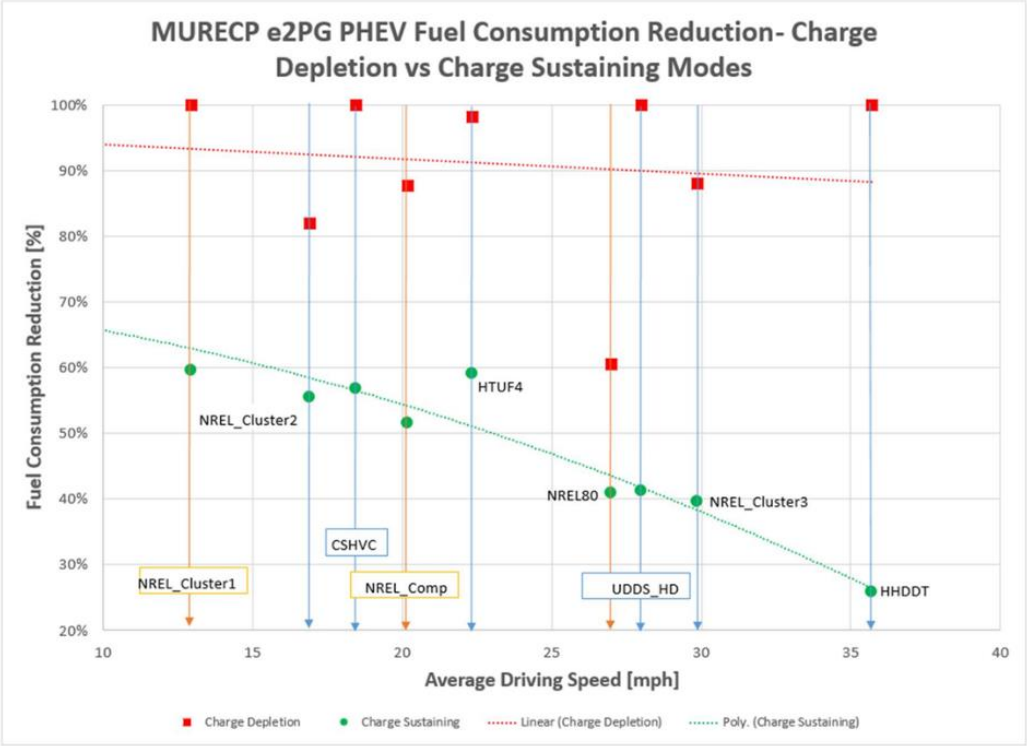

Figure 7.18 Simulation result summary in different drive cycles

7.5.2 Experimental Results

Experiments were firstly conducted on the powertrain dyno while the chassis dyno is being set up. For the purposes of project time management, coordination of multiple parties, and handling temporary limitations of the lab set-up, five function cases were defined so that experiments would proceed step-by-step:

1. Single mode operation throughout the whole drive cycle

2. No regenerative braking
3. Engine always on throughout the cycle
4. Desired engine power strategy (simplified)
5. Desired engine torque and speed strategy (simplified)

Under these simplification constraints, five control test cases were defined and shown in Table 7.1. Experiments of these defined control test cases would be performed in sequence. Within current time schedule, experiments for control test case #1 and #2 were first conducted and analyzed.

Table 7.1 Test Cases Selected of Powertrain Dyno Experiment for Designed Power-split Hybrid Powertrain

Control Test Case	Function Case Definition				
	Multi-Mode	Regenerative Braking	Engine On and Off	Optimized Engine Power	Optimized Engine Torque and Speed
1	EV only				
2	PS only				Y
3	PS only	Y			Y
4	PS only	Y	Y		Y
5	Y	Y	Y	Y	Y

The results of control test case #1 for EV mode test over the CSHVC are shown in Figure 7.19, together with the operating points of the two e-machines. The two e-machines have similar operating point distribution because the two e-machines are identical and they have very close gear ratios to the outputs. The optimization showed that the desired output torque is split close to around 52:48 ratio. Therefore, operating points of the two e-machines are similar. The energy consumption results under different environments are summarized in Figure 7.20. The closeness of the EV mode results show usefulness of the modeling development for practical implementation.

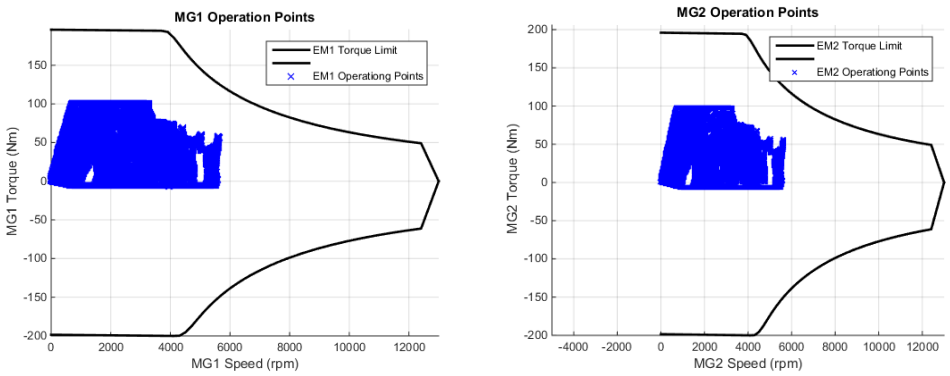

Figure 7.19 Result summary of 2-motor EV mode powertrain dyno testing

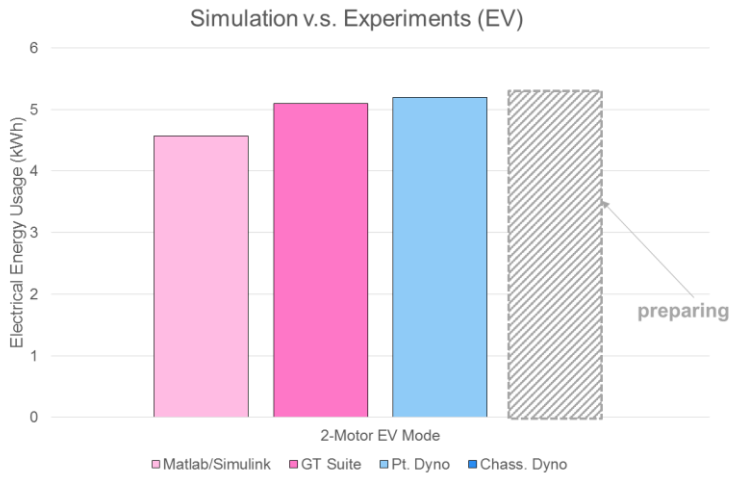

Figure 7.20 Comparison EV mode energy consumption under different environments

The results of control test case #2 for power-split mode test are shown in Figure 7.21. The corrected fuel consumption shows a fuel consumption reduction of 29.6%. These preliminary results exhibit the fuel consumption reduction categorized by the technologies of downsized engine and power-split operation. As more experiments proceed with extended control capability enabled, more fuel consumption reductions are expected.

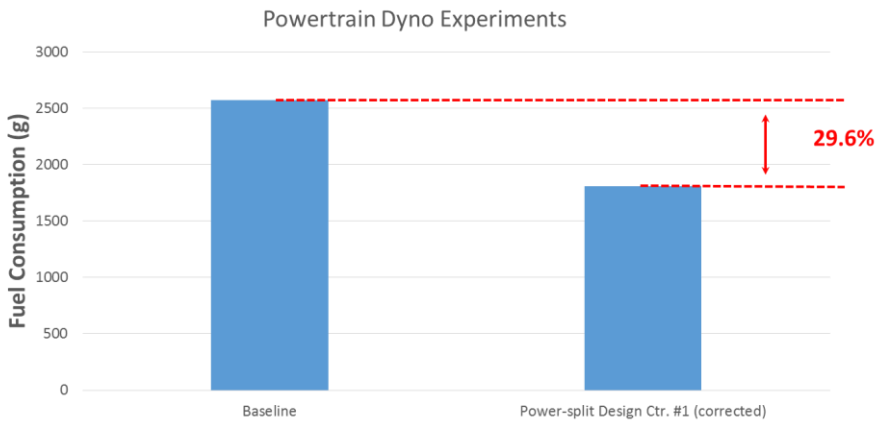

Figure 7.21 Fuel consumption result of the identified winning power-split powertrain in dyno testing

Component operating point distributions for control test case #2 are shown in Figure 7.22. Over the CSHVC, the engine operation is controlled around the desired state as highlighted in red, following closely the engine control command from the supervisory control. The engine operates freely, decoupled from the vehicle speed. This verifies the successful control design development of this prototype powertrain to have ECVT function, which is natural to many power-split hybrid powertrains. In addition, operating points of the two e-machines are also plotted in Figure 7.22. It was observed from the tests that there are some singular operating points which caused the engine operating points away from the desired control. Preliminary analysis indicate that the e-machines torque response close to zero torque or zero speed are less precise, and this phenomenon caused desired engine control less precise. Additional calibration is needed to improve the ECVT speed control accuracy and some engine control region might need to be avoided.

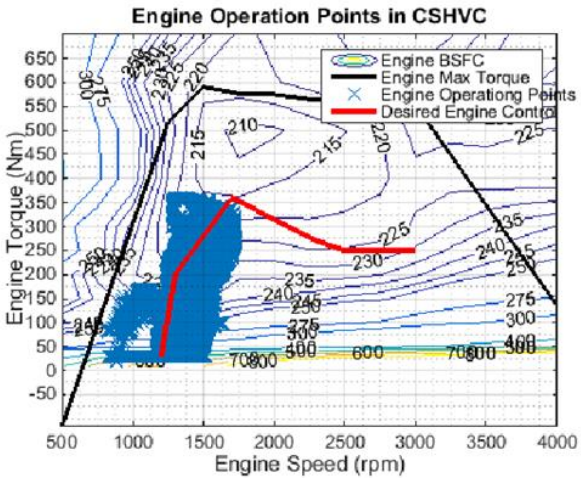

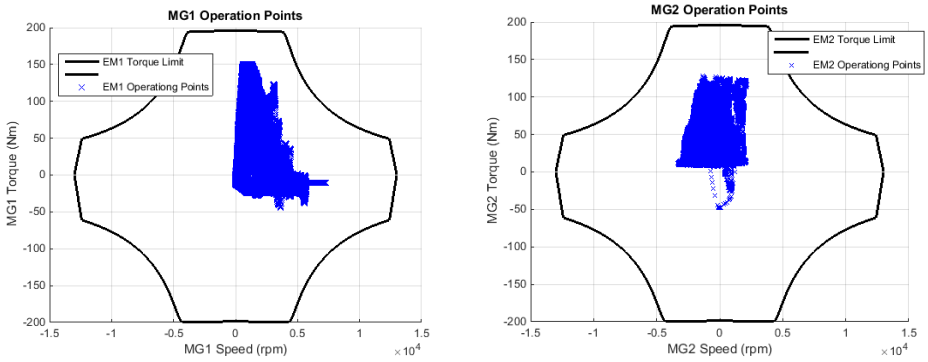

Figure 7.22 Result summary of power-split mode powertrain dyno testing

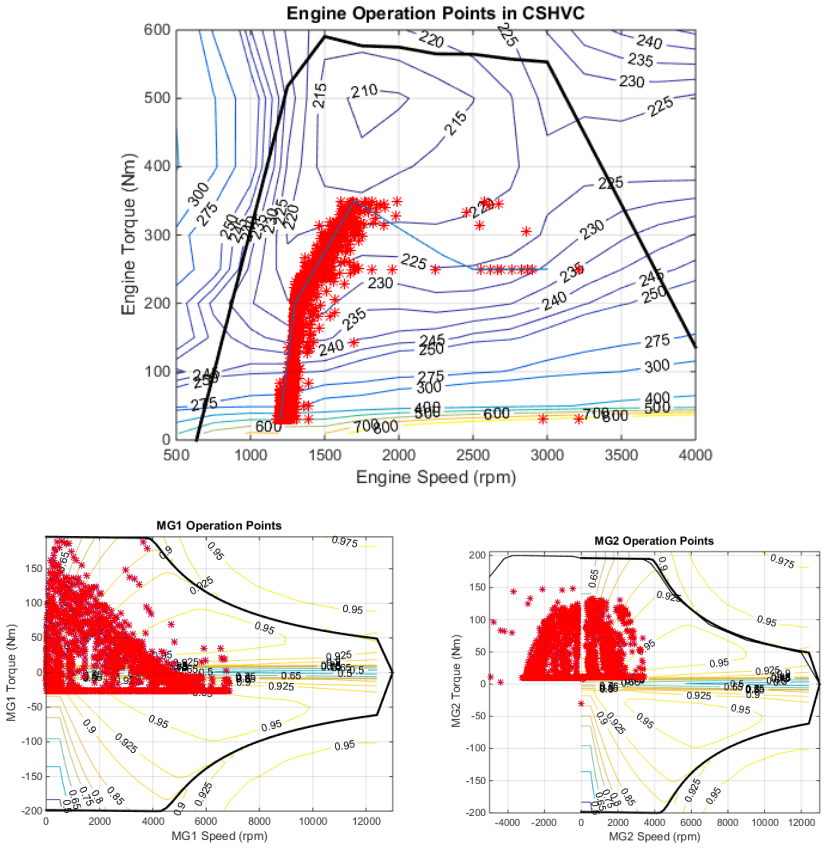

Figure 7.23 Result summary of power-split mode simulation

The simulations of the designed multi-mode power-split design with the same control strategy is performed over the CSHVC speed profile, as shown in Figure 7.23. The operating point distributions in the simulation in Figure 7.23 align with the dyno testing result in Figure 7.22. The agreement between simulation and experimental results

demonstrates the successful engineering application of the developed theory, and that the simulation models can be trusted during the design process.

7.6 Comparison and Analysis

7.6.1 Comparison between Simulation and Experimental Results

The comparison of fuel consumption between the results of simulations and experiments are summarized in Figure 7.24. Although we have not been able to have all the hardware calibration work done in time to confirm that the prototype truck indeed can achieve the projected 50% fuel reduction, the preliminary results indicate that this powertrain is projected to achieve a reduction of approximately 50% compared to the baseline model. However, availability of powertrain dyno and chassis dyno, and coordination with multiple parties to finish all the required mechanical and electrical work for the experiments made the experimental progress slower than what we would like to see. We are, nevertheless, very encouraged by the early experimental results.

These early results show that: the preliminary fuel reduction of 29.6% benefits from the downsized engine and power-split mode operation. As more experiments are in progress, tests with control technologies such as full regenerative braking, engine-off, multi-mode operation, and optimized control will be performed. The simulation results, with all the aforementioned control technologies enabled, exhibit the fuel consumption reduction of over 50%. Based on preliminary experimental results and the alignment with the simulation results, the experiments are also expected to demonstrate that this powertrain can achieve the desired target of a fuel consumption reduction of approximately 50% eventually, if all the aforementioned control technologies enabled.

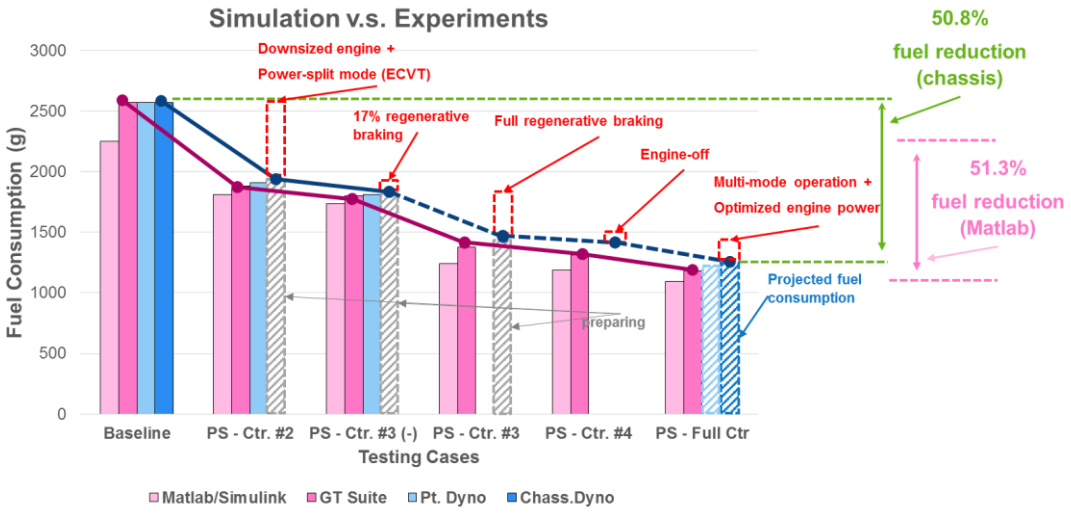

Figure 7.24 Analysis of simulations and experiments under different control settings

Based on the results summarized in Figure 7.24, fuel consumption reduction can be categorized by different technologies for this application and summarized in Figure 7.25. The technologies of downsized engine with power-split attribute and regenerative braking present the most fuel consumption reduction, with 19.5% and 25.4%, respectively. The technology of engine-off and multi-mode achieve smaller but still considerable amount of fuel consumption reduction, with 2.4% and 4%, respectively. In summary, the technologies of engine down-sizing, power-split (i.e., ECVT), and regenerative braking are the most contribution of the hybrid technology.

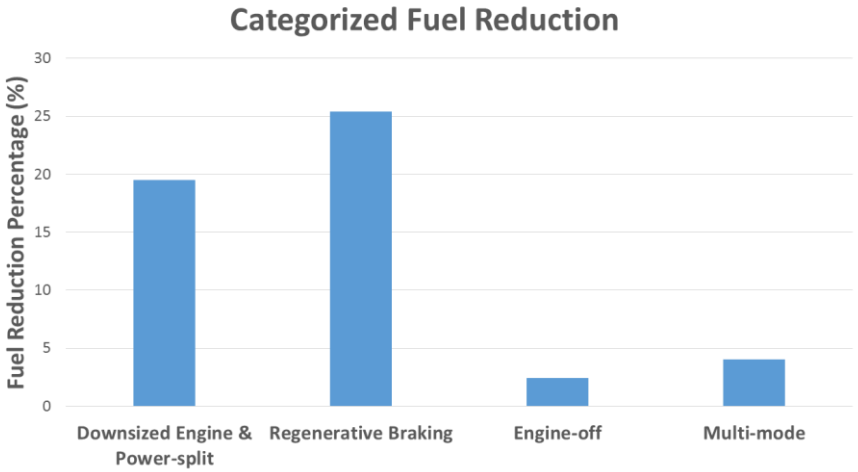

Figure 7.25 Categorized fuel reduction by different technologies

The MATLAB/Simulink results always show consistently the least fuel consumption because this simulation environment simplifies several component dynamics

and neglects a number of dynamic losses, such as, engine combustion dynamics, inverter drive dynamics, and transmission fluid dynamics. The GT Suite simulation environment show results that are considerably similar to those of the dynamometer testing results because several component dynamic losses are included through enhanced component models. Overall, the trends in fuel consumption results in simulations and experiments are well-aligned. The differences across different environments are shown in Figure 7.26. The foregoing validates the usefulness of the modeling, design, and calibration approach to design hybrid electric vehicle powertrains for the practical implementation. Again, more experiments will be performed to complete this analysis.

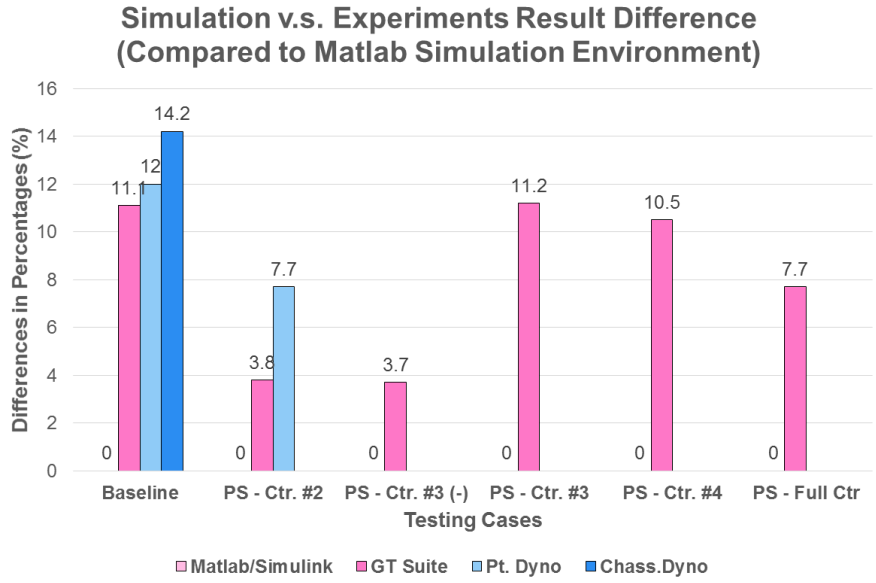

Figure 7.26 Comparison of differences among environments compared with MATLAB results

7.6.2 Analysis and Lesson Learned: PG Transmission Loss

Based on the experimental results, we found that the transmission losses are higher than expected. More tests are performed to investigate this effect and identify its root-cause. The transmission loss in terms of the transmission output shaft speed is obtained and plotted in Figure 7.27. Results were obtained by using the powertrain dyno drag the power-split transmission without any component power inputs, under various output shaft speed. The consumed power by the dynamometer is considered as the transmission loss.

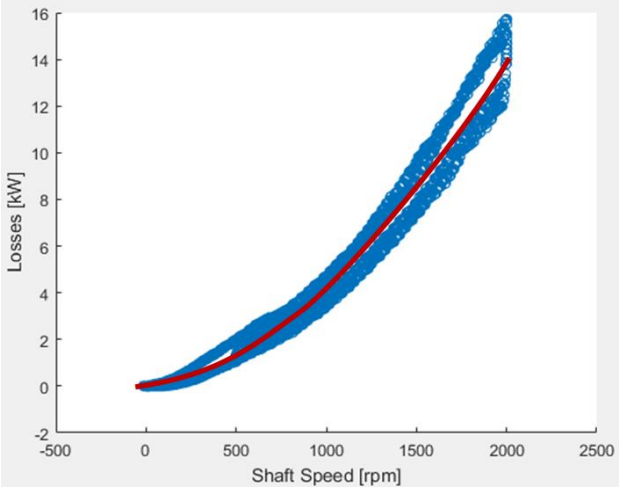

Figure 7.27 Transmission loss as functions of output shaft speed

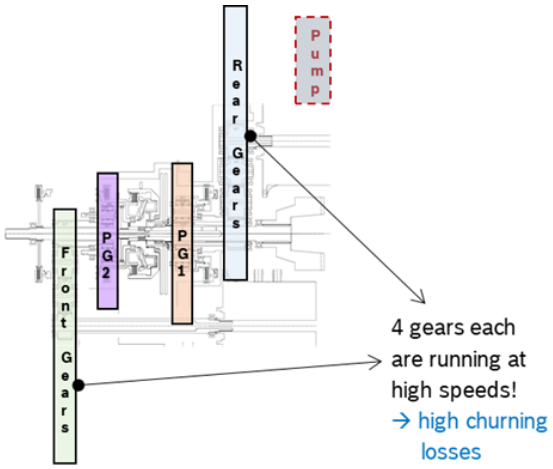

Figure 7.28 Characterizing root-cause of transmission loss

Significant transmission losses are observed from the experimental results. After analyzing the mechanical schematic in Figure 7.28 and component information, it is found that these losses were hypothesized (based both on experience and conjecture) to mainly originate from the oil pump, external gears between the e-machines and power-split transmission connections, and the PG gear losses. Our analysis indicates the oil pump is responsible for approximately 50% of the power loss.

From this experimental analysis, these transmission losses are important factors when evaluating the fuel consumption of hybrid powertrains. These losses can result in 10% fuel consumption different from results of the MATLAB simulation. On one hand, if the simulation can incorporate these losses, results will be closer to experiments for better

justification for optimal design. On the other hand, the result comparison between simulations and experiments indicate that if we maintain the same assumption (no transmission losses considered), the trends of fuel consumption reduction are similar. In summary, these transmission losses/efficiencies should be considered in the modeling and evaluation if known (e.g., gear losses); if these efficiencies are unknown (e.g., losses originate from oil pump), the assumptions of not considering these efficiencies should be maintained throughout the study to justify the fuel reduction trend.

7.7 Control Development Using Battery SOC Pulse-and-Glide Strategy

To further improve the fuel efficiency and to verify the proposed real-time control development framework proposed in this dissertation, the proposed battery SOC pulse-and-glide strategy was developed for this designed power-split hybrid powertrain. Following a design process similar to that presented in Chapter 6, the SOC PnG-based near-optimal control strategy is developed. The analyzed optimized controls of the e2PG dynamics under the vehicle command (vehicle torque and vehicle speed) is shown in Figure 7.29. The power management strategy is then developed; the integration of SOC pulse-and-glide strategy into the control design is shown in Figure 7.30.

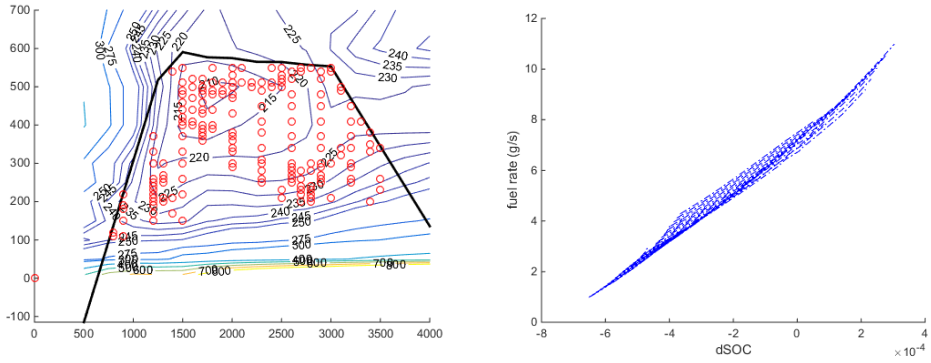

Figure 7.29 Optimized powertrain controls using SOC pulse-and-glide strategy

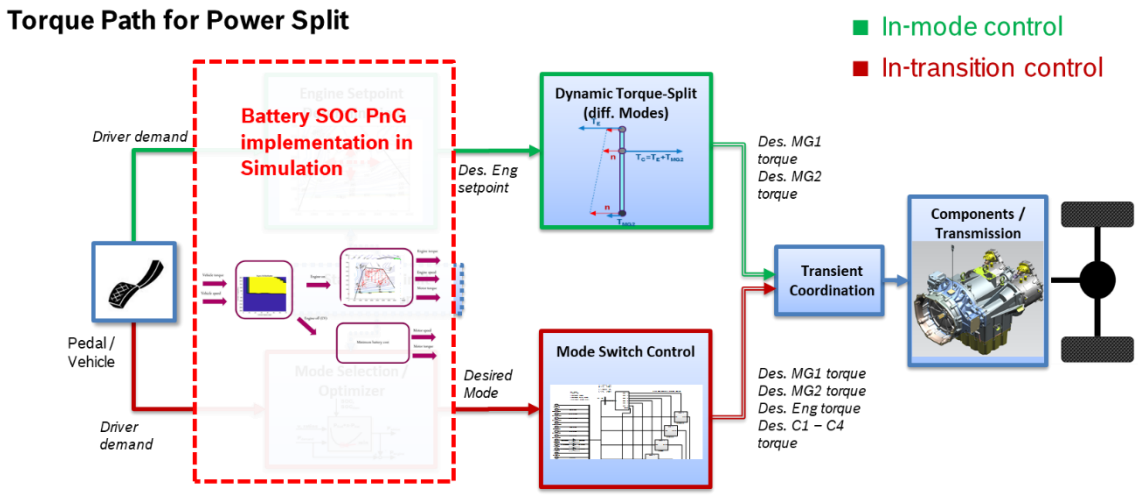

Figure 7.30 Control structure diagram adapted with SOC pulse-and-glide algorithm

The simulation results using the battery SOC pulse-and-glide control strategy are shown in Figure 7.31. Results indicate that by using the battery SOC pulse-and-glide control strategy as the real-time control strategy, the designed hybrid powertrain is able to achieved 50% fuel consumption reduction over the CSHVC drive cycle. Fuel consumption reduction benefits gained over different drive cycles are 0 – 5 % better than using the derived rule-based control.

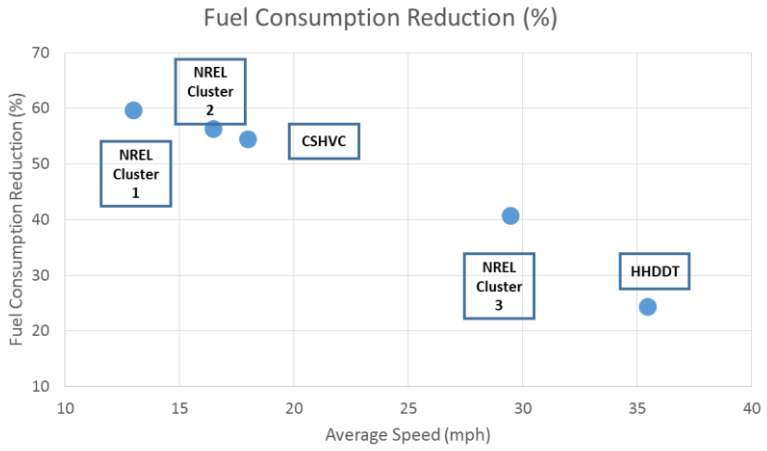

Figure 7.31 Result summary of designed multi-mode power-split hybrid powertrain using battery SOC pulse-and-glide control strategy

Because of the constraint of timeline progress and coordination of multiple parties, the hardware is not yet ready to perform tests with the designed control strategy: capability of engine-off and multi-mode operation are not ready yet. Further tests for the

implementation of this battery SOC pulse-and-glide strategy will be performed if the hardware set-up is available.

7.8 Summary of the Experimental Study

In this project, the developed design methodology for the multi-mode power-split hybrid vehicle is utilized to design a delivery truck platform. A simulation framework was also developed, using both MATLAB/Simulink and GT Suite for different simulation environments to serve different purposes in this design process. Successful experiments of first dyno tests confirmed the theoretical development on design and control of this hybrid powertrain. The development work will continue, and more research and calibration will be performed on this prototype development.

CHAPTER 8
Conclusions and Future Work

8.1 Conclusion

The dissertation work focused on the modeling, control, and design of multi-mode power-split hybrid vehicles for both the 2WD and AWD powertrains. The primary achievements include: 1. developed a design methodology for AWD power-split hybrid vehicles; 2. defined and investigated the concept of relaxed optimization for hybrid vehicles; 3. solved the relaxed optimization problem for hybrid vehicles using the MPP method; 4. generated a real-time control based on the analytical results from the MPP; 5. verified the developed framework by simulations and experiments.

A four-step systematic design methodology was developed for modeling, screening, and evaluating multi-mode power-split hybrid powertrains. A family of winning AWD designs is identified in a case study for an imaginary hybrid F-150 truck. For the identified winning design, a fuel consumption reduction of over 50% is demonstrated; the acceleration performance is also better than the conventional (ICE only) baseline.

Given an identified optimal hybrid powertrain design, the concept of relaxed optimization is further explored. Results indicate that by relaxing the vehicle speed and/or vehicle range requirements, an additional fuel consumption reduction of over 10% can be gained. As the constraint is further relaxed, more fuel consumption reduction benefits can be achieved; this benefit saturates eventually saturates (in our case study, at about 7mph speed relaxation).

A framework for using the MPP method is developed, to solve high DOF optimization problem of the HEV and identify the analytical solution of the control problem. The analytical results were found to be close to numerical results from DP.

By understanding the distribution of optimal control actions based on the analytical and numerical results, the framework for a systematic real-time control strategy was developed. The optimal control points were analyzed and obtained. Real-time control strategy was constructed based on the obtained optimized controls.

We were able to secure research funding from the USDOE to build a prototype truck, funded project MURECP. The powertrain of this prototype vehicle was designed based on the design process developed in this dissertation. Simulation results were conducted, and limited experimental results were obtained on the engine dyno and the chassis dyno. The preliminary experimental results indicate that the predicted fuel consumption reduction of 50% can be achieved. However, this requires significant additional implementation on real hardware. Due to the challenges in scheduling resources to conduct experiments, we do not yet have all the functions implemented (e.g., regen braking and multi-mode switching).

8.2 Short-Term Future Work

8.2.1 Experiments on the MURECP Prototype Vehicle

The control implementation on the designed prototype multi-mode power-split hybrid vehicle will be continued. The first next step is to implement the mode shift control logic on the test vehicle.

The experiments on the powertrain dyno and chassis dyno still ongoing. Fuel economy with different refined and implemented control cases will be measured as these additional low-level control functions become available. Fuel economy under different drive cycles will also be verified through these experiments.

8.2.2 Experiments and Analysis for Relaxed Optimization

Once the assembled vehicle is completed and ready for road test, the experiments for different levels of relaxation will be performed. Results of the simulations and experiments will be compared and to verify the concept. Effects of different relaxation of energy buffer will be analyzed.

8.2.3 Performance Robustness and Sensitivity for Battery SOC Pulse-and-Glide

The proposed battery SOC pulse-and-glide strategy will be further investigated, to understand effects of the uncertainty of the driving power distribution. The sensitivity of the resulted fuel efficiency performance and the control robustness will be analyzed.

8.3 Long-Term Future Work

8.3.1 Expansion of Design Framework to Beyond Fuel Economy

The established design framework will be extended to incorporate more performance indexes as required, including NO_x emission and cost. These added indexes are useful for determining designs for additional considerations. Additional dynamics for NO_x emissions result in additional DOFs to the problem; models for cost payback add complexity for modeling. To address these considerations, the developed design framework requires extensive models that incorporates those different dynamics and adapted methods to solve the optimization problem efficiently.

8.3.2 Expansion of Optimization and Control Frameworks to Control Planning of Connected and Automated Vehicles

The proposed framework of defining, formulating, and solving the relaxed optimization will be extended to a speed-trajectory planning problem for connected and automated vehicles. With information of surrounding vehicles, traffic lights, and speed limit available, the speed-trajectory planning for vehicles is a non-convex, nonlinear, and high-dimensional problem. Using the developed framework, constraints of all the information of connectivity can be included; and the planning problem for hybrid vehicles can be solved, which is difficult or time-consuming to solve using existing methods.

Route planning problem considering minimum fuel will be addressed by utilizing the control development framework. With consideration of fuel consumption minimization, the route planning, especially for HEVs, includes optimization for both route selection and powertrain control. Existing methods to solve these problems commonly use an average fuel consumption model, which simplifies the problem by neglecting the

powertrain dynamics. With the control developed framework, the powertrain dynamics can incorporated. The planning problem then can provide better justified results with minimizing fuel consumption considered.

APPENDIX A Calculation of Average Acceleration and Gradeability Dynamics Analysis

Appendix A.1 Calculation of the Average Acceleration

The 0 – 60 mph launching is divided into n speed grid evenly, as shown in Figure A.1.

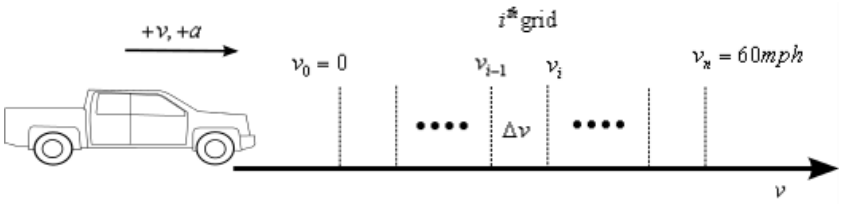

Figure A.1 Speed grid division for evaluation of the average acceleration

For each speed grid, the velocity difference Δv of the initial value and the final value is known. In the i^{th} speed grid, the time for this speed grid t_i can be calculated by Eq. (A.1),

$$t_i = \frac{v_i - v_{i-1}}{a_i} = \frac{\Delta v}{a_i} \tag{A.1}$$

where a_i is the acceleration in this grid. The total time used for 0 – 60 mph launching is calculated in Eq. (A.2).

$$t_{tot} = \sum_{i=1}^{n} t_i = \Delta v \sum_{i=1}^{n} \frac{1}{a_i} \tag{A.2}$$

By defining the average acceleration of the launching period shown in Eq. (A.3). The average acceleration relates a_i by Eq. (A.4).

$$\bar{a} = \frac{v_n - v_0}{t_{tot}} = \frac{n \cdot \Delta v}{t_{tot}} \tag{A.3}$$

$$\bar{a} = \frac{n \cdot \Delta v}{t_{tot}} = \frac{n \cdot \Delta v}{\Delta v \sum_{i=1}^{n} \frac{1}{a_i}}$$
$$\Rightarrow \bar{a} = \frac{n}{\sum_{i=1}^{n} \frac{1}{a_i}} \tag{A.4}$$

Appendix A.2 Model of Vehicle Dynamics for the Gradeability Tests

The gradeability tests in Figure A.2 are for a fully loaded vehicle driving on a slope with angle of θ. A free-body diagram for the tow-vehicle motion is shown in Figure A.3.

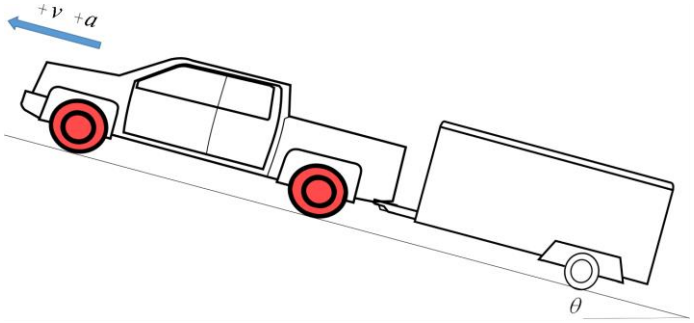

Figure A.2 Gradeability tests of a full-loaded AWD tow-vehicle

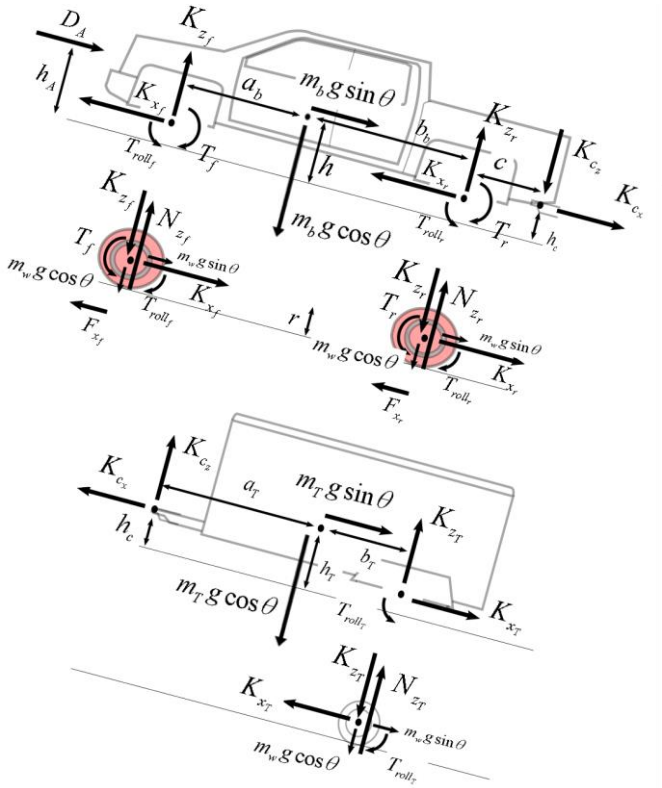

Figure A.3 Free-body diagram for the tow-vehicle motion on a slope

The tow-vehicle has a trailer with weight of m_T. K_{cz} is the vertical internal force between the vehicle and the trailer body, and K_{cx} is that internal force in the longitudinal direction. Other symbols are defined in the same way as those in Chapter 2. The subscripts T refers to the front and rear tire reaction forces/torques respectively. The gravitational constant is g, the aerodynamic force is D_A, T is the axle output torque, K_z is the vertical internal force between the wheels and body, K_x is the longitudinal internal force between the wheels and body, N_z is the tire reaction force in the vertical direction, and F_x is the tire reaction force in the longitudinal direction. The subscripts F and R refer to the front and rear tire reaction forces/torques respectively.

Longitudinal dynamics and rotational motion dynamics of the vehicle body, the trailer, trailer wheels, front wheels, and rear wheels are given in Eq. (A.5) – (A.19).

$$K_{x_f} + K_{x_r} - D_A - m_b g \sin\theta - K_{c_x} = m_b a \tag{A.5}$$

$$K_{z_f} + K_{z_r} - K_{c_z} = m_b g \cos\theta \tag{A.6}$$

$$\begin{aligned} &-K_{z_f} a_b + K_{z_r} b_b - D_A \left(h_A - h\right) \\ &-\left(K_{x_f} + K_{x_r}\right)\cdot\left(h - r\right) \\ &+T_f - T_{roll_f} + T_r - T_{roll_r} \\ &-K_{c_z}\left(b + c\right) + K_{c_x}\left(h_A - h_T\right) = 0 \end{aligned} \tag{A.7}$$

$$T_f - F_{x_f} r - T_{roll_f} = I_w \dot{\omega}_f \tag{A.8}$$

$$F_{x_f} - K_{x_f} = m_w a \tag{A.9}$$

$$N_{z_f} - K_{z_f} - m_w g \cos\theta = 0 \tag{A.10}$$

$$T_r - F_{x_r} r - T_{roll_r} = I \dot{\omega}_r \tag{A.11}$$

$$F_{x_r} - K_{x_r} = m_w a \tag{A.12}$$

$$N_{z_r} - K_{z_r} - m_w g \cos\theta = 0 \tag{A.13}$$

$$K_{c_x} - m_T g \sin\theta - K_{x_T} = m_T a \tag{A.14}$$

$$K_{c_z} + K_{z_T} = m_T g \cos\theta \tag{A.15}$$

$$\begin{aligned} &K_{z_T} b_T - K_{x_T}\cdot\left(h_T - r\right) - T_{roll_T} \\ &-K_{c_z} a_T + K_{c_x}\left(h_T - h_c\right) = 0 \end{aligned} \tag{A.16}$$

$$F_{x_T} r - T_{roll_T} = I_w \dot{\omega}_T \tag{A.17}$$

$$K_{x_T} - F_{x_T} = m_w a \tag{A.18}$$

$$N_{z_T} - K_{z_T} - m_w g \cos\theta = 0 \tag{A.19}$$

The maximum driving forces for the three cases (i.e., AWD, FWD, and RWD) in the gradeability tests are shown in Table A.1.

Table A.1 Maximum driving forces

Hybrid Vehicle Drive-train Designs	Max Tire Forces
AWD	$F_{AWD\_\max} = N_{z_f} \cdot \mu_{tire} + N_{z_r} \cdot \mu_{tire}$
FWD	$F_{FWD\_\max} = N_{z_f} \cdot \mu_{tire}$
RWD	$F_{RWD\_\max} = N_{z_r} \cdot \mu_{tire}$

APPENDIX B Case Studies of Relaxed Optimization on Relaxing Vehicle Range and Battery SOC

Additional case studies on other independent constraints (range difference and battery SOC) is provided in this appendix. Case set-up for constraints relaxation is summarized in Table B.1.

Table B.1 Extended Constraint Bounds for Different Independent Constraint Case Studies

	Vehicle Speed (mph)	Vehicle Position Offset (m)	Battery SOC (%)
Constraint Range (Case 1: Speed)	±2 ~ ±10	±50	40 – 60

Figure B.1 shows the fuel reduction benefits when varying the range difference relaxation only. Results show that, for conventional vehicle, larger range difference (when larger than 50m) does not result in significant fuel reduction. The fuel reduction benefit saturates when the range difference is greater than 50m, where the speed constraint starts to dominate the operation. Similar trend is observed for the HEV case. The benefit effect of the range difference is less sensitive compared to the speed bound relaxation, because the range difference is the integration results of the speed differences thus the effect on fuel rate is smoothed out.

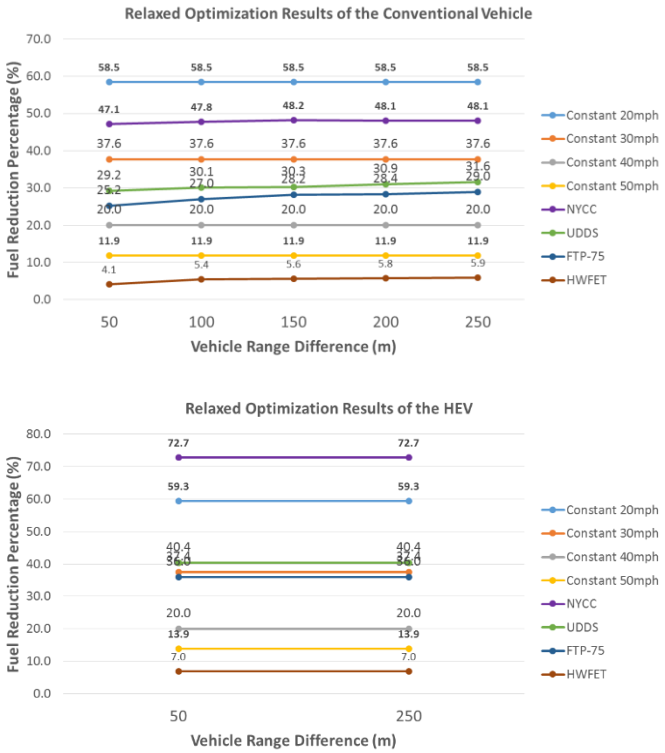

Figure B.1 Percentage of fuel consumption reduction under varying range constraints in different driving scenarios

Figure B.2 shows the fuel reduction benefits when varying the battery SOC relaxation only. The resulted fuel reduction shows steady values with enlarged battery SOC range. The benefits saturate even when the SOC range enlarged more than 20% range, as long as the battery energy range is enough to provide the buffer to absorb power from engine & braking, and enough to discharge with the help of engine. Thus a larger battery energy/SOC range is not necessary.

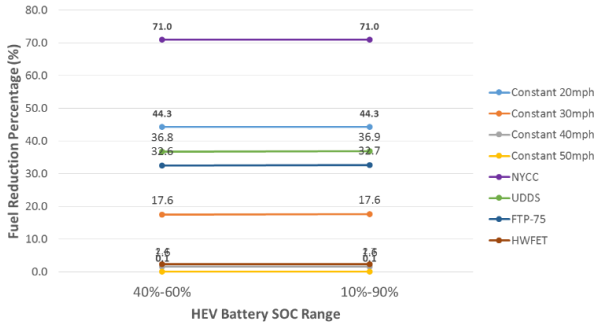

Figure B.2 Percentage of fuel consumption reduction of HEV for varying battery SOC constraint values under different driving scenarios

APPENDIX C Application Case Study of Battery SOC Pulse-and-Glide Strategy – IEEE VTS Challenge

The powertrain system optimal strategy derived from the battery SOC pulse-and-glide is also utilized in the participation of the 2018 IEEE VTS Challenge as a case study implementation. This competition focuses on the energy management of a Range Extender Electric Vehicle, the Chevrolet Volt. The aim is to develop a robust Energy Management Strategy to minimize the fuel consumption and the battery charging cost as shown in Eq. (C.1). A battery SOC pulse-and-glide strategy is developed and implemented. Simulation results show that the designed control approach leads to over 10% combined cost reduction on average, compared to the original control. The resulted global combined score is 6.641 US$, ranking No.5 globally among the 52 competitors in the 2018 IEEE VTS Motor Vehicles Challenge.

$$\min \quad J = \$_{gas} \cdot \sum_{k=0}^{N-1} \dot{m}_f^* (k) + \$_{charge} \cdot \sum_{k=0}^{N-1} \Delta SOC(k) \tag{C.1}$$

Appendix C.1 Modeling and Control Development

The 2012 Chevrolet Volt powertrain with all 4 operating modes is shown in Figure C.1. The complete dynamics for all 4 modes are shown in Eqs. (C.2) – (C.5).

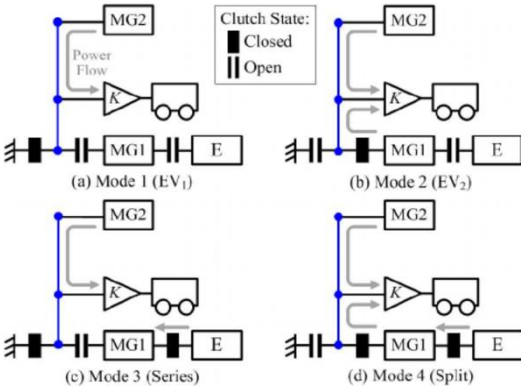

Figure C.1 Lever diagram of the 2012 Chevrolet Volt powertrain

mode 1:

$$\begin{aligned} \dot{\Omega} &= \dot{\omega}_v = \frac{1}{R+S} \cdot \dot{\omega}_{em2}, \\ A^{-1} &= I_v + \left(R+S\right)^2 \cdot I_{em2}, \\ T &= \left(R+S\right) \cdot T_{em2} - T_v \end{aligned} \tag{C.2}$$

mode 2:

$$\dot{\Omega} = \begin{bmatrix} \dot{\omega}_{em1} \\ \dot{\omega}_v \\ \dot{\omega}_{em2} \\ 0 \end{bmatrix},$$

$$A^{-1} = \begin{bmatrix} I_{em1} & 0 & 0 & -R \\ 0 & I_v & 0 & R+S \\ 0 & 0 & I_{em2} & -S \\ -R & R+S & -S & 0 \end{bmatrix}, \tag{C.3}$$

$$T = \begin{bmatrix} T_{em1} \\ T_v \\ T_{em2} \\ F_{PG} \end{bmatrix}$$

mode 3:

$$\begin{aligned} \dot{\Omega} &= \dot{\omega}_v = \frac{1}{R+S} \cdot \dot{\omega}_{em2}, \\ A^{-1} &= I_v + \left(R+S\right)^2 \cdot I_{em2}, \\ T &= \left(R+S\right) \cdot T_{em2} - T_v \\ T_e &= -T_{em1} \end{aligned} \tag{C.4}$$

mode 4:

$$\dot{\Omega} = \begin{bmatrix} \dot{\omega}_e \\ \dot{\omega}_v \\ \dot{\omega}_{em2} \\ 0 \end{bmatrix},$$

$$A^{-1} = \begin{bmatrix} I_e + I_{em1} & 0 & 0 & -R \\ 0 & I_v & 0 & R+S \\ 0 & 0 & I_{em2} & -S \\ -R & R+S & -S & 0 \end{bmatrix}, \qquad \text{(C.5)}$$

$$T = \begin{bmatrix} T_e + T_{em1} \\ T_v \\ T_{em2} \\ F_{PG} \end{bmatrix}$$

Utilizing the same analysis methodology shown earlier in Chapter 8, the powertrain system optimality is analyzed and demonstrated in Figure C.2. Again, the battery SOC pulse-and-glide control strategy is used.

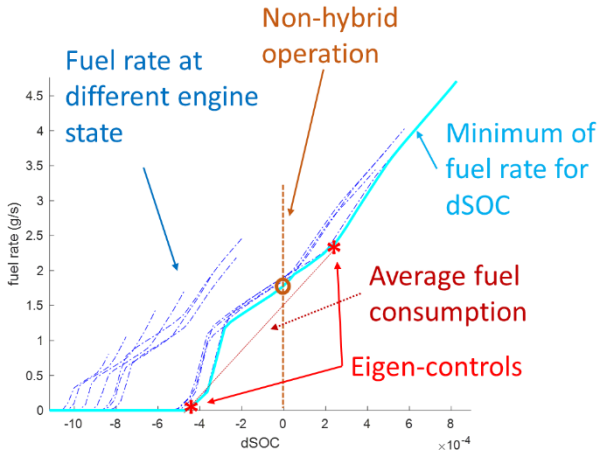

Figure C.2 Battery SOC pulse-and-glide analysis for the 2012 Chevrolet Volt powertrain

Appendix C.2 Simulation Results

Numerical simulations are conducted with different drive cycles and the results are compared with those of the original control in the Autonomie model. The results for two

different initial SOC (60% and 40%) for the original control are shown in Table C.1 and Table C.2, while the results of the proposed battery SOC pulse-and-glide strategy are shown in Table C.3 and Table C.4, which reports fuel consumption, SOC usage, and the combined cost. The comparison between the proposed battery SOC pulse-and-glide and the original control is shown in Table V. The results show that over 10% combined cost reduction as shown in Table C.5.

Table C.1 Results of the Original Autonomie Control (Initial SOC = 60%)

Tested Cycles	Fuel Consumption (g)	Usage of SOC	Combined Cost
UDDS	0	15.5%	0.3393
US06	0	28.2%	0.6187
FTP-75	0	23.9%	0.5238
WLTC	0.2488	30.0%	0.8332

Table C.2 Results of the Original Autonomie Control (Initial SOC = 40%)

Tested Cycles	Fuel Consumption (g)	Usage of SOC	Combined Cost
UDDS	0.1551	10.6%	0.3565
US06	0.4173	9.9%	0.6029
FTP-75	0.4161	9.7%	0.5432
WLTC	0.7868	9.0%	0.8222

Table C.3 Results of the Proposed Battery SOC PnG Strategy (Initial SOC = 60%)

Tested Cycles	Fuel Consumption (g)	Usage of SOC	Combined Cost
UDDS	0.2619	5.9%	0.3165
US06	0.9594	-11.1%	0.5199

FTP-75	0.6628	-2.5%	0.4732
WLTC	1.0998	-5.3%	0.7576

Table C.4 Results of the Proposed Battery SOC PnG Strategy (Initial SOC = 40%)

Tested Cycles	Fuel Consumption (g)	Usage of SOC	Combined Cost
UDDS	0.4376	-1.6%	0.3133
US06	0.9693	-11.5%	0.5191
FTP-75	0.8677	-10.2%	0.4656
WLTC	1.2804	-12.8%	0.7374

Table C.5 Combined Cost Reduction for the Proposed Battery SOC Pulse-and-Glide Strategy Compared to the Original Autonomie Control

Tested Cycles	Initial SOC = 60%	Initial SOC = 40%
UDDS	6.70%	12.11%
US06	15.96%	13.91%
FTP-75	9.66%	14.29%
WLTC	9.07%	10.32%

The engine operating points under the two control strategies are compared and shown Figure C.3 and Figure C.4.

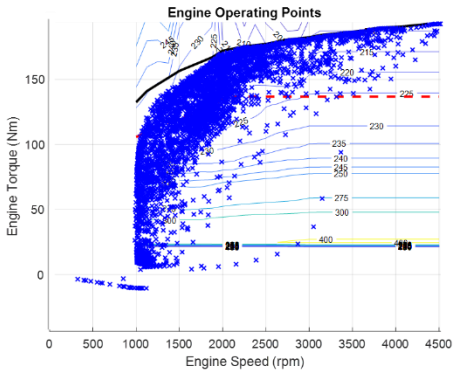

Figure C.3 Engine operating points under the original control

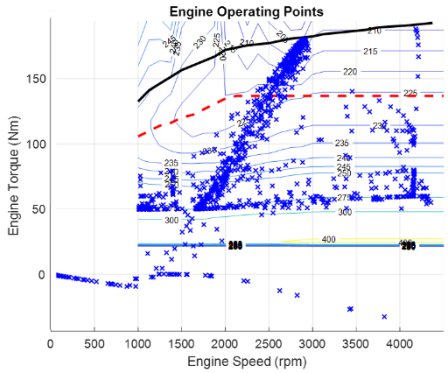

Figure C.4 Engine operating points under the proposed battery SOC pulse-and-glide strategy

Under the original control in the Autonomie software, the engine operating points in Figure C.3 are more distributed along the best brake specific fuel consumption (BSFC) line (highlighted in red). Under the proposed battery SOC pulse-and-glide strategy, the engine operating points in Figure C.4 are distributed differently. When accounting for the losses of the motor(s) and battery, operating the engine along the best BSFC line is not necessarily system optimal. The SOC pulse-and-glide strategy is able to consider all the losses, with the optimal system controls. Therefore, the overall fuel rate and combined cost are reduced.

APPENDIX D Three-Dimensional Demonstration of Multi-Mode Power-Split Hybrid Powertrain Schematics

A with 3D-printing demo is developed as a platform for an efficient validation of design schematic and control strategy development. The motivation is to establish a reconfigurable platform that can emulate multi-mode power-split hybrid powertrain mechanism using two PG sets given all possible design schematics. With this emulation technique, the feasibility to operate this powertrain can be confirmed. This demo enables:

1. collocations of powertrain components;
2. emulation of operating status;
3. emulation of mode-switch.

The design demo uses a designed PG from a typical PG set shown in Figure D.1 and developed a 3D printing PG set shown in Figure D.2.

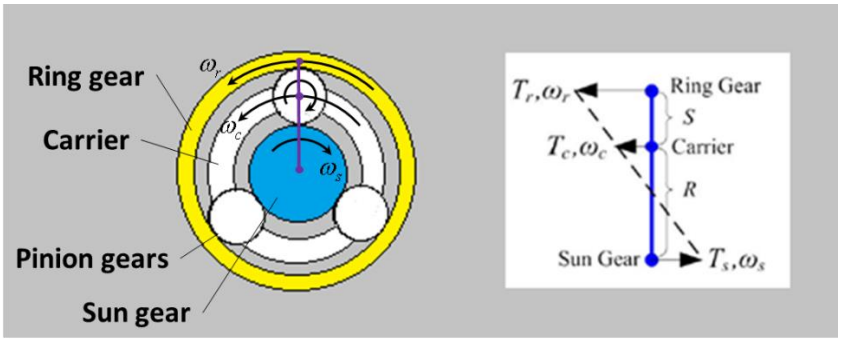

Figure D.1 Diagram of a typical PG set

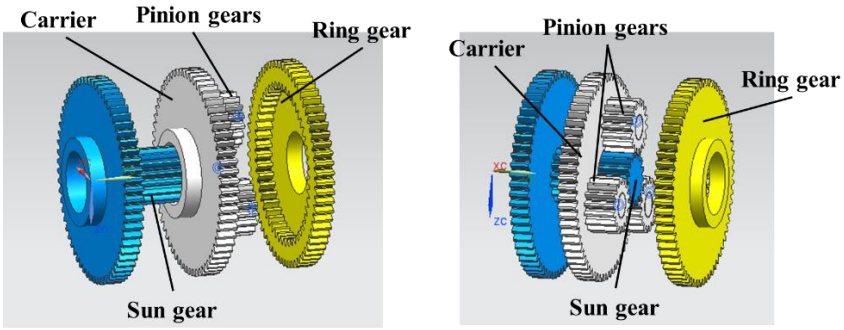

Figure D.2 3D printing gear from a typical PG set

To emulate the clutch connections between the two PG set, each PG set is connected a longitudinal rotational shaft as an output shaft. The connection between each gear is emulated by clutch connection between each shaft. A PG set with output shaft connection is created and assembled, as shown by the 3D printing design drawing (on the left) in Figure D.3, together with the manufactured mechanical gear set (on the right).

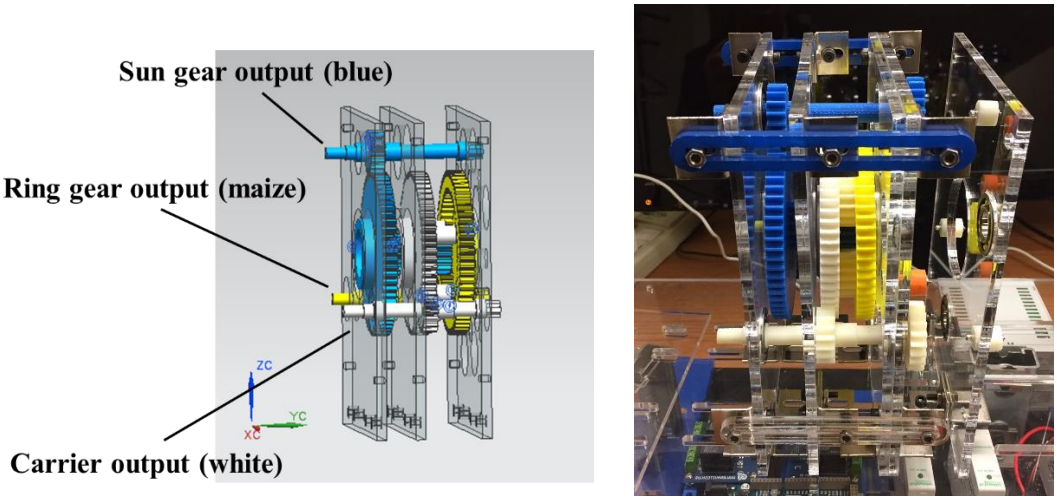

Figure D.3 The 3D printing design and the manufactured gear set

By using this PG set-up, a 2PG power-split demo is set up, which enables connection with clutches between the 2PG set and collocation with electric motors. Using an example of shown in Figure D.4 (but not limited to this example), the emulated drawing using the designed demo is shown in Figure D.5. The manufactured set-up of the corresponding design is shown in Figure D.6.

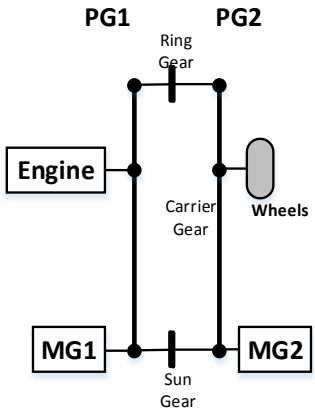

Figure D.4 An exemplary design of a 2PG power-split hybrid

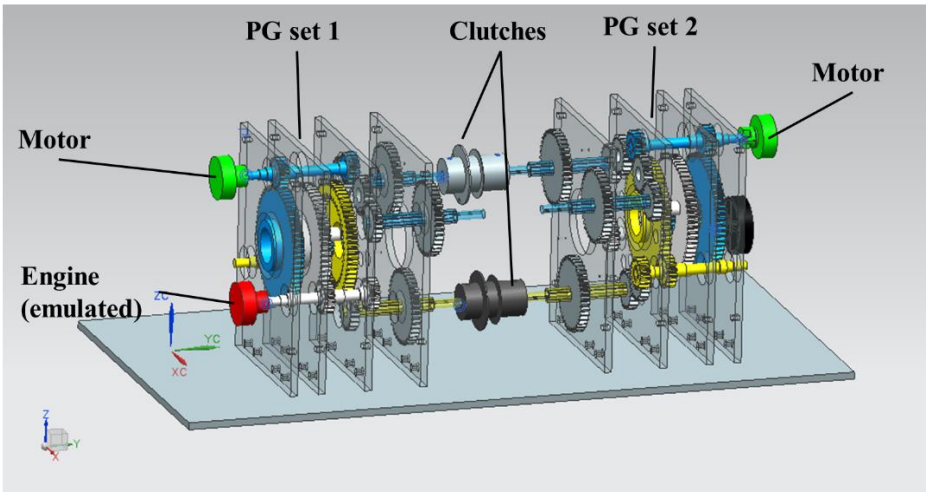

Figure D.5 The designed power-split demo that emulates the design in Figure D.4

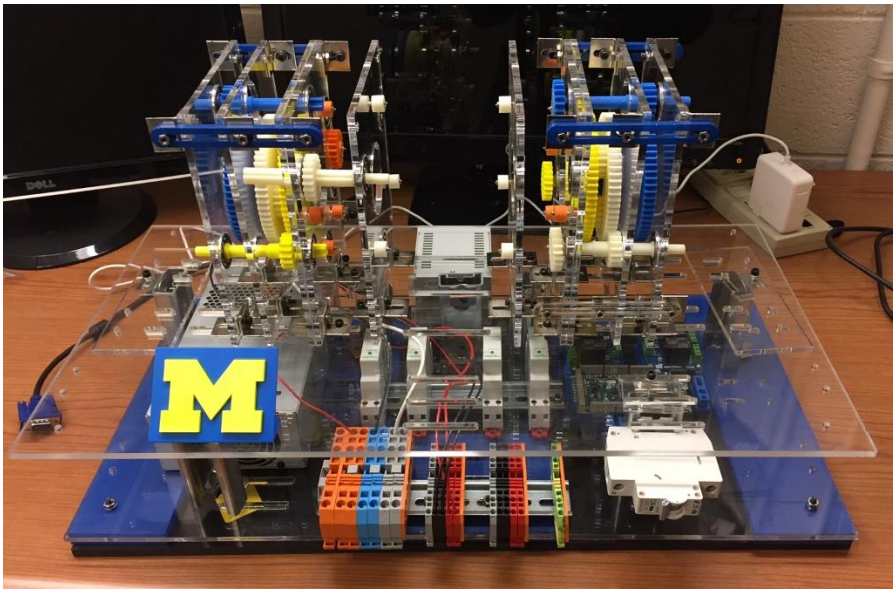

Figure D.6 The manufactured set-up of the design in Figure D.5

The above designed power-split demo can emulate 2PG power-split designs with controls through Simulink models on a PC. The electric motors and clutches communicate with the PC through Arduino board and controlled by controller in Simulink. This hardware-in-loop (HIL) set-up is used to test the speed mode control and mode shift operation for a given power-split design. It is able to emulate the powertrain operation through a down-scale level to test and confirm a realistic feasibility of a designed power-split hybrid powertrain.

BIBLIOGRAPHY

[1] T. I. C. o. C. Transportation, "Chart library: Passenger vehicle fuel economy," [Online]. Available: www.theicct.org/chart-library-passenger-vehicle-fuel-economy, 2018.

[2] "The Safer Affordable Fuel-Efficient (SAFE) Vehicles Rule for Model Years 2021-2026 Passenger Cars and Light Trucks - Proposed Rule," N. H. T. S. A. a. E. P. Agency, ed., [Online]. Available: www.federalregister.gov, 2018.

[3] "2017–2025 Model Year Light-Duty Vehicle GHG Emissions and CAFE Standards: Supplemental Notice of Intent," N. H. T. S. Administration, ed., [Online]. Available: www.federalregister.gov, 2011.

[4] "Fuel Economy Guide - Model Year 2018," United States Environmental Protection Agency. [Online]. Available: https://www.fueleconomy.gov/, 2018.

[5] Statista, "Light vehicle retail sales in the United States from 1978 to 2018," [Online]. Available: www.statista.com/statistics/199983/us-vehicle-sales-since-1951/, 2019.

[6] Statista, "U.S. light truck retail sales from 1980 to 2018," [Online]. Available: www.statista.com/statistics/199980/us-truck-sales-since-1951/, 2019.

[7] "Performance Requirements for Determining Tow-Vehicle Gross Combination Weight Rating and Trailer Weight Rating," SAE International, 2016.

[8] SAE, "SAE Standard J1952: All-Wheel Drive Systems Classification," Society of Automotive Engineers International.

[9] "2014 Acura RLX Sport Hybrid SH-AWD: Powertrain," Honda Motor Co.. Available: http://news.honda.com/newsandviews/article.aspx?id=7504-en. [Online. Accessed 2016]. 2013.

[10] C. Csere, "2016 Toyota RAV4 Hybrid," Available: http://www.caranddriver.com/reviews/2016-toyota-rav4-hybrid-first-drive-review. [Online. Accessed 2016]. 2015.

[11] B. Halvorson, "2016 Lexus RX Hybrid F Sport First Drive," Available: http://www.greencarreports.com/news/1099941_2016-lexus-rx-hybrid-f-sport-first-drive. [Online. Accessed 2016]. 2015.

[12] "United States Hybrid and Plug-in Hybrid Sales," HybridCars.com. [Online]. Available: http://www.hybridcars.com/december-2017-dashboard/, 2017.

[13] T. Burress, S. Campbell, C. Coomer, C. Ayers, A. Wereszczak, J. Cunningham, L. Marlino, L. Seiber, and H. Lin, *Evaluation of the 2010 Toyota Prius hybrid synergy drive system*, Oak Ridge National Lab.(ORNL), Oak Ridge, TN (United States). Power …, 2011.

[14] X. Zhang, H. Peng, and J. Sun, "A near-optimal power management strategy for rapid component sizing of power split hybrid vehicles with multiple operating modes," in American Control Conference (ACC), 2013, pp. 5972-5977.

[15] W. Caihao, Z. Xiaowu, and S. Jing, "Adaptive model predictive control for hybrid rlectric vehicles power management," in Control Conference (CCC), 2013 32nd Chinese, 2013, pp. 7756-7761.

[16] J. Liu, and H. Peng, "Control optimization for a power-split hybrid vehicle," in American Control Conference, 2006, pp. 6 pp.-6 pp.

[17] N. Jalil, N. A. Kheir, and M. Salman, "A rule-based energy management strategy for a series hybrid vehicle," in American Control Conference, 1997, pp. 689-693.

[18] A. Sciarretta, M. Back, and L. Guzzella, "Optimal control of parallel hybrid electric vehicles," *IEEE Transactions on Control Systems Technology*, vol. 12, no. 3, pp. 352-363, 2004.

[19] S. Stockar, V. Marano, G. Rizzoni, and L. Guzzella, "Optimal control for plug-in hybrid electric vehicle applications," in American Control Conference (ACC), 2010, pp. 5024-5030.

[20] C.-C. Lin, H. Peng, J. W. Grizzle, and J.-M. Kang, "Power management strategy for a parallel hybrid electric truck," *IEEE Transactions on Control Systems Technology*, vol. 11, no. 6, pp. 839-849, 2003.

[21] "Recommended Practice for Measuring the Exhaust Emissions and Fuel Economy of Hybrid-Electric Vehicles, Including Plug-in Hybrid Vehicles," SAE International, 2010.

[22] K. McDonough, I. Kolmanovsky, D. Filev, D. Yanakiev, S. Szwabowski, and J. Michelini, "Stochastic dynamic programming control policies for fuel efficient in-traffic driving." pp. 3986-3991.

[23] K. McDonough, I. Kolmanovsky, D. Filev, D. Yanakiev, S. Szwabowski, and J. Michelini, "Stochastic dynamic programming control policies for fuel efficient vehicle following." pp. 1350-1355.

[24] S. E. Li, H. Peng, K. Li, and J. Wang, "Minimum fuel control strategy in automated car-following scenarios," *IEEE Transactions on Vehicular Technology,* vol. 61, no. 3, pp. 998-1007, 2012.

[25] N. Mueller, S. Strauss, S. Tumback, G.-C. Goh, and A. Christ, "Next Generation Engine Start/Stop Systems:"Free-Wheeling"," *SAE International Journal of Engines,* vol. 4, no. 2011-01-0712, pp. 874-887, 2011.

[26] N. Müller, S. Strauss, S. Tumback, and A. Christ, "Coasting–Next Generation Start/Stop Systems," *MTZ worldwide eMagazine,* vol. 72, no. 9, pp. 14-19, 2011.

[27] S. Xu, S. E. Li, H. Peng, B. Cheng, X. Zhang, and Z. Pan, "Fuel-Saving Cruising Strategies for Parallel HEVs," *IEEE Transactions on Vehicular Technology*, vol. 65, no. 6, pp. 4676-4686, 2016.

[28] S. E. Li, K. Deng, Y. Zheng, and H. Peng, "Effect of Pulse‐and‐Glide Strategy on Traffic Flow for a Platoon of Mixed Automated and Manually Driven Vehicles," *Computer‐Aided Civil and Infrastructure Engineering,* vol. 30, no. 11, pp. 892-905, 2015.

[29] S. Xu, S. E. Li, X. Zhang, B. Cheng, and H. Peng, "Fuel-optimal cruising strategy for road vehicles with step-gear mechanical transmission," *IEEE Transactions on Intelligent Transportation Systems,* vol. 16, no. 6, pp. 3496-3507, 2015.

[30] H. Waschl, I. Kolmanovsky, M. Steinbuch, and L. D. Re, *Optimization and Optimal Control in Automotive Systems*: Springer, 2014.

[31] G. Rizzoni, L. Guzzella, and B. M. Baumann, "Unified modeling of hybrid electric vehicle drivetrains," *IEEE/ASME transactions on mechatronics*, vol. 4, no. 3, pp. 246-257, 1999.

[32] J. Liu, “Modeling, configuration and control optimization of power-split hybrid vehicles,” The University of Michigan, 2007.

[33] X. Zhang, “Design of Power Split Hybrid Powertrains with Multiple Planetary Gears and Clutches,” The University of Michigan, 2015.

[34] X. Zhang, C.-T. Li, D. Kum, and H. Peng, “Prius+ and volt-: Configuration analysis of power-split hybrid vehicles with a single planetary gear,” *IEEE Transactions on Vehicular Technology,* vol. 61, no. 8, pp. 3544-3552, 2012.

[35] X. Zhang, S. E. Li, H. Peng, and J. Sun, “Efficient Exhaustive Search of Power-Split Hybrid Powertrains With Multiple Planetary Gears and Clutches,” *Journal of Dynamic Systems, Measurement, and Control,* vol. 137, no. 12, pp. 121006, 2015.

[36] X. Zhang, H. Peng, J. Sun, and S. Li, “Automated modeling and mode screening for exhaustive search of double-planetary-gear power split hybrid powertrains,” in ASME 2014 Dynamic Systems and Control Conference, 2014.

[37] R. Bellman, R. Kalaba, and B. Kotkin, “Polynomial approximation - a new computational technique in dynamic programming: allocation processes,” *Mathematics of Computations,* vol. 17, no. 82, pp. 155-161, 1963.

[38] C.-T. Li, and H. Peng, “Optimal configuration design for hydraulic split hybrid vehicles,” in American Control Conference (ACC), 2010, pp. 5812-5817.

[39] J. Liu, and H. Peng, “A systematic design approach for two planetary gear split hybrid vehicles,” *Vehicle System Dynamics,* vol. 48, no. 11, pp. 1395-1412, 2010.

[40] E. Pistikopoulos, A. Galindo, V. Dua, E. S. Kikkinides, L. Papageorgiou, W. Jorisch, K.-W. Benz, W. Neumann, M. Köhler, and W. Fritzsche, *Multi-Parametric Programming: Theory, Algorithms and Applications, Volume*: Weinheim: WileyVCH, 2007.

[41] L. Serrao, S. Onori, and G. Rizzoni, "ECMS as a realization of Pontryagin's minimum principle for HEV control." pp. 3964-3969.

[42] C. Musardo, G. Rizzoni, Y. Guezennec, and B. Staccia, “A-ECMS: An adaptive algorithm for hybrid electric vehicle energy management,” *European Journal of Control,* vol. 11, no. 4-5, pp. 509-524, 2005.

[43] C.-C. Lin, S. Jeon, H. Peng, and J. M. Lee, “Driving pattern recognition for control of hybrid electric trucks,” *Vehicle System Dynamics,* vol. 42, no. 1-2, pp. 41-58 %@ 0042-3114, 2004.

[44] T. Yoshimura, *Vehicle power transmission,* US20110314960A1, 2008.

[45] M. Bian, L. Chen, Y. Luo, and K. Li, “A dynamic model for tire/road friction estimation under combined longitudinal/lateral slip situation,” 2014.

[46] S. Bai, J. Maguire, and H. Peng, *Dynamic analysis and control system design of automatic transmissions*: SAE International, 2013.

[47] SAE, "SAE Standard J2807: Performance requirements for determining tow-vehicle gross combination weight rating and trailer weight rating," Society of Automotive Engineers International, 2012.

[48] Z. Pan, H. Peng, and N. Ravi, *Hybrid all-wheel drive system having dynamic clutches*, 2018.

[49] R. Bellman, *Dynamic programming*: Courier Corporation, 2013.

[50] J. Liu, and H. Peng, “Modeling and control of a power-split hybrid vehicle,” *IEEE transactions on control systems technology,* vol. 16, no. 6, pp. 1242-1251, 2008.

[51] B. Sampathnarayanan, L. Serrao, S. Onori, G. Rizzoni, and S. Yurkovich, "Model predictive control as an energy management strategy for hybrid electric vehicles." pp. 249-256.

[52] S. Onori, and L. Serrao, "On Adaptive-ECMS strategies for hybrid electric vehicles."

[53] Z. Chen, C. C. Mi, J. Xu, X. Gong, and C. You, “Energy management for a power-split plug-in hybrid electric vehicle based on dynamic programming and neural networks,” *IEEE Transactions on Vehicular Technology,* vol. 63, no. 4, pp. 1567-1580, 2014.

[54] G.-E. Katsargyri, I. Kolmanovsky, J. Michelini, M. Kuang, A. Phillips, M. Rinehart, and M. Dahleh, “Path dependent receding horizon control policies for hybrid electric vehicles,” in 18th IEEE International Conference on Control Applications, (ISIC), Saint Petersburg, Russia, 2009, pp. 607-612.

[55] R. Prohaska, A. Duran, A. Ragatz, and K. Kelly, *Statistical characterization of medium-duty electric vehicle drive cycles*, National Renewable Energy Lab.(NREL), Golden, CO (United States), 2015.

[56] M. P. O'Keefe, A. Simpson, K. J. Kelly, and D. S. Pedersen, "Duty cycle characterization and evaluation towards heavy hybrid vehicle applications," in the 2007 SAE World Congress and Exhibition, 2007.